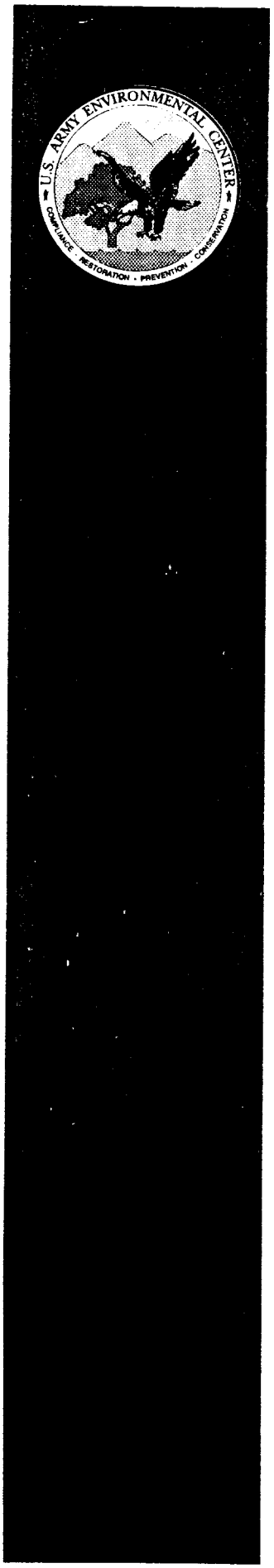

Report No. CETHA-TS-CR-92066

GEOPHYSICAL DIFFRACTION TOMOGRAPHY: THEORY, IMPLEMENTATION, AND RESULTS

November 1992

Alan Witten
Oak Ridge National Laboratory
Oak Ridge, Tennessee 37831

SECURITY CLASSIFICATION OF THIS PAGE

REPORT DOCUMENTATION PAGE

Form Approved
OMB No. 0704-0188

1a. REPORT SECURITY CLASSIFICATION	1b. RESTRICTIVE MARKINGS
2a. SECURITY CLASSIFICATION AUTHORITY	3. DISTRIBUTION/AVAILABILITY OF REPORT
2b. DECLASSIFICATION/DOWNGRADING SCHEDULE	unlimited
4. PERFORMING ORGANIZATION REPORT NUMBER(S)	5. MONITORING ORGANIZATION REPORT NUMBER(S)
	CETHA-TS-CR-92066
6a. NAME OF PERFORMING ORGANIZATION: Oak Ridge National Laboratory; 6b. OFFICE SYMBOL (If applicable)	7a. NAME OF MONITORING ORGANIZATION: USATHMA
6c. ADDRESS (City, State, and ZIP Code): P.O. Box 2008, Oak Ridge, TN 37831-6200	7b. ADDRESS (City, State, and ZIP Code): Aberdeen Proving Ground, MD 21010-5401
8a. NAME OF FUNDING/SPONSORING ORGANIZATION: USATHMA; 8b. OFFICE SYMBOL (If applicable): CETHA-TS-D	9. PROCUREMENT INSTRUMENT IDENTIFICATION NUMBER: MIPR 2199
8c. ADDRESS (City, State, and ZIP Code): Aberdeen Proving Ground, MD 21010-5401	10. SOURCE OF FUNDING NUMBERS

PROGRAM ELEMENT NO.	PROJECT NO.	TASK NO.	WORK UNIT ACCESSION NO.

11. TITLE (Include Security Classification)
Geophysical Diffraction Tomography: Theory, Implementation, and Results

12. PERSONAL AUTHOR(S)
Witten, Alan J.

13a. TYPE OF REPORT	13b. TIME COVERED	14. DATE OF REPORT (Year, Month, Day)	15. PAGE COUNT
Final	FROM 88,8,18 TO 91,10,1	92, 11, 2	91

16. SUPPLEMENTARY NOTATION

17. COSATI CODES			18. SUBJECT TERMS (Continue on reverse if necessary and identify by block number)
FIELD	GROUP	SUB-GROUP	geophysical imaging, tomography, acoustic data acquisition

19. ABSTRACT (Continue on reverse if necessary and identify by block number)

Geophysical diffraction tomography (GDT) is a high resolution technique for quantitative subsurface imaging. The method is based on the analysis of data acquired from the propagation of scalar waves from an array of source positions to an array of receiver positions. Images of spatial variations in refractive index are produced by a procedure which propagates the received signal backwards through a subsurface cross-section. This is conceptually similar to the elements of optical holography.

An acoustic-based GDT imaging procedure has been implemented using a specially developed data acquisition system employing a source deployed on the ground surface and an array of 29 hydrophones that are emplaced in a borehole. Confirmatory field studies have demonstrated that GDT can successfully image naturally-occurring and man-made buried features.

20. DISTRIBUTION/AVAILABILITY OF ABSTRACT	21. ABSTRACT SECURITY CLASSIFICATION
☒ UNCLASSIFIED/UNLIMITED ☐ SAME AS RPT. ☐ DTIC USERS	

22a. NAME OF RESPONSIBLE INDIVIDUAL	22b. TELEPHONE (Include Area Code)	22c. OFFICE SYMBOL
Wayne Sisk	(410) 671-2054	CETHA-TS-D

DD Form 1473, JUN 86 *Previous editions are obsolete.* SECURITY CLASSIFICATION OF THIS PAGE

GEOPHYSICAL DIFFRACTION TOMOGRAPHY: THEORY, IMPLEMENTATION, AND RESULTS

Alan Witten
Energy Division
Oak Ridge National Laboratory
Oak Ridge, Tennessee 37831–6200

November 2, 1992

SUMMARY

Geophysical diffraction tomography (GDT) is a high resolution technique for quantitative subsurface imaging. The method is based on data derived from the propagation of scalar waves from an array of source positions to an array of receivers. Images of spatial variations in refractive index are produced by a procedure which propagates the received signal backwards through a subsurface cross-section. This is conceptually similar to the elements of optical holography.

An acoustic-based GDT imaging procedure has been implemented for acoustic waves. The field instrumentation consists of a commercially-available, impulsive acoustic source, an array of 29 hydrophone/preamp pairs, a custom-made data acquisition system, and portable personal computer. Data is acquired in an offset vertical seismic profiling configuration with the receiver array positioned in a borehole and the source successively fired at fixed intervals along a line on the ground surface radially outward from the borehole. The resulting image is of a two-dimensional vertical cross-section spanning the depth interval of the receiver array and horizontal extent which corresponds to the length of the source line. The personal computer is used to control the data acquisition system, execute all the required signal processing steps, and display the final image. The entire procedure can be implemented in near real-time in the field.

To date, five field studies have performed as part of the development and demonstration of GDT. These studies have taken place in a variety of geologic settings and have successfully imaged naturally-occurring and man-made buried features.

Contents

List of Figures

List of Tables

1 INTRODUCTION

It is not necessary to delve deeply into the scientific literature to understand that disposal of hazardous waste is a national problem. Public health and environmental damages from hazardous materials being dumped or improperly disposed of are reported daily in the news. Cleanup of these dumps or burial sites is a high national priority and will remain such for decades based on the magnitude of the problem. For a large number of these sites, discovering what is buried where poses an extremely difficult technical challenge (Benson et al. 1982). Remote sensing has become a primary means of investigating the subsurface features at such sites. Nonintrusive detection methods offer numerous benefits over the more conventional drilling methods. They are safer for the workers, do not present the risk of puncturing waste containers or liners allowing for further contamination, and in many cases are faster, cheaper, and more accurate.

Techniques such as ground penetrating radar, seismic refraction, electrical conductivity, and magnetics have all been employed for remote sensing of buried wastes. The feature common to these and, in fact, all remote sensing techniques is that they employ seismic or electromagnetic wave energy to deduce perturbations in subsurface wave propagation properties which infer the existence and/or location of the features of interest. Most remote sensing techniques currently used at hazardous waste sites have been in existence many years and were originally developed for resource exploration. These methods generally offer low spatial resolution as well as requiring considerable interpretive insight. While research continues, the traditional remote sensing techniques appear to be almost fully exploited. Ground penetrating radar is a relatively new geophysical method which has achieved considerable success. This method offers greater resolution than most others; however, it requires interpretive insight and its value is limited in certain soil types.

The technique presented in this report, geophysical diffraction tomography (GDT) (Devaney 1984; Witten and Long 1986; Witten and Molyneux 1988; Witten and King 1988; Witten and King 1989; King et al. 1989; King and Witten 1989) is the next generation of remote sensing technology. It begins with the basic concept of all remote sensing in the use of energy waves to probe the subsurface environment; however, it progresses beyond existing methods by making a coherent analyses of the collected signal.

This report presents an overview of geophysical tomography, in general, and a complete description of the physical and mathematical principles of geophysical diffraction tomography. A complete description of the instrumentation and field implementation of geophysical tomography, along with a presentation of field results to date, is also included. The report concludes with discussion of potential applications of this technique as well as directions for future development efforts.

2 BACKGROUND

The technique applied here to shallow, subsurface imaging is known as geophysical diffraction tomography which is a generalization of the reconstruction algorithms of straight-ray tomography (Kak 1979) as used in x-ray CT scanners for diagnostic medicine. Earlier methods used in geophysical tomography were based on such straight-ray methods (Anderson and Dziewonski 1984; Dines and Lytle 1979; Fisk et al. 1987). In order to better understand diffraction tomography and to establish the motivation for pursuing the more complex signal processing requirements of this method, it is enlightening to review the basis and limitations of the straight ray methods.

The steps associated with straight-ray image formation are illustrated in Fig. 1. Reconstructions are developed from a system of experiments, each forming a partial image. In the simple example presented here, we will consider a light as our energy source and a white wall as a detector plane. The source and detector maintain a fixed orientation relative to each other but free to rotate about the target which is taken to be an opaque disk. Each experiment is performed at a different instrument orientation relative to the target. In the first experiment, the upper left portion of Fig. 1, the detector line is vertical. The presence of the target blocks the light causing a shadow to be cast on the wall. The first partial image is formed by tracing a line from each edge of the shadow back to the source defining a triangle as shown in the upper right portion of Fig. 1. It is clear that, on the basis of a single experiment, the image is quite poor. The image quality can be significantly improved by incorporating information derived from additional experiments. The lower left portion of Fig. 1 illustrates the measurement configuration for a second experiment in which the instrumentation has been rotated 90^0 relative to the first experiment. The procedure follows that of the first experiment with the formation of a second partial image; also a triangle. A full reconstruction based on these two experiments is formed by taking the intersection of the two partial images as shown in Fig. 1. Notice that the image has improved significantly over that from a single experiment and it is easy to imagine the increased image quality that can be obtained from many experiments.

Before considering the problem of geophysical tomography, it is worthwhile to point out that this technique is frequently referred to as "backprojection" since it projects information from the detector plane back, along straight lines, to the source. As will become evident later, this is different from diffraction tomography which is a "backpropagation" method. In general, backprojection considers semitransparent targets as well as opaque ones. Rather than tracing rays only at the edges of the shadow, a continuum of rays are traced from the entire detector length back to the source. Each ray is assigned a fixed value of gray level equal to that measured at a fixed position on the detector plane. For example, every ray not passing through the target is assigned a level of white, while rays passing through the target each have an appropriate gray level which would only be black if the target is perfectly opaque. In this manner CT scanners provide quantitative images of local attenuation.

In medical CT scanners, images are formed based on measurements of x-ray intensity. For geophysical measurements, images can be derived from straight-ray-path algorithms based

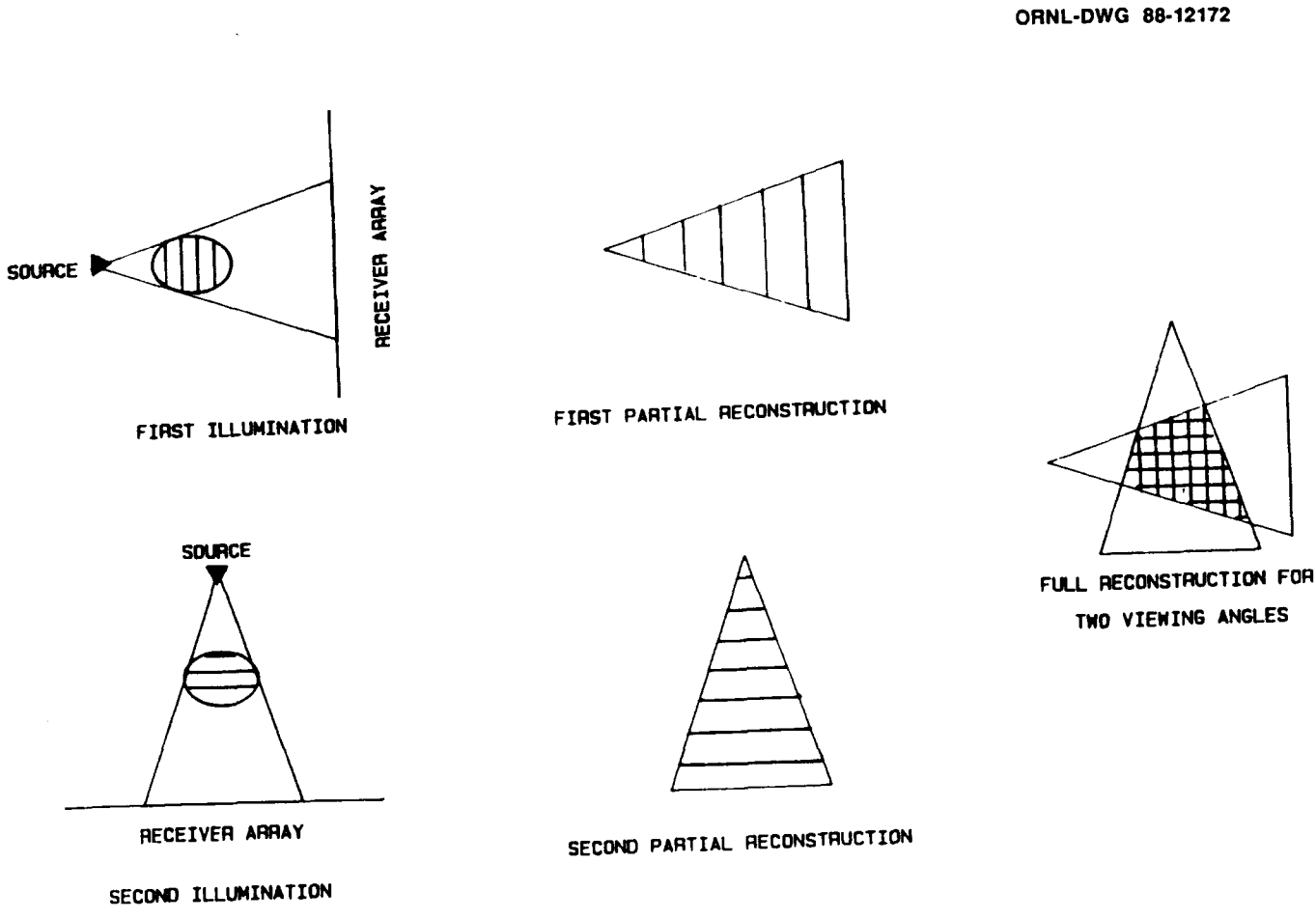

Figure 1: Simplified illustration of the straight-ray imaging procedure as used in CT Scanners.

on either the time of first signal arrival or the amplitude of this arriving signal. Figure 2 is an example of a typical recorded signal as a function of time from a geophysical experiment with the time and amplitude of the first arrival denoted by τ and A, respectively. For an assumed straight ray path of length L as shown in Fig. 3, the measured amplitude of the first arrival A is related to the local, spatially-varying attenuation per unit length $a(\underline{x})$ by

$$A = \int_0^L a(\ell) d\ell \tag{1}$$

where ℓ is the position along the ray. Similarly, the time of first arrival τ is related to local variations in wave speed $c(\underline{x})$ by

$$\tau = \int_0^L \frac{1}{c(\ell)} \, d\ell \, . \tag{2}$$

Local values of a and c can be reconstructed by an inversion of eqs. (1) and (2), respectively. This can be accomplished by approximating the continuum of values of a and c by discrete values a_{ij} or c_{ij} averaged over cells defined by superimposing a grid onto the study region. Then by considering many ray paths resulting from a multiplicity of sources and receivers and by approximating the integrals in eqs. (1) and (2) as finite sums, a system of algebraic equations is formed which can be inverted for each value of a_{ij} or c_{ij} by standard numerical methods. An alternative inversion scheme can be applied by expressing the integrals in eqs. (1) and (2) in a modified form and then utilizing methods of Fourier deconvolution.

Straight ray geophysical tomography has successfully been employed for a number of problems associated with shallow and deep subsurface investigations. These include the mapping of karst features (Fisk et al. 1987), steam flood zones associated with oil recovery (Witterholt et al. 1981) and inhomogeneities in the earth's mantle (Anderson and Dziewonski 1984), as well as the location of tunnels and voids (Olehoeft 1989). These studies have been performed in an offset vertical seismic profiling configuration (sources on the ground surface and receivers in a borehole or vice versa) such that shown in Fig. 3 using seismic (acoustic) energy sources; and in a cross-borehole configuration (sources and receivers in parallel boreholes) as shown in Fig. 4 for both seismic and radar frequencies electromagnetic sources. Figure 5 is an image of a tunnel cross-section located in rock obtained from cross-borehole seismic data and a backprojection tomography algorithm.

While backprojection (straight-ray) algorithms of geophysical tomography have, in some cases, provided excellent results, they have failed in others due to limitations in the method which are well understood. The first difficulty is that, unlike medical CT scanners which are free to rotate 360^0 about the target, geophysical measurements are necessarily constrained to certain fixed measurement geometries (Figs. 3 and 4). This is illustrated in Fig. 6 for an offset VSP geometry. Shown here is the approximate image (cross-hatched area) of a target (black) obtained from two experiments (source positions). Note that the image here is quite poor and considerably elongated on a diagonal. Also note that no substantial improvement in image quality could be obtained by considering additional source positions and that the

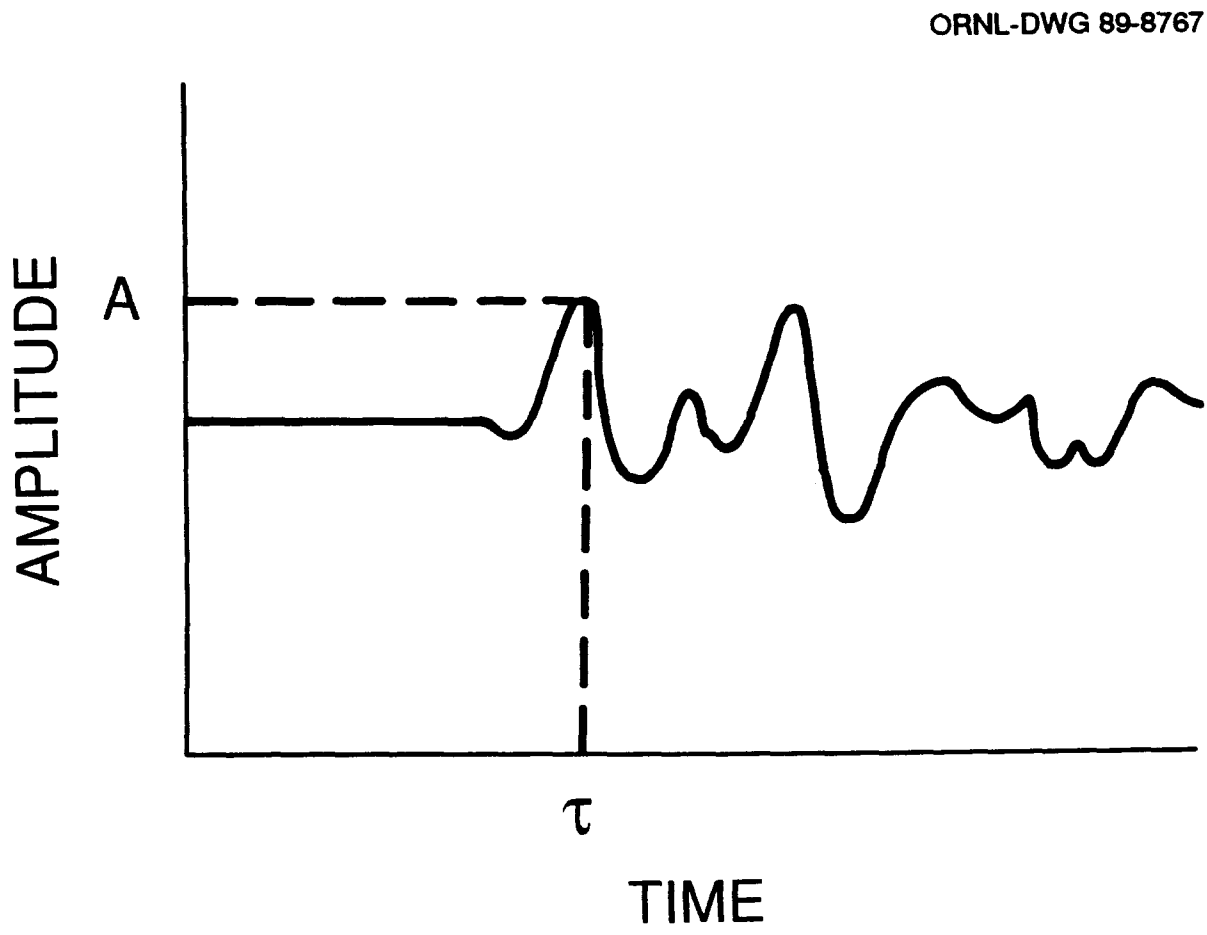

Figure 2: Plot of amplitude vs. time showing amplitude A of first arriving signal τ.

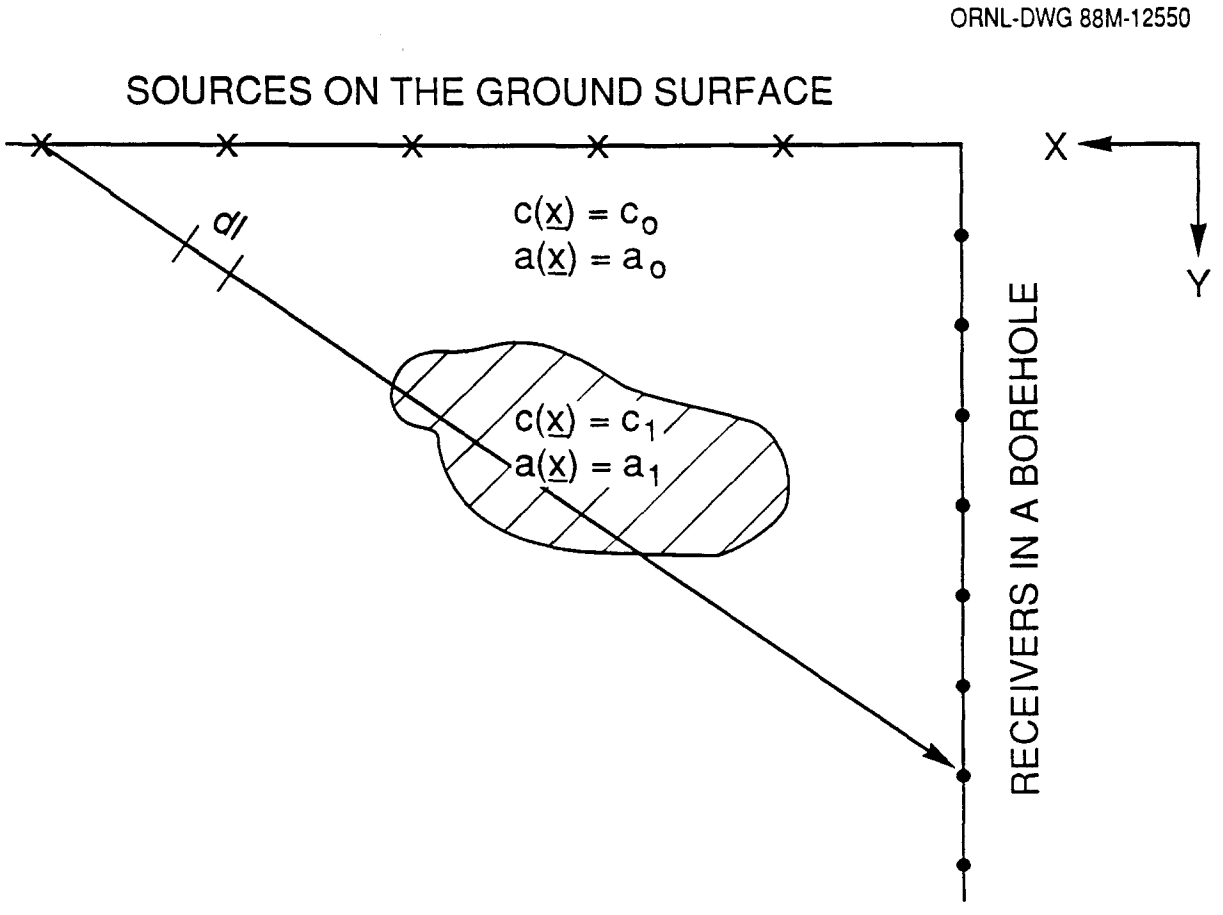

Figure 3: Illustration of straight-ray geophysical tomography concept in an offset VSP configuration.

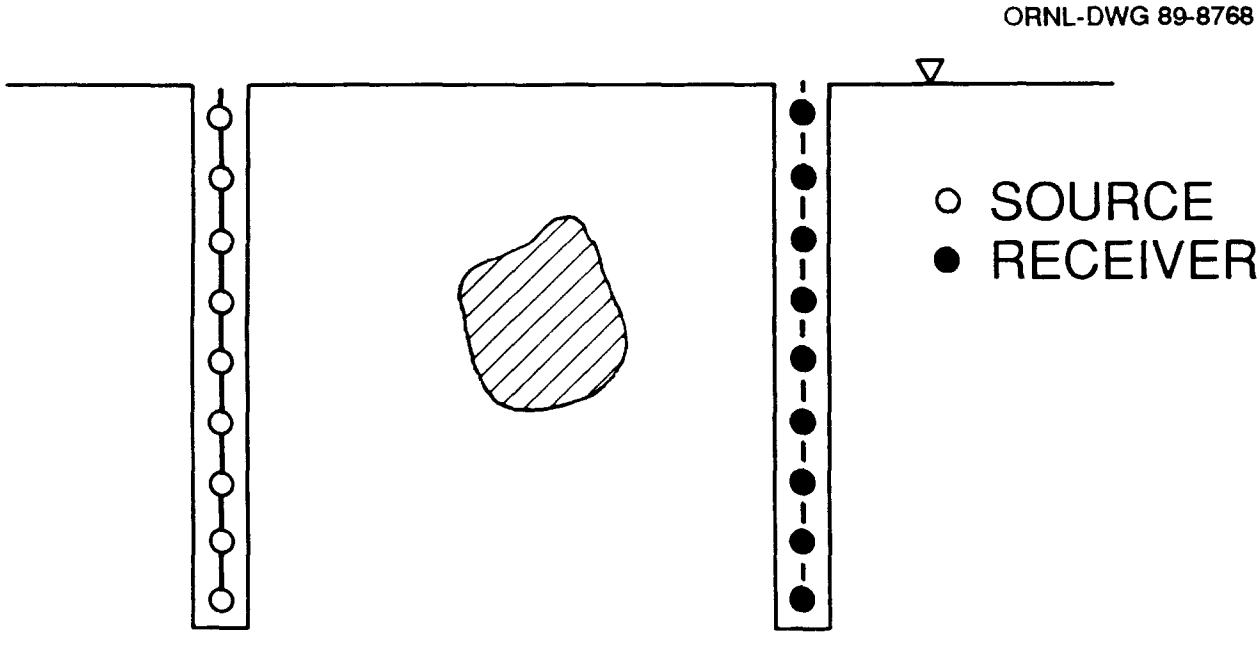

Figure 4: Cross-borehole data acquisition geometry.

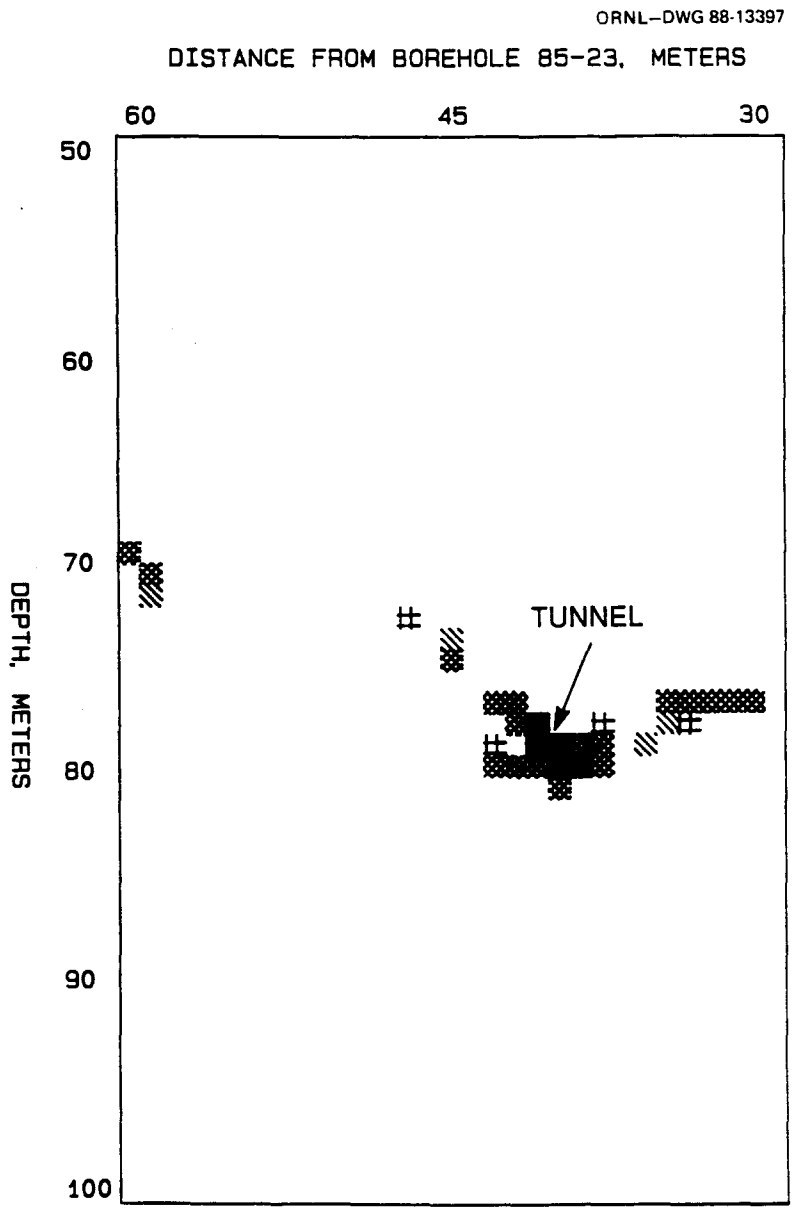

Figure 5: Image of tunnel in rock obtained from the application of a straight-ray tomography algorithm in a cross-borehole configuration.

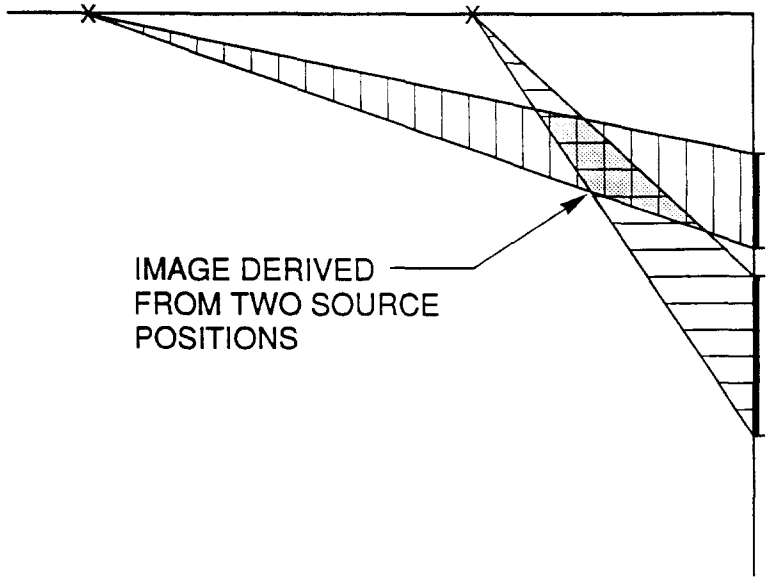

Figure 6: Illustration of the loss of image resolution associated with a fixed measurement configuration.

image would be worse if the target were deeper and/or further from the receiver array. This difficiency is associated with the limited range of view angles (perspectives) which result from a fixed measurement geometry.

A second and more fundamental problem associated with backprojection is that rays do not travel in straight lines in all but the most homogeneous settings. When a ray encounters a region of different mechanical or electromagnetic properties it will both bend (refract) on transmission and reflect from the boundary of the inhomogeneity. The degree of refraction and the proportion of incident energy transmitted and reflected will depend on the local refractive index of the inhomogeneity. The amplitude of the received signal will be reduced due to the portion of the incident energy which is reflected and this will produce an artificially high value of imaged local attenuation. Furthermore, the ray bending which occurs during transmission will alias the "shadow" cast by the target and, as a result, it will be backprojected along erroneous straight-ray paths. This is illustrated in Fig. 7. Because of these limitations of straight ray algorithms, they are best suited for applications in relatively simple settings containing relatively large targets where high spatial resolution is not required (Dines and Lytle 1979). In more complex settings, some features of interest may be unresolved.

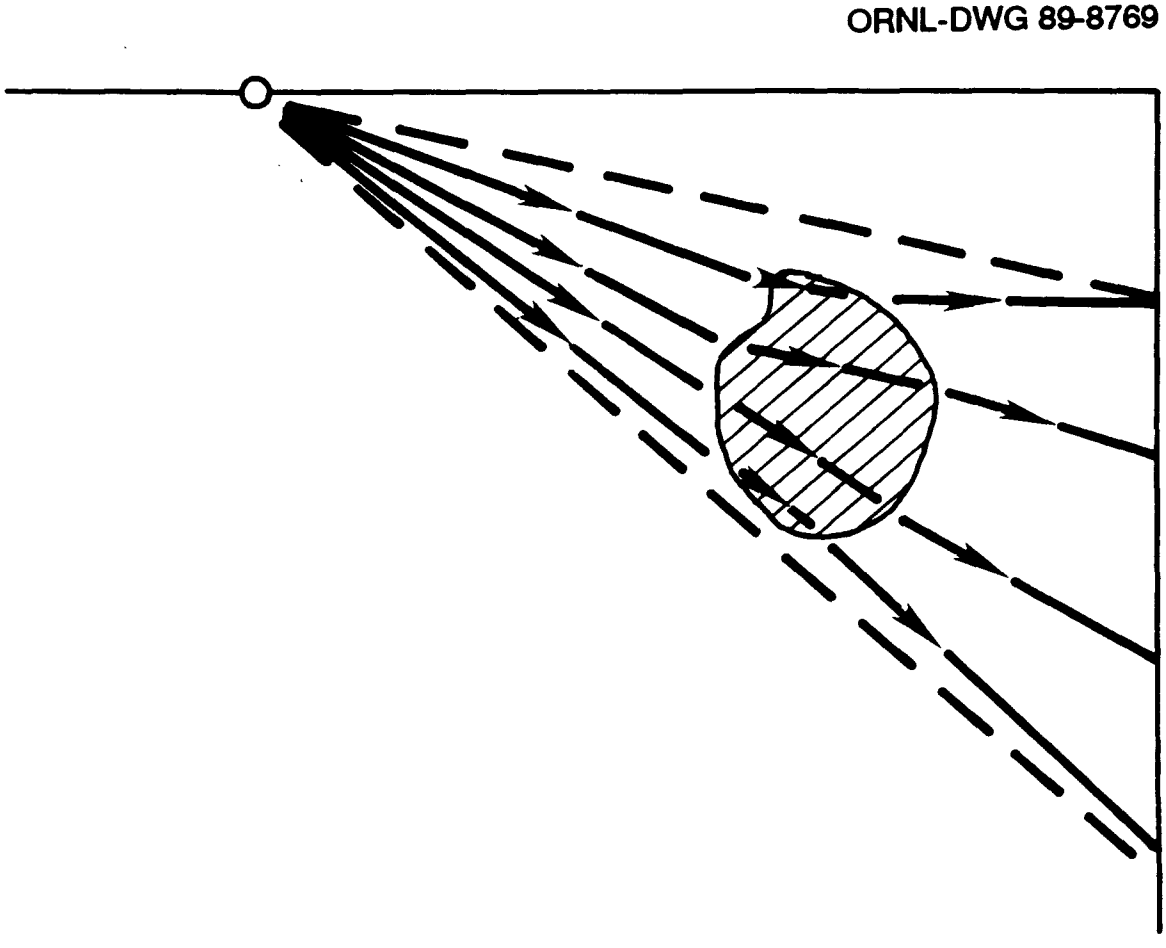

Figure 7: Illustration of ray bending (solid lines) which occurs as a result of changes in wave-speed and the resulting erroneous backprojection (dashed lines).

3 GEOPHYSICAL DIFFRACTION TOMOGRAPHY

As noted earlier, geophysical diffraction tomography (GDT) is considered a backpropagation technique since it propagates waves back from the receivers to the source rather than using straight-ray path backprojection. This approach is based on the scalar wave equation

$$\nabla^2 p + k_0^2 n^2(\underline{x}) p = f(\underline{x}, \omega) \tag{3}$$

where p is the pressure (assuming a seismic source) which has been Fourier transformed in time

$$p(\underline{x}, \omega) = \int \bar{p}\ (\underline{x}, t) e^{i\omega t} dt\ , \tag{4}$$

ω is the angular frequency, k_o is the wavenumber at frequency ω and reference wave speed c_o, $k_o = \omega / c_o$, $n(\underline{x})$ is the local value of refractive index $n = c_o / c(\underline{x})$, and f characterizes the spatial and frequency distribution of the wave source. The objective of GDT is to invert eq. (3) in order to reconstruct $n(\underline{x})$ from values of the pressure p measured over some receiver contour. This is accomplished by writing the formal solution to eq. (3) (Morse and Feshbach 1953) as

$$p(\underline{x}, \omega) = \int G(\underline{x} - \underline{\xi})\ f(\underline{x}, \omega)\ d\underline{\xi} - k_0^2 \int G(\underline{x} - \underline{\xi})\ O(\underline{\xi})\ p(\underline{\xi}, \omega)\ d\underline{\xi}\ , \tag{5}$$

where $O(\underline{x}) = 1 - n^2(\underline{x})$ is referred to as the "object profile" and $G(\underline{x})$ is the Green's function for propagation.

Before continuing the discussion of GDT it is worthwhile to examine eq. (5) and compare it to the backprojection formulation of eqs. (1) and (2). First consider the left side of eq. (5) which is composed of two terms. The first is the measured pressure p and the second is a quantity known from f and G. These terms can be collectively called $D(\underline{x}, \omega)$, the reduced data, and eq. (5) can be written as

$$D(\underline{x}, \omega) \ = \ - k_0^2 \int G(\underline{x} - \underline{\xi})\ O(\underline{\xi})\ p(\underline{\xi},\ \omega)\ d\underline{\xi}\ . \tag{6}$$

We immediately can see that this equation is quite similar to those of backprojection, eqs. (1) and (2), in that both formulations have a known quantity derived from measurements on the left sides of the equations, while the functions of interest ($O(\underline{x})$ for backpropagation; $a(\underline{x})$ and $c(\underline{x})$ for backprojection) are under the integral on the right side. Equation (6) is, in fact, a generalization of backprojection and eqs. (1) and (2) can be derived from eq. (6) by invoking the appropriate simplifying assumption. Furthermore, for nonattenuating media $O(\underline{x})$ is real; however, for attenuating media $O(\underline{x})$ is complex with the real part related to speed variations and the imaginary part related to local variations in attenuation.

One complicating aspect of backpropagation is that the pressure appears under the integral of eq. (6) along with the object profile. This means that the pressure must be known everywhere that values of $O(\underline{x})$ are desired, not just along some measurement contour.

While it is possible to invert this nonlinear formulation, it is quite difficult as well as computationally intensive. For this reason, one simplifying assumption is made in the development of GDT, the weak scatter approximation. It is assumed that the total pressure p is composed of an incident pressure, p_i, that satisfies eq. (3) with $n(\underline{x}) = 1$ ($O(\underline{x}) = 0$) along with a perturbed field associated with inhomogeneities (nonzero values of $O(\underline{x})$). It is further assumed that inhomogeneities produce a scattered field which is small compared to p_i. With this, the linearized formulation is

$$D(\underline{x},\omega) \;=\; -\,k_0^2 \int G(\underline{x} \,-\, \underline{\xi})\; O(\underline{\xi})\; p_i(\underline{\xi})\; d\underline{\xi}\;, \tag{7}$$

where p_i satisfies

$$\nabla^2 p_i \;+\; k_0^2 p_i = f(\underline{x},\omega)\;. \tag{8}$$

In this form, the only unknown on the right side of eq. (7) is the quantity to be imaged, $O(\underline{x})$.

There are two forms of weak scatter approximations that can be invoked, the Born (Wolf 1969) and the Rytov (Devaney 1981). The Born approximation assumes that the total pressure is the sum of the incident field, p_i, and a scattered field, p_s, so that

$$p \;=\; p_i \;+\; p_s\;. \tag{9}$$

The Rytov approximation takes the perturbations in pressure associated with inhomogeneities to be a multiplicative correction to the incident field as

$$p \;=\; p_i e^{\psi}\;, \tag{10}$$

where ψ is referred to as the complex phase. The imaginary part of ψ represents perturbations in the phase of the received signal associated with the presence of inhomogeneities. While the real part of ψ contains similar information associated with perturbations in signal amplitude, results will differ according to which weak scatter approximation is used. The relative merits of each and the motivation for selecting one over the other is addressed in the next chapter. The remainder of the derivation considered here can be cast in a unified form by the definition of the reduced data, D, given by

$$D(\underline{x},\omega) \;=\; \left\{ \begin{array}{l} p_s\;, \textit{Born approximation;} \\ p_i\psi\;, \textit{Rytov approximation.} \end{array} \right\} \tag{11}$$

The inversion of eq. (7) is straight forward but tedious. Therefore, the detailed mathematics for relatively general measurement geometries is provided in Appendix A. Here we highlight the inversion procedure for an offset VSP configuration focusing on the physical interpretation of the various steps in the procedure.

Conceptually, geophysical diffraction tomography is best described as an analog to optical holography as depicted in Fig. 8 (King et al. 1989). The first step in the imaging procedure is to construct the reduced data D [eq. (11)]. This is analogous to the interference pattern

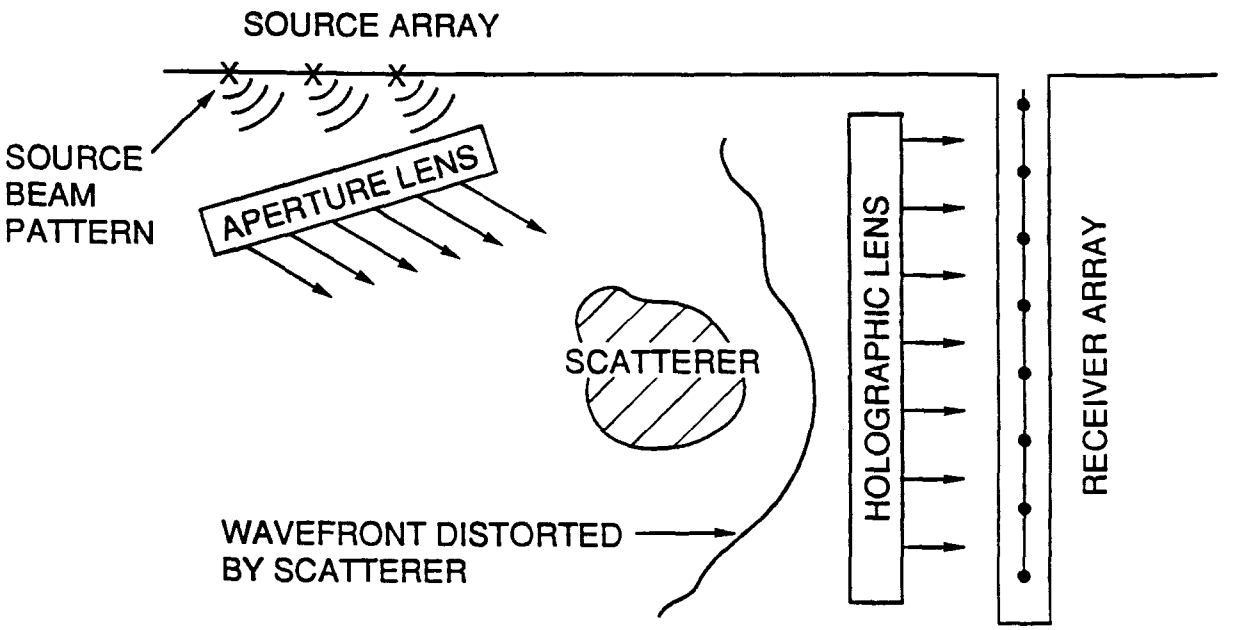

Figure 8: Illustration of the physical concept of geophysical diffraction tomography.

created in optical holography by the interaction between the laser illuminating the target and a reference beam. The next two mathematical steps associated with the inversion of eq. (7) are

$$\gamma\,(\ell'\,,\,\underline{s}_0)\;=\;\frac{k_0}{2}\,\underline{s}_0\,\cdot\,\underline{n}\int D(\ell'\,,\,\ell_o)e^{ik_0\underline{s}_0\,\cdot\,\underline{r}_o}\,, \tag{12}$$

the synthetic aperture step (Schultz and Clarebout 1978); and

$$\hat{O}\,[k_o(\underline{s}\;-\;\underline{s}_0)]\;=\;\frac{2i}{k_0}\,\underline{m}\;\cdot\;\underline{s}\int\gamma(\ell'\,,\underline{s}_0)e^{-ik_0\underline{s}\,\cdot\,\underline{r}'}\,d\ell'\,, \tag{13}$$

the holographic lens step. In eq. (12) and (13), ℓ_o and ℓ' are the positions of sources and receivers, respectively; and other parameters are defined in Fig. 9. The step corresponding to eq. (12) is a coherent sum or synthetic aperture step synthesizing a coherent wave from a superposition of all sources. Thus, this step produces an incident wave form similar to the coherent light produced by laser illumination. Different viewing perspectives are obtained by varying the direction of propagation $\underline{s}_0$ of this synthetic, illuminating incident wave field. Equation (13) is the mathematical analog of a holographic lens, refocusing the wavefield distorted by inhomogeneities. The result of the application of eq. (13) is the spatial Fourier transform $\hat{O}(\underline{K})$ of the object profile $O(\underline{x})$. This is similar to the image contained in the optical plate of holography. Finally, the image can be recovered by numerical inversion.

$$O(\underline{x})=\int\hat{O}(\underline{K})\;e^{i\underline{K}\,\cdot\,\underline{x}}d\underline{K}\,, \tag{14}$$

which is the mathematical analog to the presentation of the hologram by reillumination of the optical plate.

At this point it is appropriate to evaluate GDT in light of the problems and limitations associated with straight-ray backprojection described in the previous chapter. First and foremost are the complications arising from ray bending. Since GDT is a backpropagation method, in contrast to backprojection, it rigorously accounts for ray bending within the context of the invoked weak scatter approximation. Thus, no image artifacts occur provided that, in principle, the conditions of the weak scatter approximation are satisfied. In practice, this means that ray bending phenomenon are properly treated provided that strong scatters do not occur in close proximity to one another. In situations where this is not the case, proximate strong scatterers (inhomogenities) can be expected to blur together and a weak scatterer may not properly be resolved if it is proximate to a strong scatterer. While the limited view angles still occur in backpropagation, the inherent focus step, eq. (13), provides better resolution per experiment than does backprojection (Devaney 1983). Rather than a triangular partial reconstruction as depicted in Figs. 1 and 6, a single partial image of a circular disk derived from GDT will be eliptic.

One final and important point must be mentioned when comparing GDT with straight-ray tomography. Unlike the straight-ray approach which is based on the first arriving signal, GDT is a full waveform technique extracting information from the entire time series (Fig. 2). It is clear from eq. (4) that all features in the time series which influence the pressure at

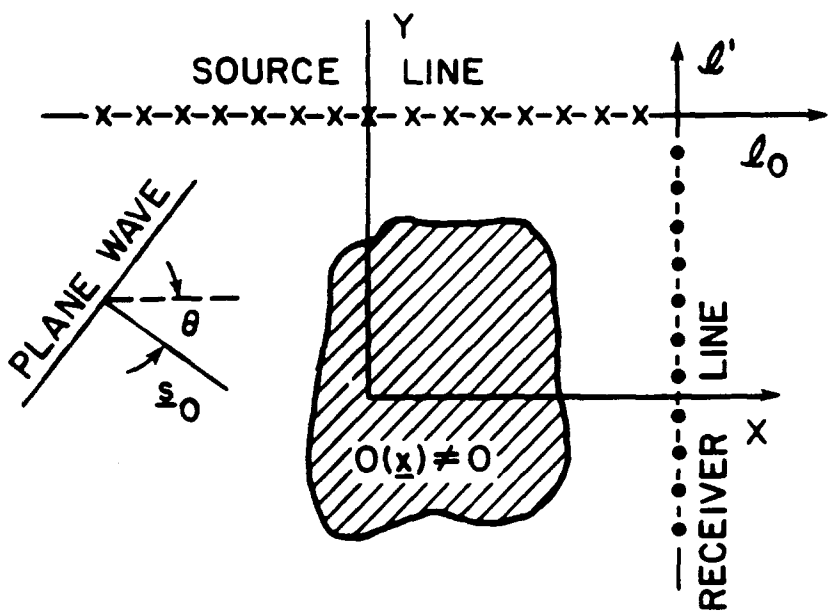

Figure 9: Notation used in the formulation of geophysical diffraction tomography in an offset VSP configuration.

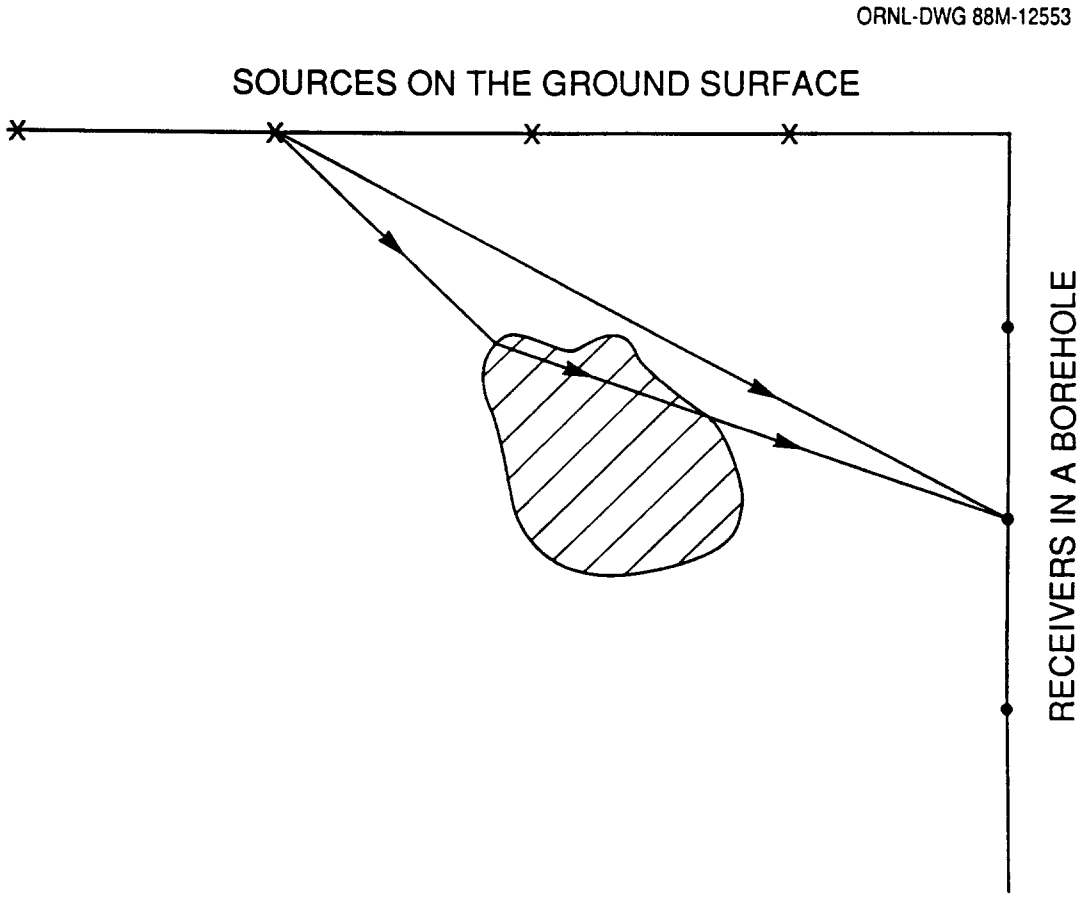

Figure 10: Illustration of possible multiple ray paths which produce constructive and/or destructive interference in the recorded time series.

a fixed frequency ω are considered in the GDT algorithm. This is illustrated in Fig. 10. Shown here are two realizable ray paths; one a direct path and the other refracted through the inhomogeneity. Under most conditions, the direct ray will be that which produces the first arriving signal. Consequently, this path provides little information about the inhomogeneity (except where it isn't) when considering first arrival information. In contrast, GDT extracts information for both ray paths as well as many others. Furthermore, unlike straight-ray tomography, GDT is not strictly a transmission technique. Therefore supplemental view angles can be considered by inclusion of slant-stack or synthetic aperture directions which are away from the receiver array. As illustrated in Fig. 11, this allows the incorporation of other late arriving signals associated with reflections or back scatter.

The signal processing steps associated with the implementation of the GDT algorithm described above are summarized in Fig. 12.

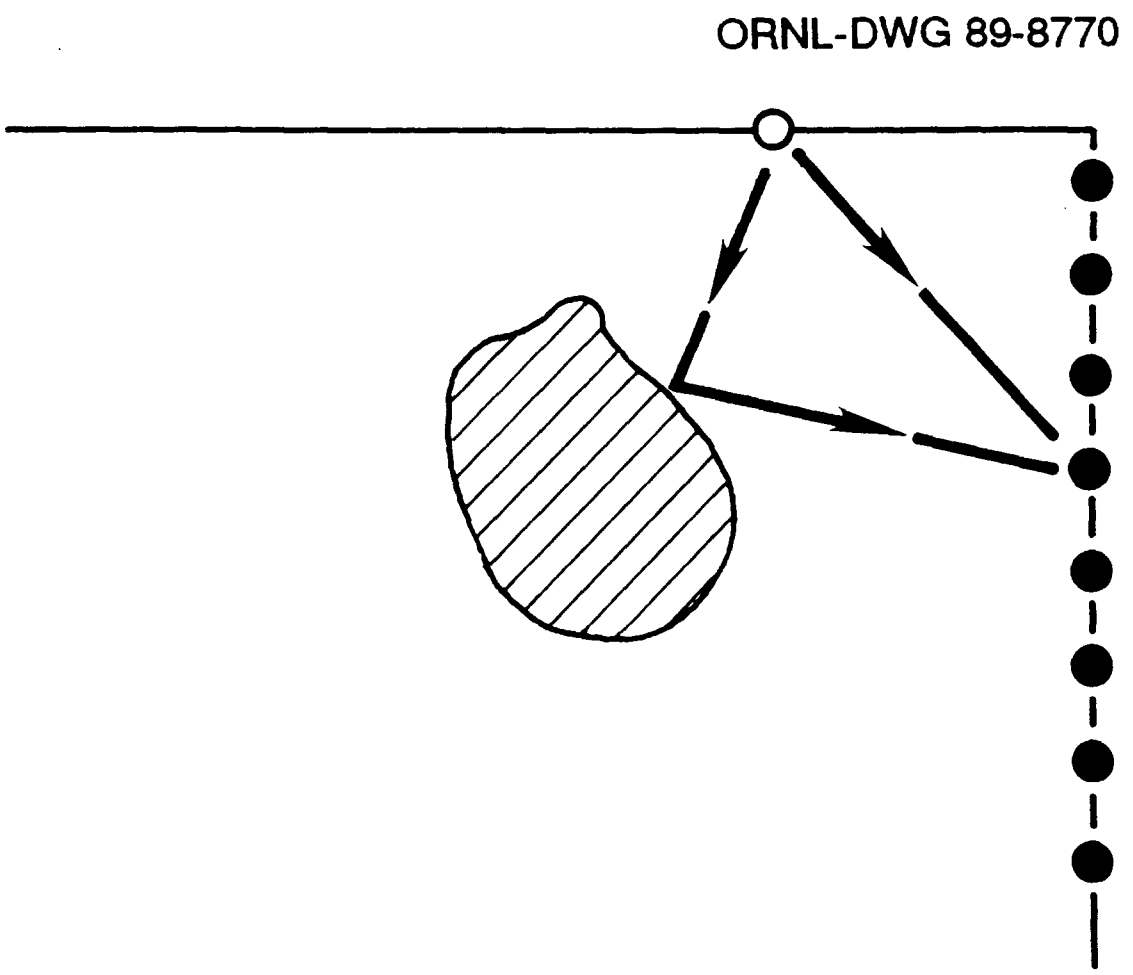

Figure 11: Illustration of the direct and backscattered ray paths.

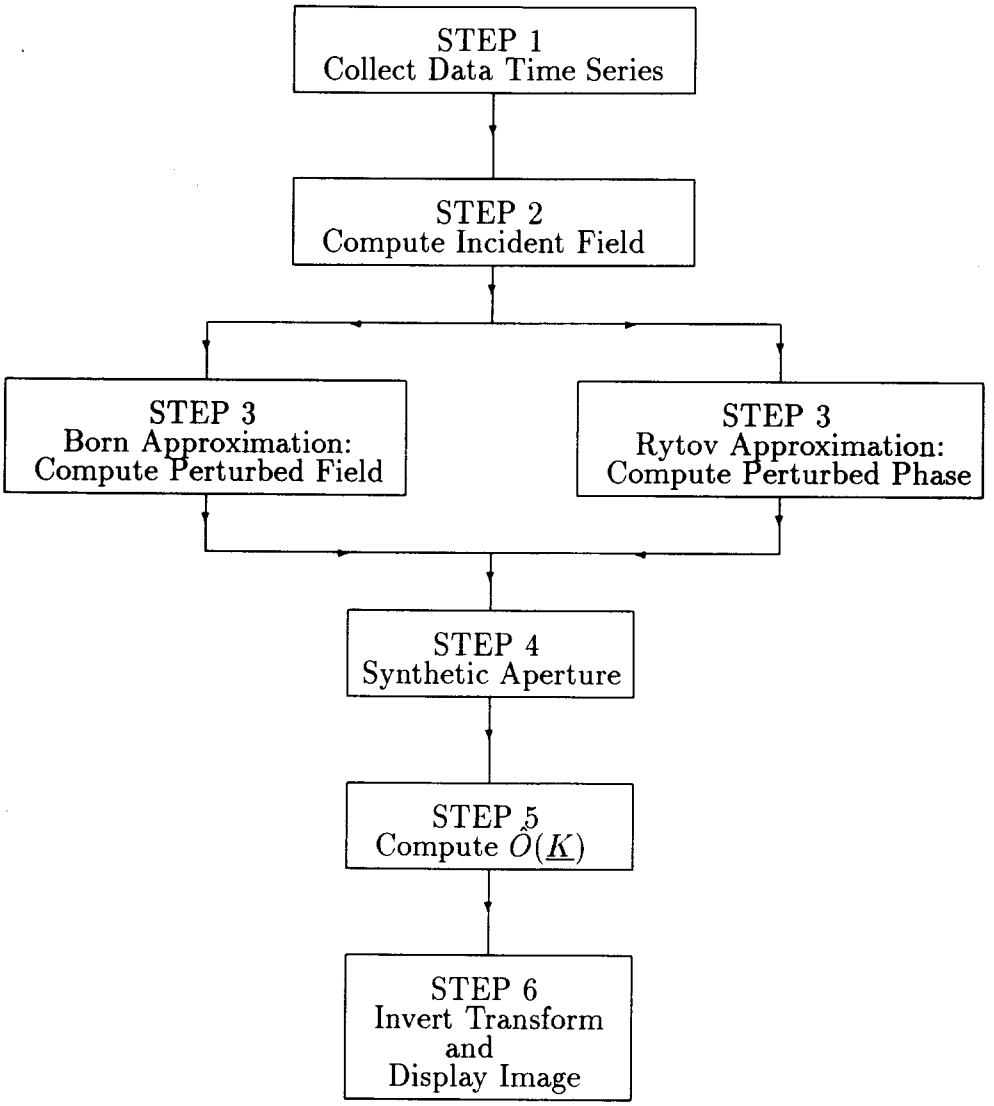

Figure 12: Sequence of steps employed in the implementation of geophysical diffraction tomography.

4 IMPLEMENTATION SCHEMES, INSTRUMENTATION, AND FIELD OPERATIONS

4.1 Measurement Geometries

There are three basic practical instrument configuration for field implementation of geophysical diffraction tomography. These are cross-borehole, offset VSP, and surface-to-surface geometries. The surface-to-surface configuration employs source and receiver arrays which are both located on the ground surface [Fig. 13(a)]. In the cross-borehole configuration, an array of acoustic sources is located in one borehole and an array of acoustic receivers is placed in a parallel borehole [Fig. 13(b)]. For offset VSP [Fig. 13(c)], receivers are again located in a borehole but sources are deployed on a line on the ground surface extending outward from the borehole.

The ultimate regions which can be imaged are defined by the particular geometry and the lengths of both the source and receiver arrays. For the cross-borehole geometry this two-dimensional vertical cross-section is a rectangular region with a vertical extent corresponding to the depth interval spanned by the receiver array and a horizontal extent defined by the distance between boreholes. For the offset VSP configuration, the vertical extent of the image is the depth interval spanned by the receivers while the horizontal boundaries of the imaged region are defined by the length of the source array on the ground surface. The vertical extent of the region which can be imaged in the surface-to-surface geometry is arbitrary and the horizontal extent of this region corresponds to the interval spanned by the surface-located receivers. In practice, however, these regions could be somewhat smaller due to the finite length of the source array. This is because it is necessary to simulate plane wave illumination by means of a slant stack or synthetic aperture procedure. As illustrated in Fig. 14, this synthetic wave is only near-planar over a certain portion of the illuminated region. It is therefore necessary to either reduce the imaged region or restrict the range of viewing angles in order to minimize image artifacts.

While each configuration described above can ideally achieve a range of viewing angles approaching 180^0, there exists significant differences in image quality among these measurement geometry. This is illustrated in Fig. 15 which shows images of a single circular disk for a number of geometries. The reason for these evident differences is that, while each configuration can utilize a comparable range of view angles, the specific view angles vary among configurations. It is clear that the best image is obtained from a cross-borehole configuration [Fig. 15(a)] while the worst is offered by the surface-to-surface method [Fig. 15(c)]. This difference is because the quality of information contained in a single view angle is a function of the particular angle. The most useful information is contained in transmission angles while the value of reflection or backscatter angles is minimal. For cross-hole geometries all available view angles are associated with transmission and, for offset VSP, 50% of available views are transmission angles. The surface-to-surface configuration offers no transmission

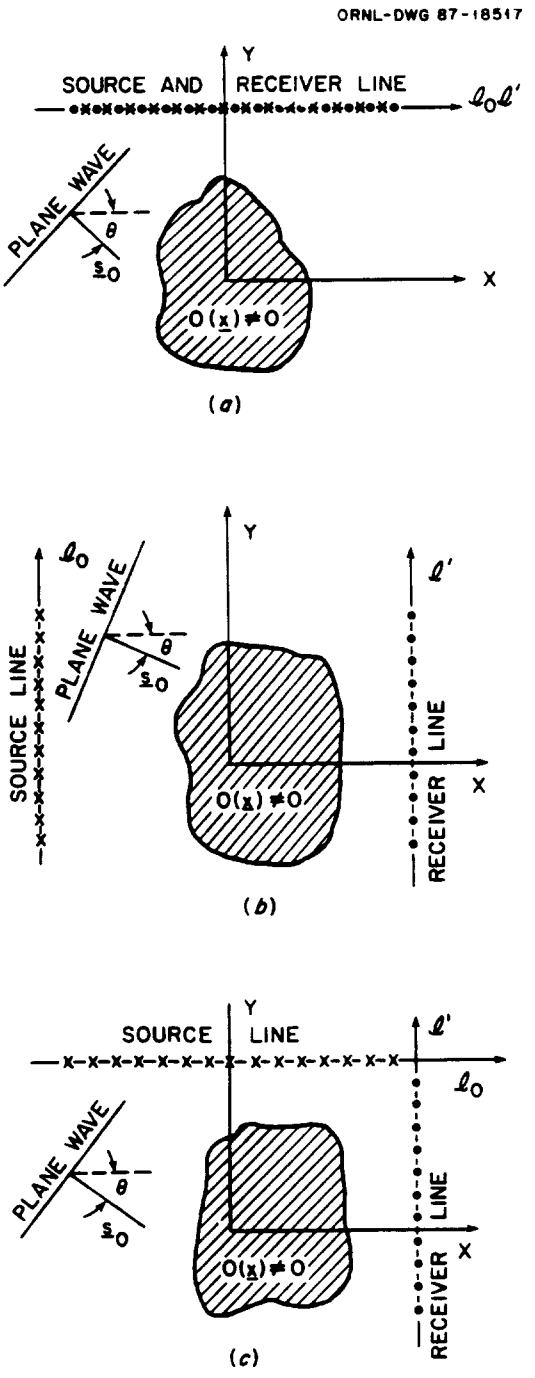

Figure 13: Notation used in formulating the geophysical diffraction tomography algorithm in (a) surface-to-surface, (b) cross-borehole, and (c) offset VSP geometry.

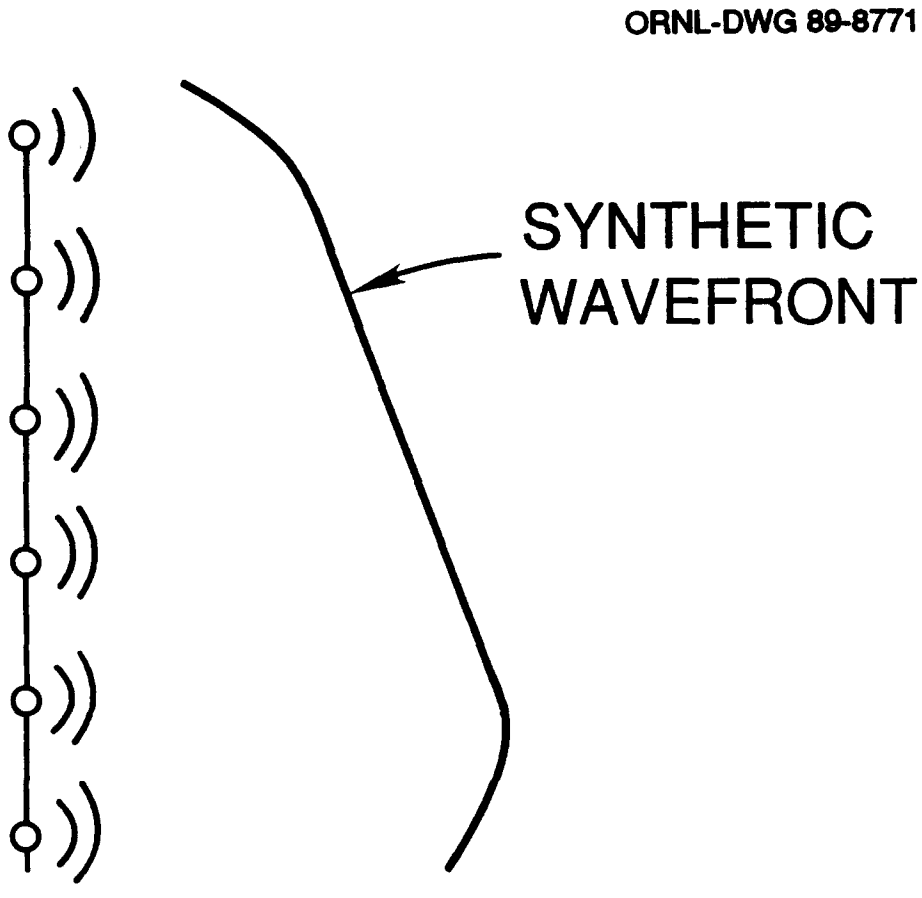

Figure 14: "Edge" effects associated with the synthesis of a plane wave by slant-stacking.

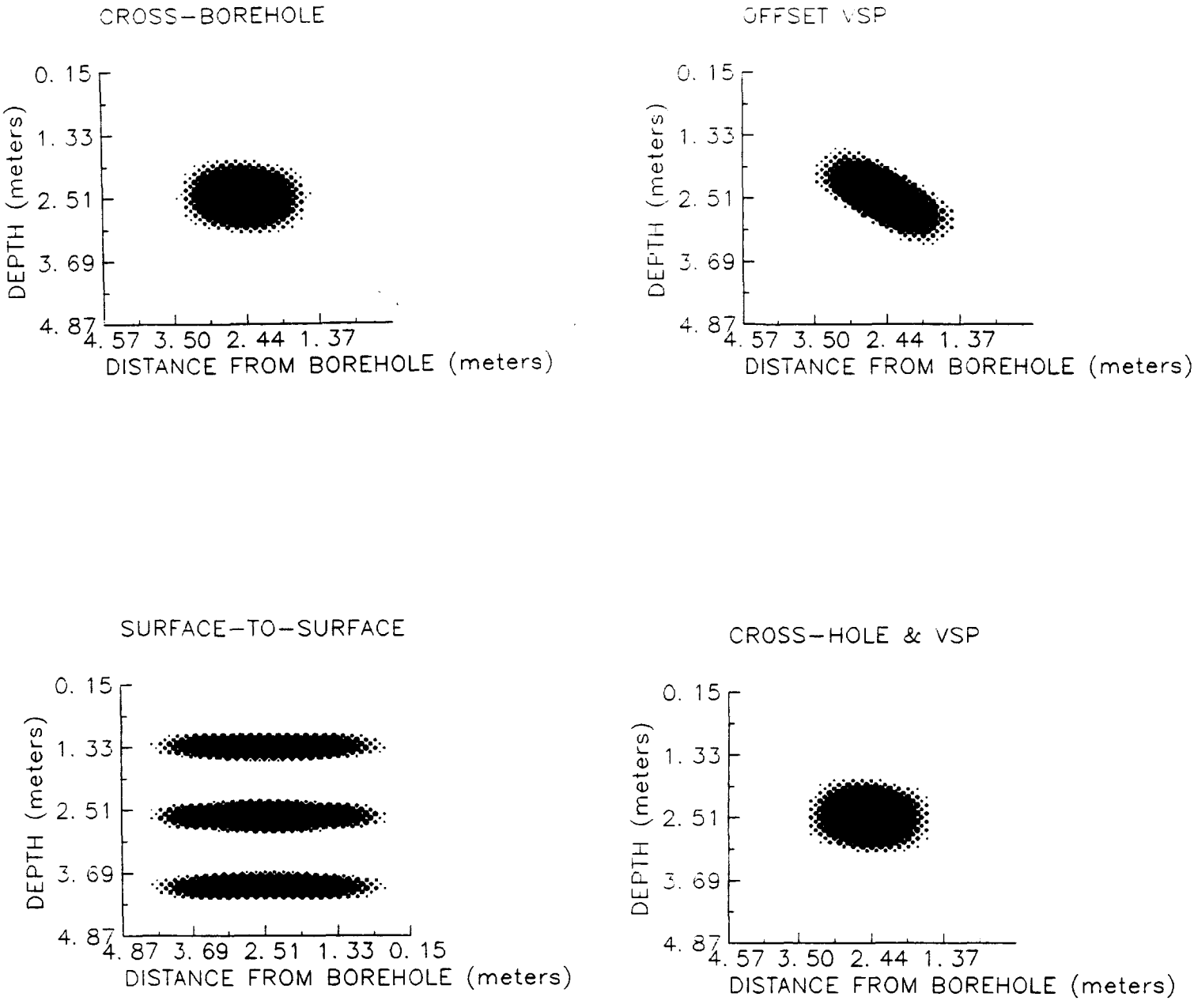

Figure 15: Synthetic images of a circular disk for a (a) cross-borehole, (b) offset VSP, (c) surface-to-surface, and (d) composite cross-borehole and offset VSP geometry.

angles. It is clear that the differences in image quality between cross-borehole [Fig. 15(a)] and offset VSP [Fig. 15(b)] are slight; however, the image quality attainable from purely surface measurements [Fig. 15(c)] is unsuitable for most applications. In summary, reflection view angles are of little value as a primary source of information and are best utilized as a supplement to sharpen images.

Along with the three primary configurations described above, composite geometries can be used to further improve image quality. One such composite geometry is surface to two borehole which provides the same range of view angles as offset VSP; however, here improved image quality results because all view angles are associated with transmission. An example of the use of this geometry is given in the next chapter. Another composite system is combined cross-hole and offset VSP where 180^0 of transmission angles and an additional 90^0 of backscatter angles can be realized. Figure 15(d) is an example of a simulated image from this geometry.

The offset VSP configuration appears to be best suited for shallow applications associated with environmental problems because it provides good image quality, avoids the complications of a downhole energy source, and allows for the imaging of multiple cross-sections from a single borehole. For imaging in a cross-borehole configuration, two boreholes are required to image each cross-section and one additional borehole would be required for each additional cross-section. Multiple cross-sections or a three-dimensional image can be obtained in the offset VSP configuration by the deployment scheme illustrated in Fig. 16.

The remainder of this chapter deals with the field instrumentation and implementation for GDT in an offset VSP configuration.

4.2 Instrumentation

The data acquisition system consists of the four hardware subsystems represented in Figure 17 plus the associated operating software. Each of the separate components are described below.

Noise Source — The propagating sound wave is produced by a commercially manufactured 8-gauge seismic gun known as "BETSY." BETSY, shown in Fig. 18 fires a 85 g slug downward producing a hemi-spherical wave front with an initial energy of 12.2 KJoule. The normal frequency spectrum for this source shows the majority of the energy is in the 25-250 Hz range. A typical signature from one source firing is shown in Fig. 19. Two critical parameters associated with seismic gun operations are proper coupling to the ground and accurate location of the source with respect to the borehole. Coupling determines the efficiency in transferring energy to the ground. This directly impacts the signal-to-noise ratio and the effective distances for wave propagation. Location of the source is an important parameter affecting variability of results. Sampling procedures present in the following subsection describe methods utilized to properly locate and couple the source.

Hydrophone Receivers — Signal collection is accomplished by 29 hydrophones and preamplifiers assembled into a sealed, oil-filled streamer (Fig. 20). These hydrophones are commercially available and offer good frequency response in the range from several Hz to several

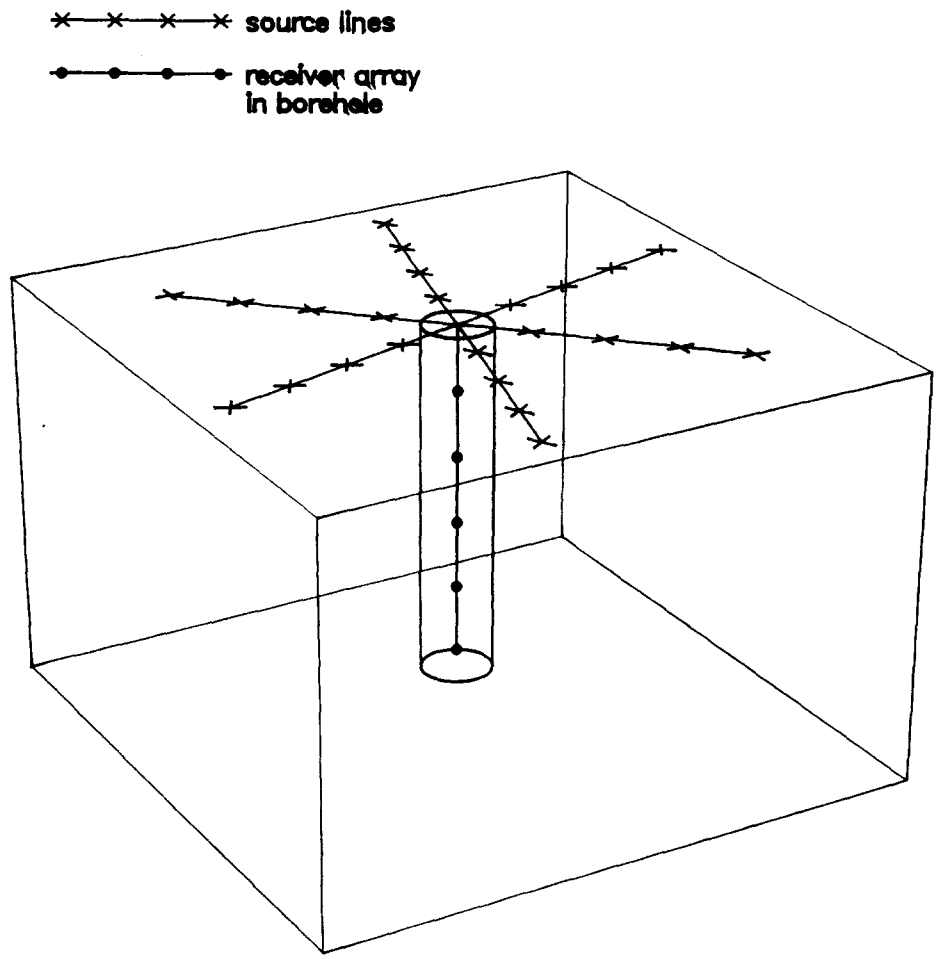

Figure 16: Illustration of the manner in which multiple cross-sections may be surveyed from a single borehole using the offset VSP configuration.

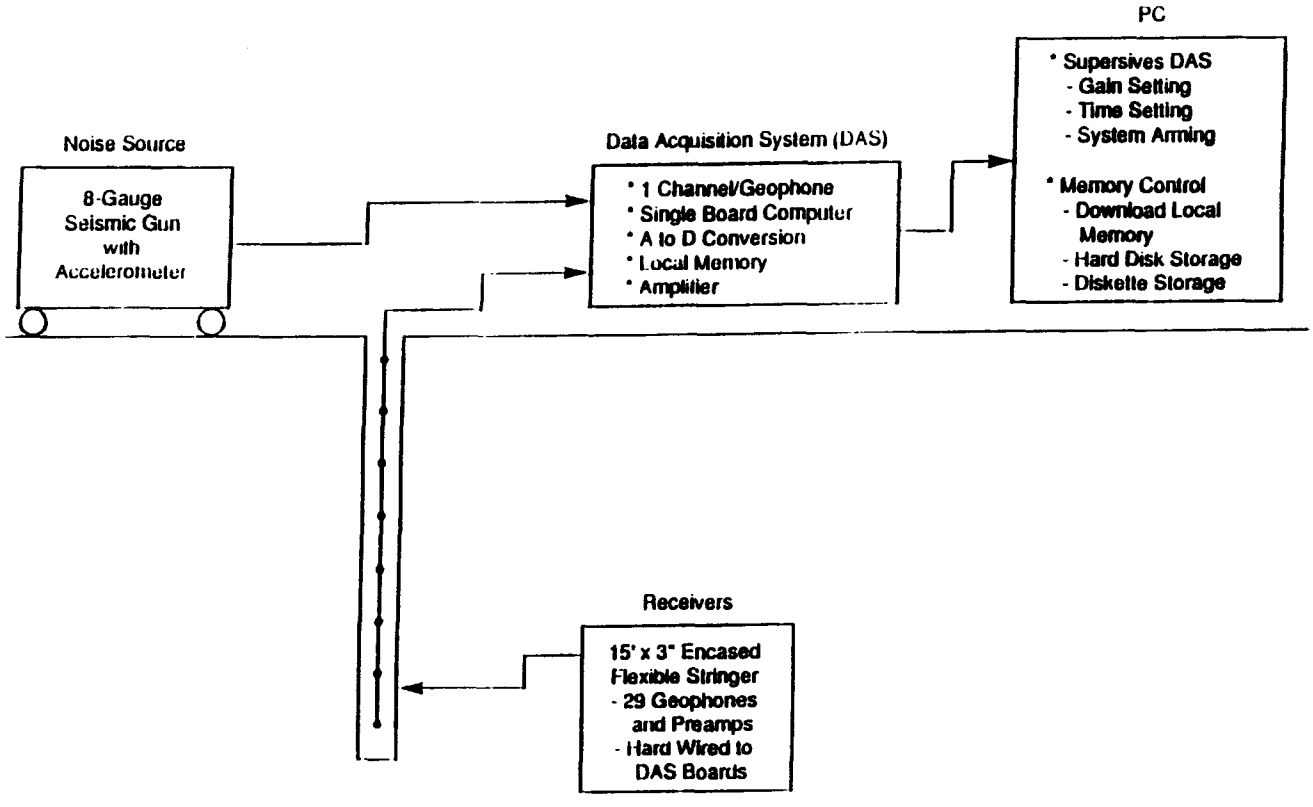

Figure 17: Schematic of the field system used to implement geophysical diffraction tomography.

Figure 18: Photograph of the acoustic source (BETSY seisgun) used in field studies.

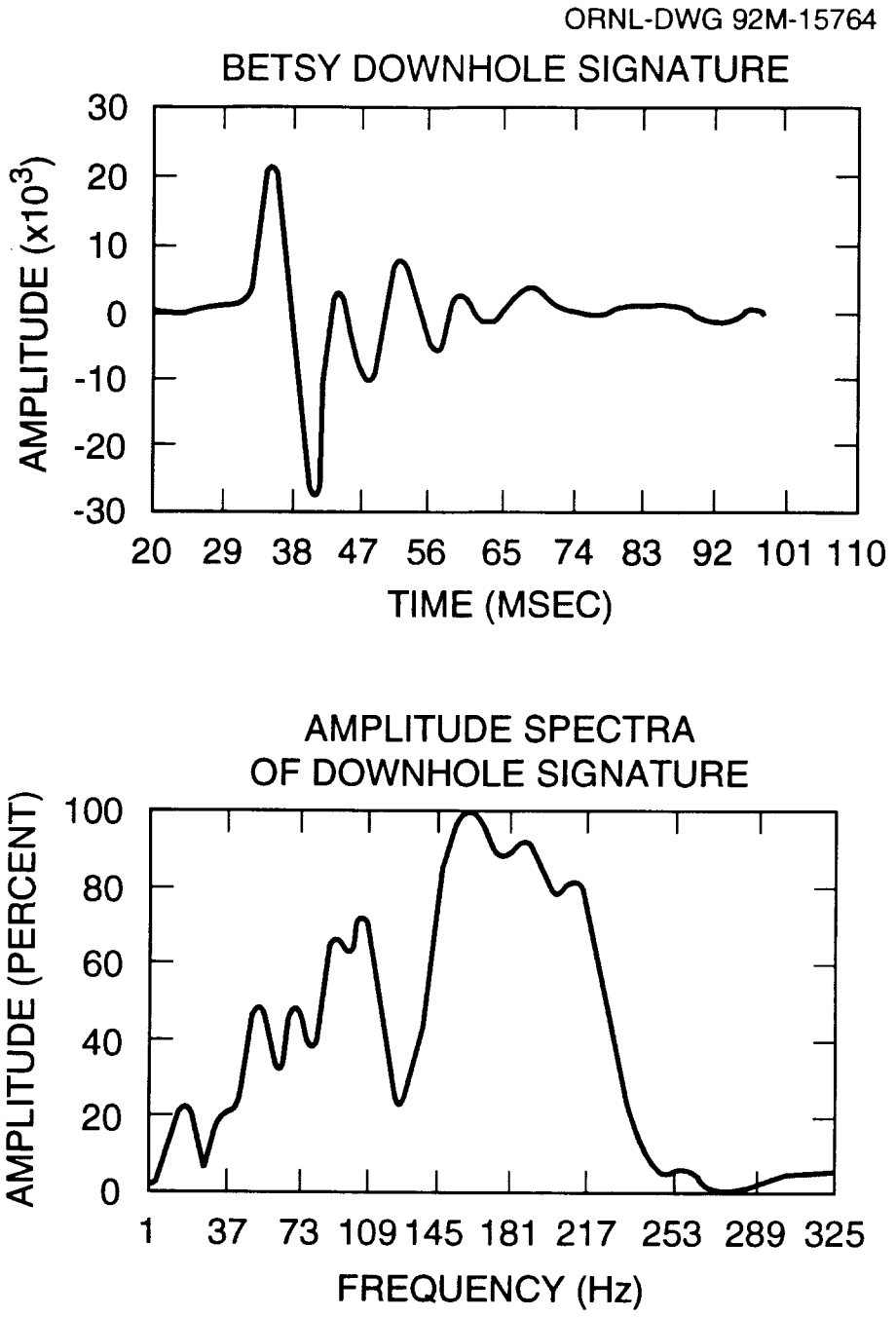

Figure 19: Typical time series and power spectrum produced by the BETSY seisgun (Source: Martin, P. N., "Betsy M3 seisgun source," Betsy Seisgun Inc., October 1986).

Figure 20: Close-up photograph of a portion of the hydrophone/preamp streamer.

KHz. Each set is hardwired to a separate channel of the data acquisition system. The streamer is lowered into a water-filled hole to the desired depth (Fig. 21). Utilizing a water-filled hole provides a stronger received signal by promoting better acoustic coupling between hydrophones and the formation.

Data Acquisition System DAS — The DAS consists of 32 identical data collection channels assembled on 8 separate computer boards. Each channel includes an analog-to-digital converter, an amplifer, local memory, and access to a single board computer. Channels are programmable for signal gain, sampling period, and number of sample points. Data collection is initiated by the system's electronic trigger actuated by a signal from an accelerometer attached to the BETSY. Figure 22 shows the DAS along with the supervisory computer being operated in the field.

Supervisory Computer — Because the hardware system was necessarily constructed before final field methods were known, the system was designed to provide maximum flexibility in operation. Key to obtaining this flexibility was incorporation of on-line control through a supervisory computer. In general, the computer is used to input the data collection parameters executed by the DAS and to provide permanent memory for the collected data. Current system configuration employs a COMPAQ Portable 386 personal computer equipped with a data acquisition board specially designed to communicate with the DAS. The computer includes a 40 mega-byte permanent memory and one high density diskette drive. Specifics of operation are provided in the following section which described the DAS controller functions operating on the supervisory computer. For efficiency all data acquisition software is written in FORTH, a relatively low-level programming language.

4.3 Field Operations

The field operations necessary for implementation of GDT include site preparation, definition of source lines, data acquisition, and signal processing. The elements are described individually below.

Site preparation — It is necessary to suitably prepare a site for the deployment of sources and receivers. This requires a 4 in diameter borehole to accommodate the receiver array. A dry or uncased hole can be used but, as noted above, a water-filled hole is more desireable. When preparing a site from scratch, a 6 in diameter hole is drilled and a 4 inch id PVC casing capped on the bottom is placed in the hole. The annular region between the casing on the borehole is backfilled with sand or available site materials to improve acoustic wave coupling. It is not critical to the method to rigorously follow these borehole development procedures. Suitable monitoring wells can be used as well as open core holes if available.

Definition of source lines — The acoustic source (BETSY) must be fired at predetermined intervals along a line radially outward from the borehole containing the hydrophone array. While this line does not have to be horizontal it should be as flat as possible. Energy produced by the seismic gun and propagated for some subsurface distance without substantial

KHz. Each set is hardwired to a separate channel of the data acquisition system. The streamer is lowered into a water-filled hole to the desired depth (Fig. 21). Utilizing a water-filled hole provides a stronger received signal by promoting better acoustic coupling between hydrophones and the formation.

Data Acquisition System DAS — The DAS consists of 32 identical data collection channels assembled on 8 separate computer boards. Each channel includes an analog-to-digital converter, an amplifer, local memory, and access to a single board computer. Channels are programmable for signal gain, sampling period, and number of sample points. Data collection is initiated by the system's electronic trigger actuated by a signal from an accelerometer attached to the BETSY. Figure 22 shows the DAS along with the supervisory computer being operated in the field.

Supervisory Computer — Because the hardware system was necessarily constructed before final field methods were known, the system was designed to provide maximum flexibility in operation. Key to obtaining this flexibility was incorporation of on-line control through a supervisory computer. In general, the computer is used to input the data collection parameters executed by the DAS and to provide permanent memory for the collected data. Current system configuration employs a COMPAQ Portable 386 personal computer equipped with a data acquisition board specially designed to communicate with the DAS. The computer includes a 40 mega-byte permanent memory and one high density diskette drive. Specifics of operation are provided in the following section which described the DAS controller functions operating on the supervisory computer. For efficiency all data acquisition software is written in FORTH, a relatively low-level programming language.

4.3 Field Operations

The field operations necessary for implementation of GDT include site preparation, definition of source lines, data acquisition, and signal processing. The elements are described individually below.

Site preparation — It is necessary to suitably prepare a site for the deployment of sources and receivers. This requires a 4 in diameter borehole to accommodate the receiver array. A dry or uncased hole can be used but, as noted above, a water-filled hole is more desireable. When preparing a site from scratch, a 6 in diameter hole is drilled and a 4 inch id PVC casing capped on the bottom is placed in the hole. The annular region between the casing on the borehole is backfilled with sand or available site materials to improve acoustic wave coupling. It is not critical to the method to rigorously follow these borehole development procedures. Suitable monitoring wells can be used as well as open core holes if available.

Definition of source lines — The acoustic source (BETSY) must be fired at predetermined intervals along a line radially outward from the borehole containing the hydrophone array. While this line does not have to be horizontal it should be as flat as possible. Energy produced by the seismic gun and propagated for some subsurface distance without substantial

Figure 21: Photography of the streamer being lowered into a monitoring well.

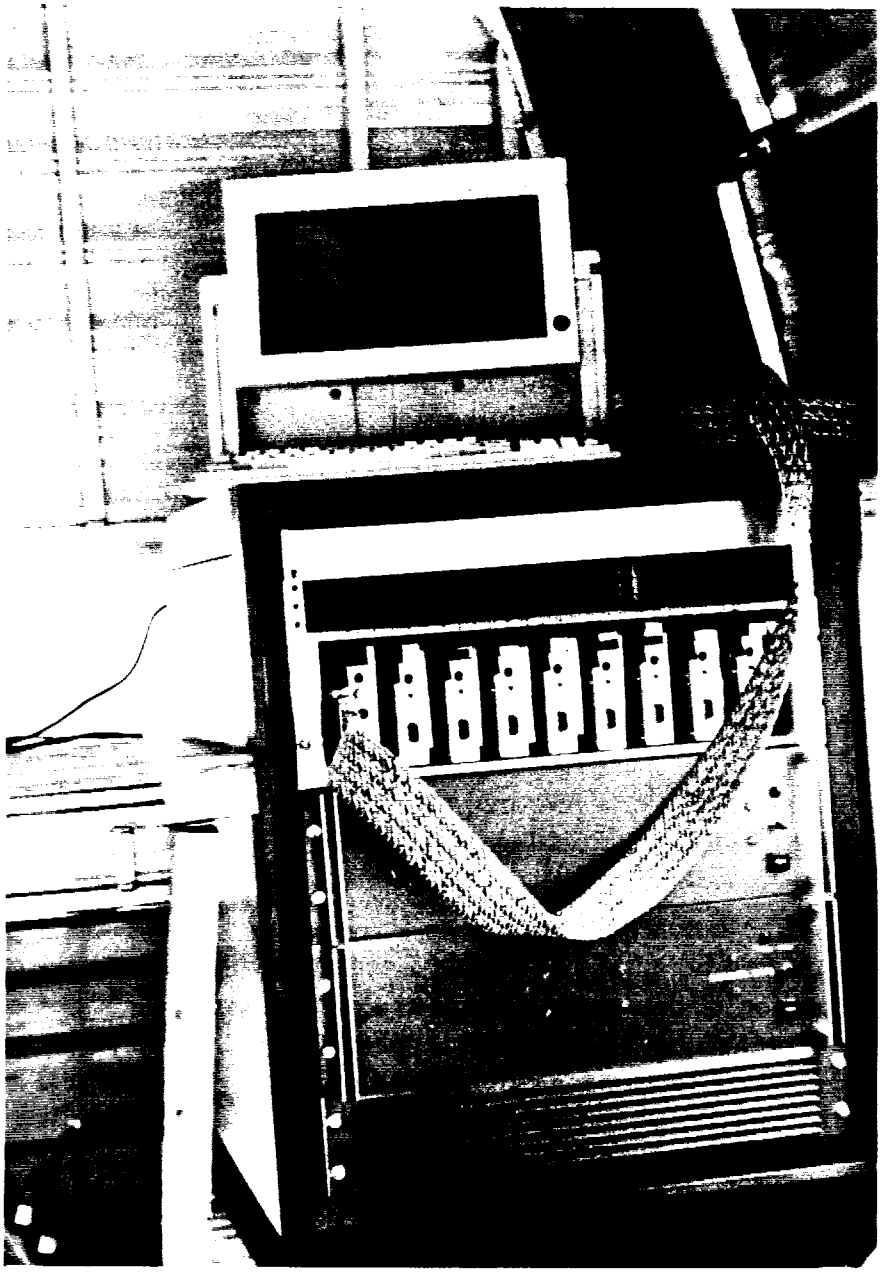

Figure 22: Photograph of the data acquisition system (DAS) and supervisory computer.

attenuation losses lies in the 10-300 Hz spectral range. The resolution limits of GDT are wavelength-dependent with the smallest inclusion which can reliably be imaged being about a quarter of a wavelength. The actual wavelengths which can be realized are defined by the relationship $\lambda = c_0/f$, where λ is the wavelength, c_0 is the reference sound speed at the site, and f is the frequency considered. Thus, the best possible resolution which can be achieved is defined by the maximum possible frequency which can be propagated. In practice, however, there is a trade-off because higher frequencies are more rapidly attenuated and, as a result, this limits the horizontal extent of the region which can be imaged from a single borehole. Furthermore, the implementation of GDT requires the spatial resolution of the propagated wave which, in turn, requires source positions to be established at half wavelength intervals. In other words, increased resolution requires more data collection and limits the distance the source can be moved from the borehole. These points must be considered when establishing the source deployment scheme.

The above discussion also influences site preparation. A source line must be established with source firing locations occurring every half wavelength. Minor deviations in source position are acceptable provided such deviations are not more than about one eighth of a wavelength. Surface irregularities and obstructions such as trees can be avoided by relocation of the source provided that such a deviation is much smaller than one wavelength. As a result, at some sites minor (hand) grading may be required or imaging must be accomplished at a lower frequency.

Figure 23 is a photograph of a prepared site with cased boreholes in place and grading stakes located to guide source positioning.

Data acquisition — The data acquisition system developed for the initial field implementation of GDT was designed to be quite flexible and a recent modification to the software which controls the acquisition of data makes use of the system both efficient and user-friendly. Figure 24 is a photograph of the user menu appearing on the monitor of the supervisory computer. The shaded area occupying most of the screen is used to input and display selected data acquisition parameter, while the box in the lower right corner displays supplemental commands. The elements of the main menu and supplement commands are described below.

Main Menu

1. File name: The user inputs a master file name for each cross-section to be surveyed. For example a file name TEST may be used. A separate file of time series from all hydrophones is created and stored on the hard disk. The procedure assumes that the first location for the source is the one nearest to the borehole. Following each data acquisition, data is stored in a file TEST01.DAT for the first source position, file TEST02.DAT for the second source position, etc. Once data acquisition begins, the file name corresponding to a particular source location is automatically displayed.

2. No. of samples: The user may input the total number of samples in time (up to 512) to be digitized and stored for each hydrophone.

Figure 23: Photograph of the Chestnut Ridge site as prepared for the tomography field study.

ORNL-DWG 90M-6474

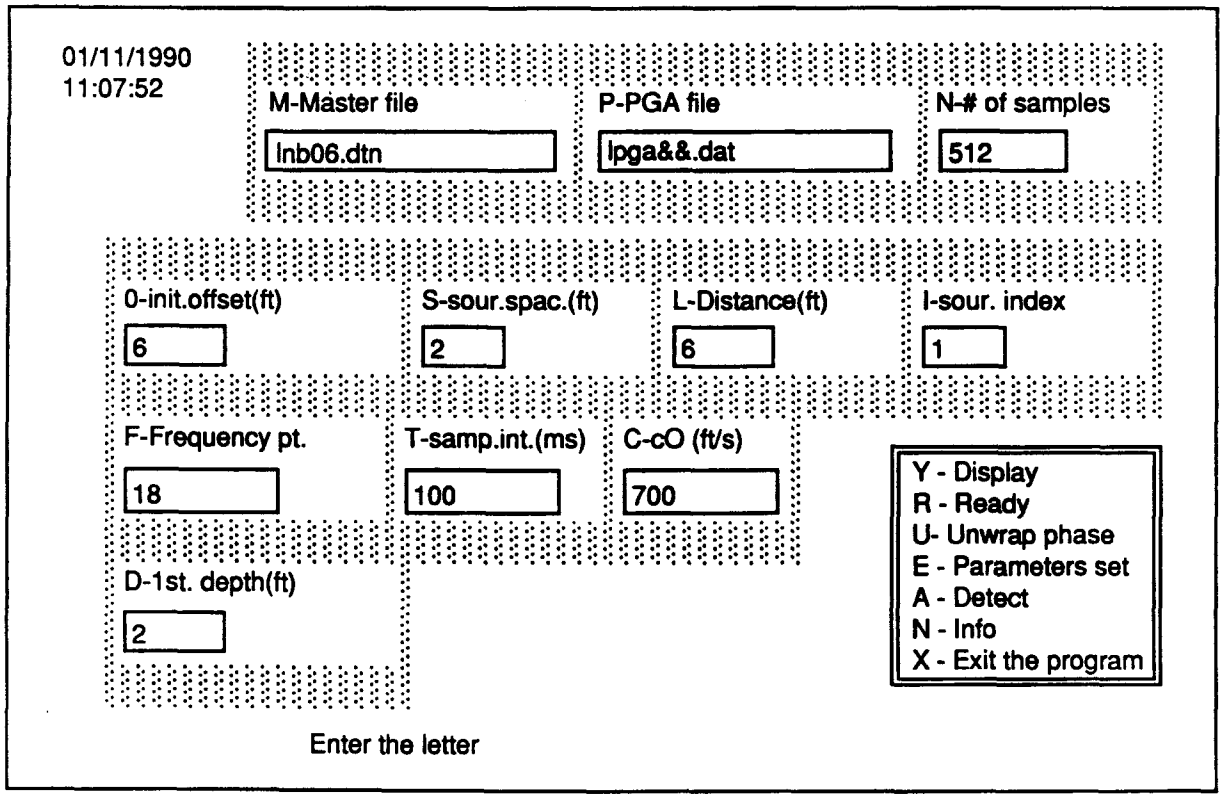

Figure 24: Illustration of the interactive user menu which controls data acquisition.

3. Sampling interval: The user inputs the time interval in microseconds between each digitization. The total length of the acquired time series (in microseconds) is the product of the sampling interval and number samples.

4. Initial source position: The user inputs the distance of the source from the borehole at its initial location.

5. Source spacing: The user inputs the distance between successive source positions.

6. Source index: Displayed here is an index which defines the incremental source position. This is 1 for the first source position, 2 for second position, etc. The user may change this value to access data collected for a previous source location. Changing the source index will result in a change in the displayed file name to correspond to the data file being accessed.

7. Source position: Displayed here is the distance between the source and the borehole for the current source position. This is automatically updated based on the current source index, initial source position, and source spacing. Changing the source index or file name will result in a corresponding change in the displayed file name, source index, and source position.

8. Frequency point: The user inputs a frequency index at which imaging is to be performed. This is stored for use in later signal processing.

9. Sound speed: The user inputs a reference sound speed for the site being studied. This is stored for use in later signal processing.

10. First depth: Depth of shallowest hydrophone in the array.

11. PGA file: Name of file containing gain settings for the programmable gain amplifiers.

Supplemental Commands

1. Ready: This command downloads sampling parameters from the supervisory computer to the DAS prior to source firing. Following data acquisition, the user is prompted to strike any key. The response to this prompt causes the data retained in local memory of the DAS to be downloaded into the current file name displayed on the main menu and stored on the hard disk. Added to each data file is a heading containing all unique parameters currently displayed on the main menu. This also automatically increments the file name, source index, and source position displayed on the main menu.

2. Display: The display command allows the user to view a plot of the time series for any hydrophone from the file currently displayed under file name (Fig. 25). Display is typically used periodically to verify the system is acquiring data correctly and to check that the gain setting is appropriate. The user may review data acquired for a previous position by changing the displayed file name or source index.

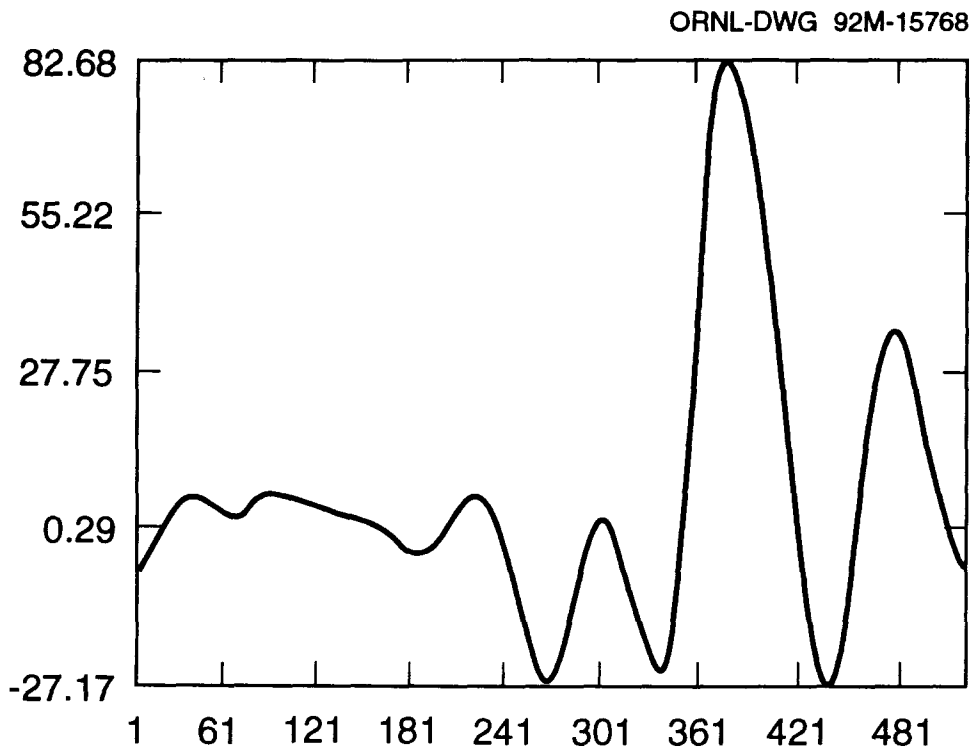

Figure 25: Data time series produced by execution of the supplemental DISPLAY command.

3. Unwrap: This command executes an initial signal processing step. This is the computation of the principal value of the acoustic wave phase and its total value obtained by a phase unwrapping procedure (see Appendix A). A plot of the unwrapped phase as a function of receiver position appears on the PC monitor following completion of these computations (Fig. 26). The unwrapped phase data is stored separately in a two-dimensional array. Following each source firing and phase unwrap, another column is added to this array. This processed data is used by the imaging software for all acquired data. The computational speed of the COMPAQ Portable 386 allows the phase unwrapping to be accomplished during the time required to reposition the source. Performing this operation during the data acquisition phase saves about 15 min in signal processing time later.

4. Detect: Relative changes in phase as a function of depth between adjacent or nearby source positions suggests the presence of inhomogeneities. The approximate location and nature (layers, isolated inclusions, etc.) of inhomogeneities may be inferred by visual examination of selected phase plots such as the one shown in Fig. 26. By invoking Detect, the user can view, simultaneously, up to six selected phase plots in order to establish preliminary information regarding subsurface conditions. Detect can be invoked any time during the data acquisition operation. Figure 27 is an example of the display created by Detect.

5. Info: Following completion of data acquisition and signal processing all raw and processed data can be archived on diskette. The Info command allows the user to interactively create a text file describing experimental conditions and other observations. This file can then be incorporated in the information contained on diskette.

6. Parameter set: This command calls another menu which allows the user to establish gain files for the programmable gain amplifiers and to invoke diagnostic software used to verify proper communications between the supervisory PC and the DAS.

The above described data acquisition procedure was designed to be both efficient and user-friendly. Data acquisition proceeds with a minimum of user intervention so there is little opportunity for user-induced error. The user has displayed before him at all times all relevant parameters associated with the experimental procedure and appropriate diagnostic functions to allow easy and rapid identification of system malfunctions. This data acquisition procedure is quite fast with a proven speed (including data acquisition, data storage, and preliminary signal processing) of one source firing at least every minute.

Signal processing — Following the completion of data acquisition for an individual surveyed cross-section, the sequence of signal processing steps outlined in Fig. 28 can be executed to create images in near real time in the field. The mathematical details associated with these steps are given in Appendix A.

The first step of the signal processing procedure is to compute the perturbed phase. This is the difference between the actual total as determined by the phase unwrapping procedure

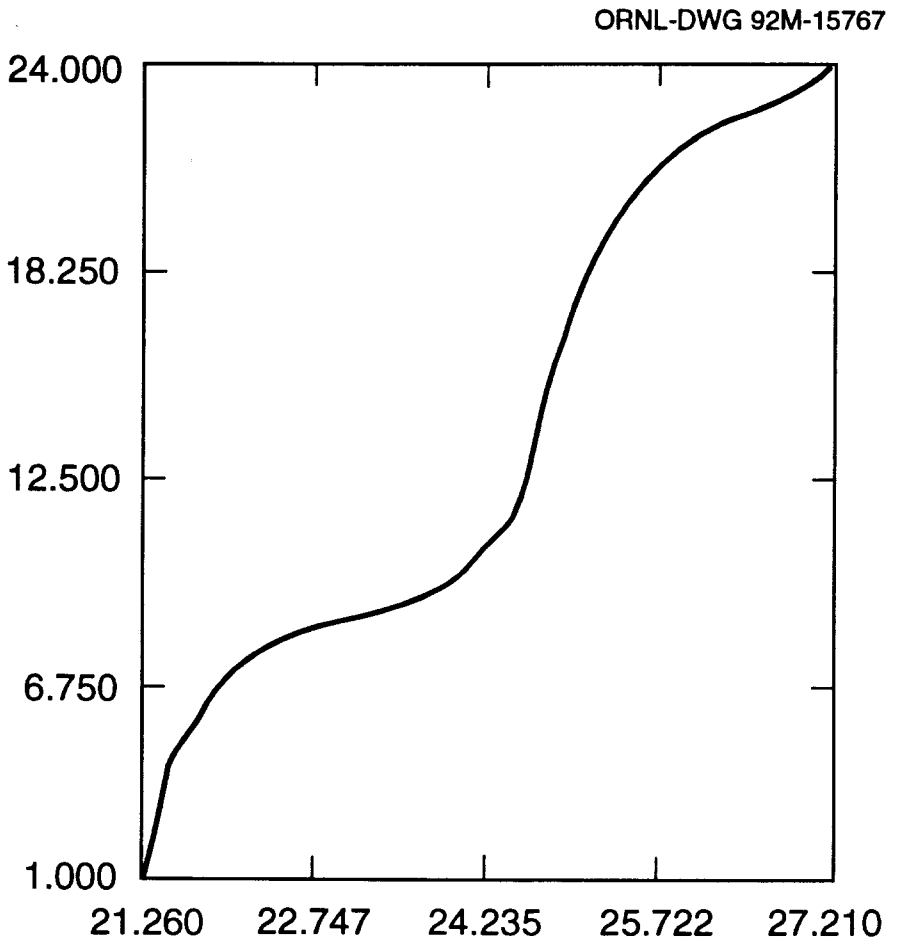

Figure 26: Unwrapped phase as a function of receiver index produced by execution of the supplemental UNWRAP command.

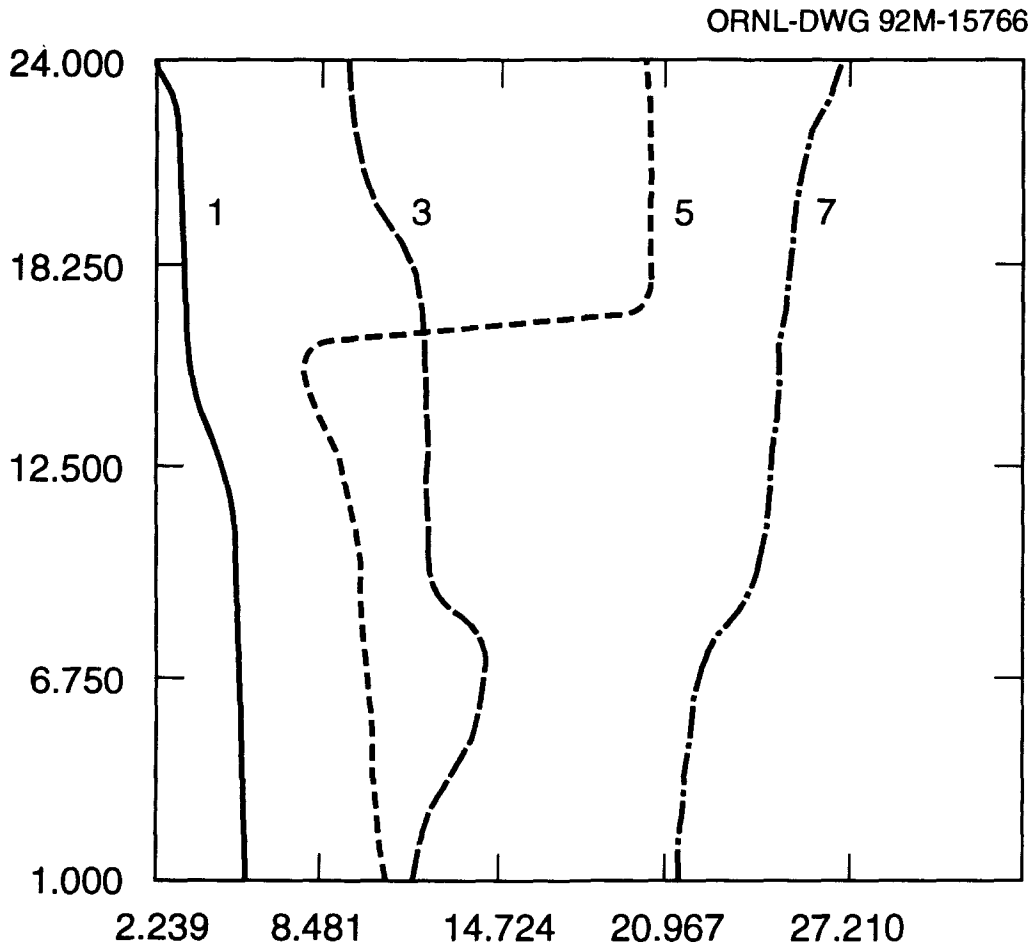

Figure 27: Example of graphical output produced by execution of the supplemental DETECT command.

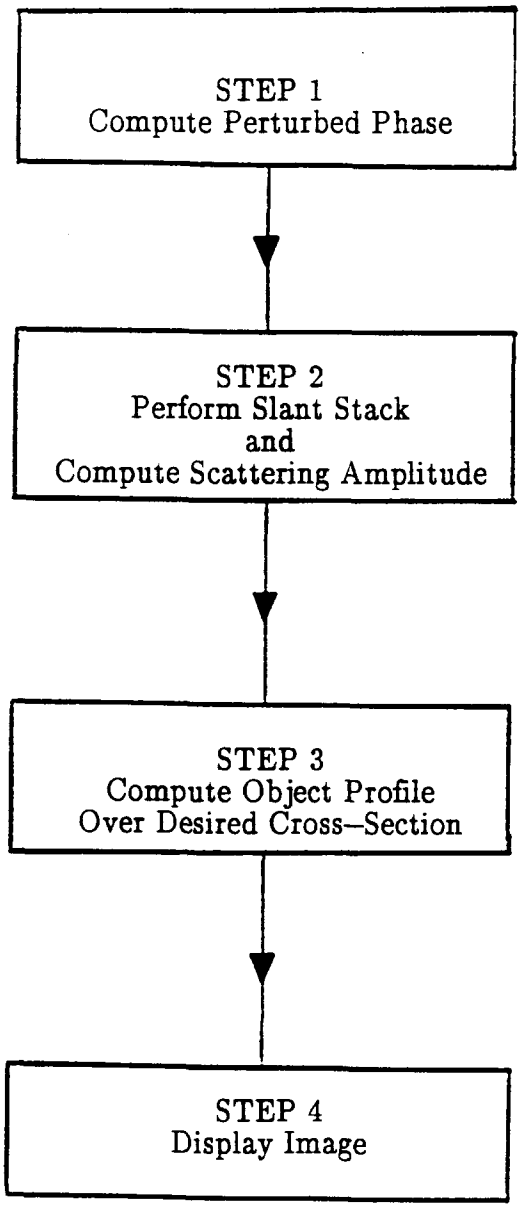

Figure 28: Schematic of the sequence of signal processing steps necessary to produce an image following data collection.

and that which would have been measured if propagation occured in a homogeneous medium. Recalling the discussion of the physical analogy of GDT to optical holography, given in the previous chapter, this step is the one which corresponds to the formation of an interference pattern created by the interaction action of the target laser beam with the reference beam.

The next step in the procedure is the slant-stack to simulate plane (coherent) wave illumination [eq. (12)] and the computation of scattering amplitude [the application of the numerical holographic lens, eq. [(13)]. In this step the user must specify the number of viewing angles to be used as well as specify a range of view angles between 0^0 and 180^0. This selection must be made judiciously to avoid image artifacts.

The third step in the procedure, is the numerical inversion of the spatial Fourier transform of the object profile [eq. (14)]. The user specifies the horizontal extent and resolution of this computation. The selection of the horizontal extent must be compatible with the range of view angles selected in the previous step to avoid image artifacts.

The final step in this procedure is the graphical display of the resulting image. The means of display utilized in the field is a pseudo gray scale image produced on the PC monitor with dark levels of gray corresponding to increasing relative values of sound speed. A hard copy of the result can be obtained in the field through the use of a dot matrix printer and the PRINT SCREEN command. Figure 29 is an example of an image as produced in the field. The image is somewhat "blocky" and limited to only 15 gray levels. This is a result of the limited number of addressable pixels available on the monitor of the supervisory PC. The image quality can be improved by using recently-available portable PC's with high-resolution monitors. As will be seen in the next chapter, final images of far superior quality can be achieved using a dot-matrix or laser printer.

The signal processing software described here is quite efficient, typically requiring about 2 min for all data analysis and display.

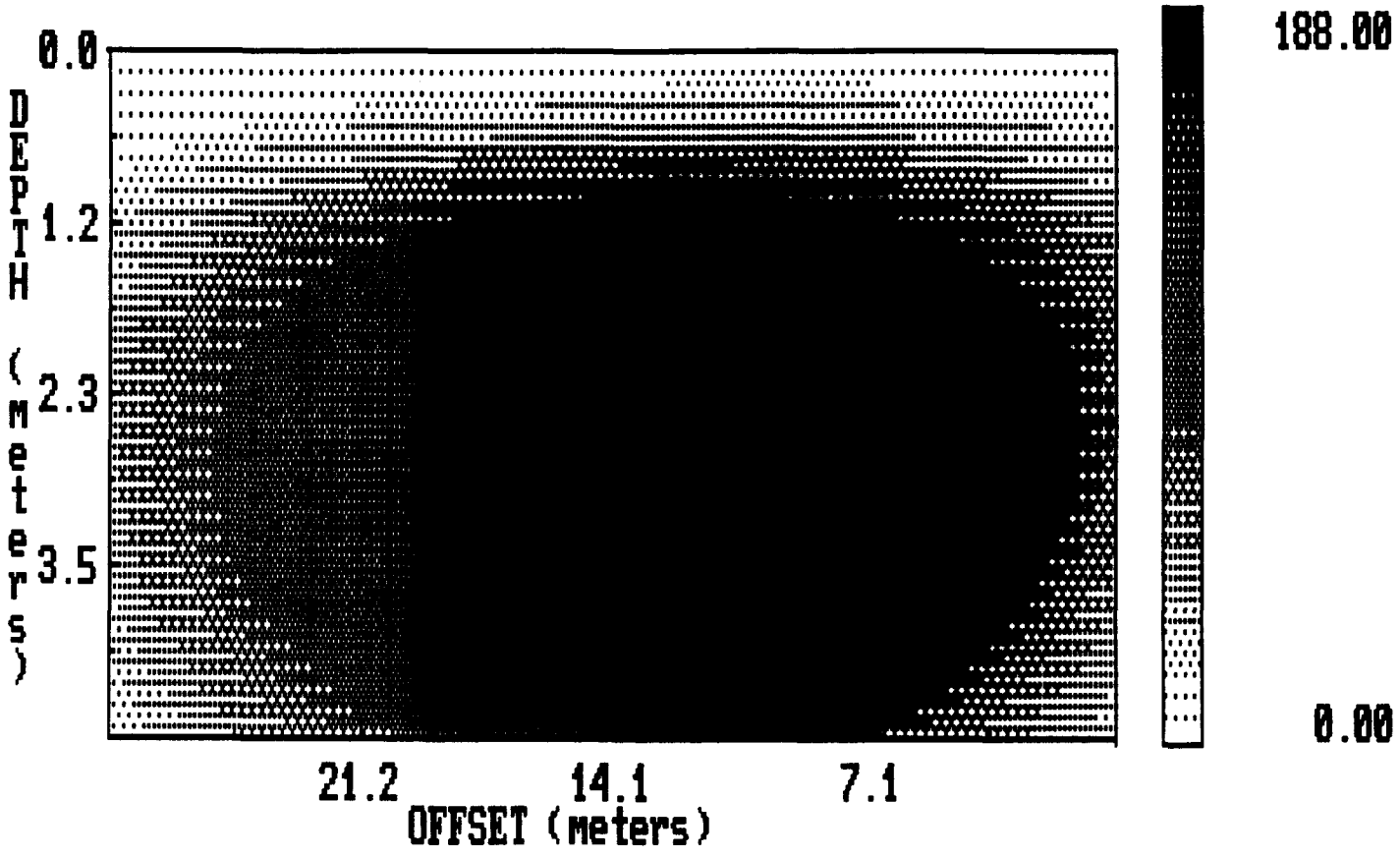

Figure 29: Example of an image as it appears on the monitor of the supervisory computer.

5 RESULTS

This chapter presents results to date on the implementation of geophysical diffraction tomography from five field tests performed at four sites. These are presented in chronological order and each successive test was executed to either validate or improve the technology. The images present here, unless otherwise noted, display gray scales where increasingly darker shades of gray indicate increasing sound speeds of subsurface features. In interpreting these images it is important to realize that sound speed is a composite function of both density and compressibility. Thus, an elevated sound speed relative to background can be the result of an increased density, decreased compressibility, or both. The opposite is true for features displaying sound speeds which are less than background.

5.1 Chestnut Ridge March 1987 Survey

This field study was conducted on the Oak Ridge reservation at a site on Chestnut Ridge between the Y-12 and X-10 areas. The target was a 0.6 m diameter cast iron water pipe buried approximately 1.2 m deep in clay soil. Two 0.15 m by 10 m deep boreholes were installed, one on each side of the cleared pipeline right-of-way. PVC casings equipped with bottom caps were installed in each hole and the outside of the wells were grounted with sand. The distance between the two boreholes was 15 m.

The source shot line was set by chaining in stakes every 1.2 m on a line between the two boreholes. Figure 30 is a plot of the site and Fig. 23 shows the site with the stakes installed. Initial source spacing was derived from the relations given in Witten and Long (1986). Using a representative source frequency of 200 Hz (from Fig. 19) and assuming an initial sound speed in the soil of 250 m/sec, a wavelength of 1.25 m was calculated. To image an object with a radius of 0.3 m this establishes the required source spacing at approximately 0.6 m. The sources were set to provide a horizontal coverage of from 1.2 to 13.4 m. The maximum source distance was limited by available working space. Depth of the receiver array (streamer) was selected to correspond to the anticipated depth of the buried pipe.

The field station for these tests was a pickup truck outfitted with a camper top. The DAS and supervisory computer were operated from the back of the truck. Power was supplied by a commercial 110-volt 650 watt gasoline powered generator. The system was assembled by wiring the computer into the DAS, the hydrophones to the individual boards in the DAS, and the accelerometer on the BETSY to the trigger circuit on the DAS. The streamer was positioned in the water filled borehole by setting the depth of the first hydrophone to a selected depth referenced to the ground surface.

Since this test was the first designed for the collection of data to support GDT, the site was selected because of the expected simple subsurface conditions; i.e., a buried pipe in otherwise homogeneous clay soil.

Figure 31 is a gray-scale image of relative sound speed variations derived for this field experiment. Most important is the clear indication of the pipe centered at 7.5 m from the receivers and 1 m deep. Also note that this image reveals subsurface conditions more complex

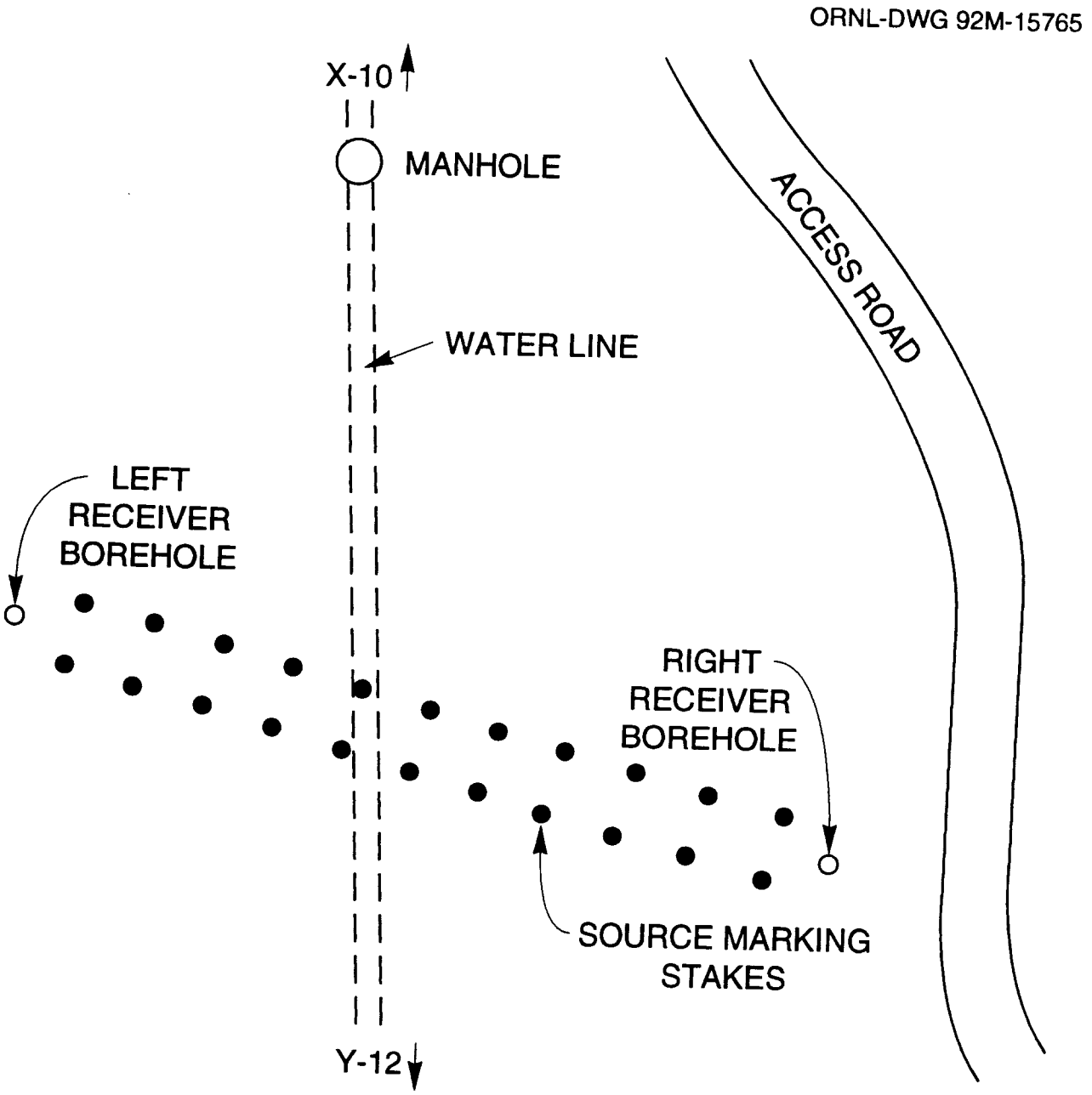

Figure 30: Site plan for the Chestnut Ridge test site.

ORNL-DWG 88-15631

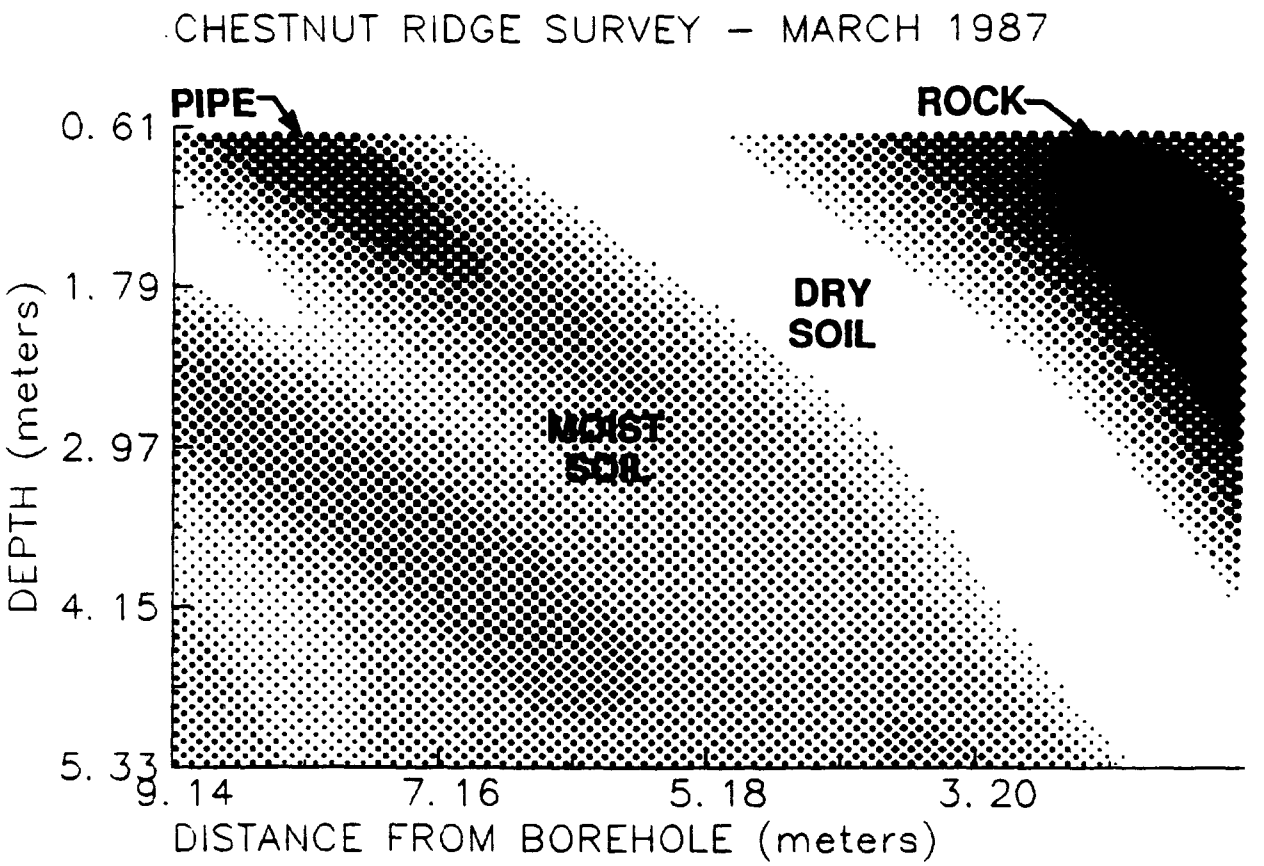

Figure 31: Gray-scale image of the Chestnut Ridge survey cross-section from the March 1987 field study.

than originally believed. The elongated shape of the pipe is caused by the offset geometry of the source/receiver configuration as discussed in Chapters 2 and 3 along with the fact that only transmission view angles were considered. Figure 32 is a synthetic reconstruction from perfect computer generated data of a circular disk in a homogeneous media. Comparison of the form of the actual result with the form of the optimum achievable result for the offset vertical seismic profiling configuration clearly demonstrates that GDT was successful in finding and imaging the pipe. The other features identifiable in Fig. 31, are an isolated area of high sound speed located close to the receiver array (shown as a black area), the shallow horizontal region of relatively dry soil (shown as a white area), and a transition with depth to a moist soil layer (shown as light gray) resulting from an extended period of rain prior to the field survey. Again, the system configuration tilts these inclusions in the direction of the ray path. This is particularly evident for the layer.

5.2 Chestnut Ridge October 1987 Survey

Verification of the methods and findings from the initial imaging experiment was accomplished by a resurvey of the site in October. The same field procedures as used in the March survey were followed here. The image produced from this study is presented in Fig. 33. This study was conducted during extremely dry conditions and absent are the fast regions supporting the original conclusion of their presence being transient elevated soil moisture. The pipe remains in approximately the same position as seen in Fig. 31 as does the fast shallow area near the borehole. The slight differences between the two reconstructions was caused by a change in initial receiver positions. For the first study the top receiver was 0.6 m deep while in the second it was only 0.15 m deep.

Also evident in the lower left of this image is an isolated region of elevated sound speed. This is likely a lens of more compressed soil. Although more subtle due to the surrounding soil moisture, this feature does appear in the March results (Fig. 31).

In addition to verification of the March survey, this field test was used to test a measurement geometry which should offer improved image quality.

One image artifact that can occur in transmission tomography is an elongation of features in the predominant direction of incident wave propagation. This is a result of the limited propagation or projection angles inherent in most measurement geometries. This elongation results from the resolution always being superior in the direction normal to the direction of propagation than in the direction parallel to the direction of propagation. Artifacts of this type are evident in some of the previously presented images and can be clearly seen in Fig. 33 which shows an image of a cross-section containing a 0.61 m diameter buried pipe and other identified features. This image is derived using the backpropagation algorithm applied to data collected in an offset VSP configuration with a borehole containing a receiver array located to the left of the imaged cross-section. For this geometry, the directions of propagation are all downward from right to left. The pipe, which should display a circular cross-section, is clearly elongated in the direction of propagation. A means to minimize this artifact is to implement a measurement geometry which offers a broader range of detectable

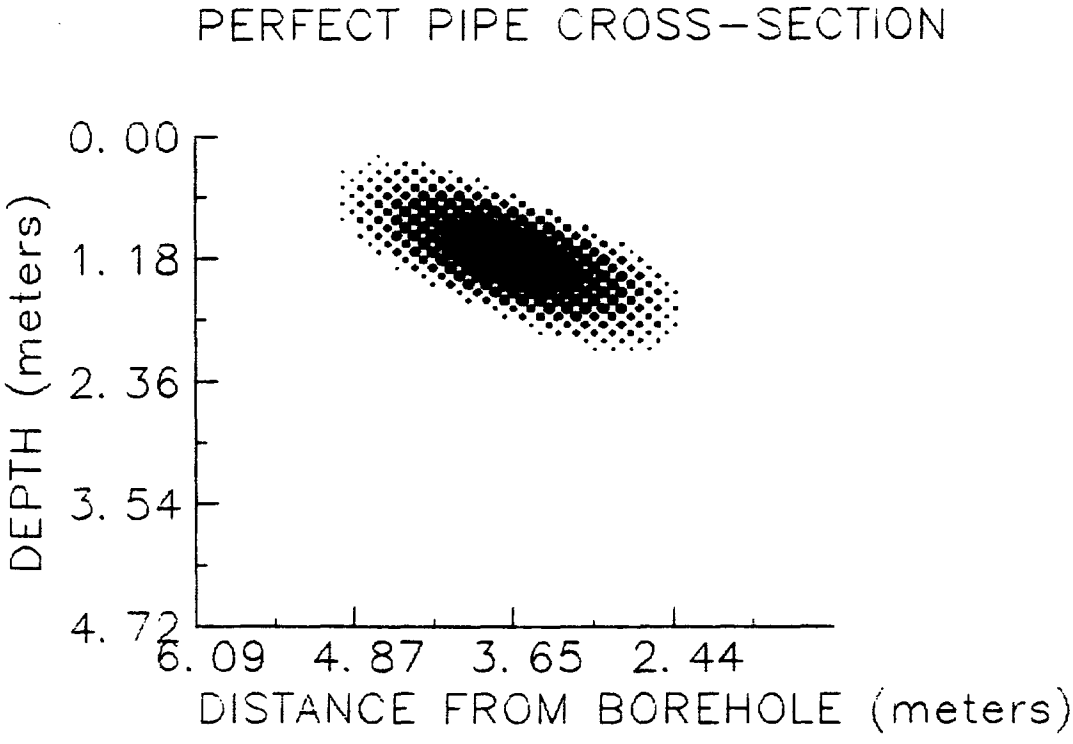

Figure 32: Gray-scale image of a circular pipe derived from simulated data.

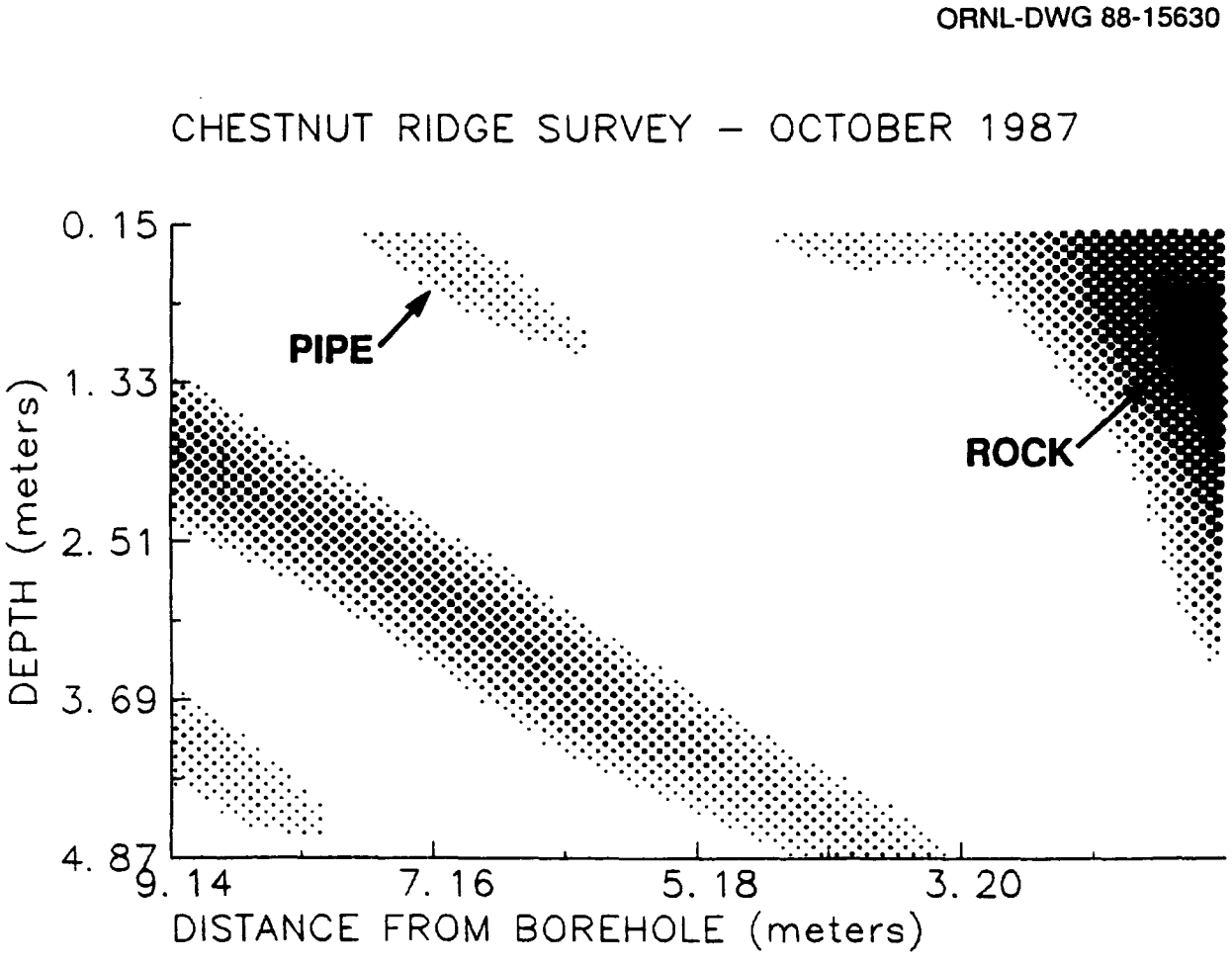

Figure 33: Gray-scale image of the Chestnut Ridge survey cross-section from the October 1987 field study.

incident propagation angles. Once such geometry is offset VSP using receiver arrays in two parallel boreholes with sources deployed on the ground surface between the two receiver arrays. This configuration doubles the available transmission viewing angles that can be used in the imaging procedure. This configuration was implemented for the same cross-section as shown in Fig. 33. The resulting image of the portion of the cross-section containing the pipe is given in Fig. 34. A comparison of Figs. 33 and 34 demonstrates a considerable improvement in image quality. Slight elongation still occurs; however, this is not believed to be an image artifact but due to the measurement geometry relative to the pipe. The cross-section defined by the subsurface region between the two boreholes is not perpendicular to the axis of the pipe. In this geometry the cross-section of the pipe should properly have a slight elliptic shape as portrayed in Fig. 34.

5.3 Bear Creek Valley March 1988 Survey

Following the successful completion of the two initial field studies, it was appropriate to conduct a more controlled field study directed towards the imaging of buried wastes. This was performed in the Bear Creek Valley area west of the Y-12 facility on the ORNL reservation. No boreholes were developed here, but rather, an existing PVC-cased monitoring well was used to house the hydrophone array. Coupling was maintained by periodically adding water to the well. Source locations were established in the same manner as described for the Chestnut Ridge surveys.

A second objective of this field study was to determine the increased data acquisition speed offered by the COMPAQ Portable 386 personal computer which replaced the previously used IBM-XT just prior to this field test. Several minor software changes were made to the data acquisition software to take better advantage of the new supervisory computer.

Two types of waste-simulating targets were selected for burial at predetermined locations on this site. These targets are 0.2 m^3 metal drums approximately 0.61 m in diameter and 1 m tall, both empty and water-filled, as well as plastic bags containing styrofoam packing peanuts of about the same dimensions as the metal drums. Six targets were deployed over the two subsurface cross-sections depicted as lines A and B in Fig. 35. An array of 29 uniformly spaced hydrophones spanning a 0.61 to 4.9 m depth interval was located in a cased monitoring well. Source positions were established every 0.61 m over two survey lines extending radially outward from the well containing the receiver array (Fig. 35). Source positions ranged from 1.2 to 14.6 m from the well along line A and from 1.8 to 14.6 m from the well along line B.

The resulting images of these two cross-sections are displayed in Figs. 36 and 37. The dominant features in the image of Line A are a fast area near the monitoring well identified as an area of folded and weathered shale observed in the excavation operations having a sound speed greater than the surrounding soil, the drum and the packing peanuts. The styrofoam packing peanuts appear in the image to have a sound speed slightly greater than the local soil. This result is unexpected because of the high compressibility of the target and may be caused by a blurring between this target and the fast adjacent weathered shale. Clearly

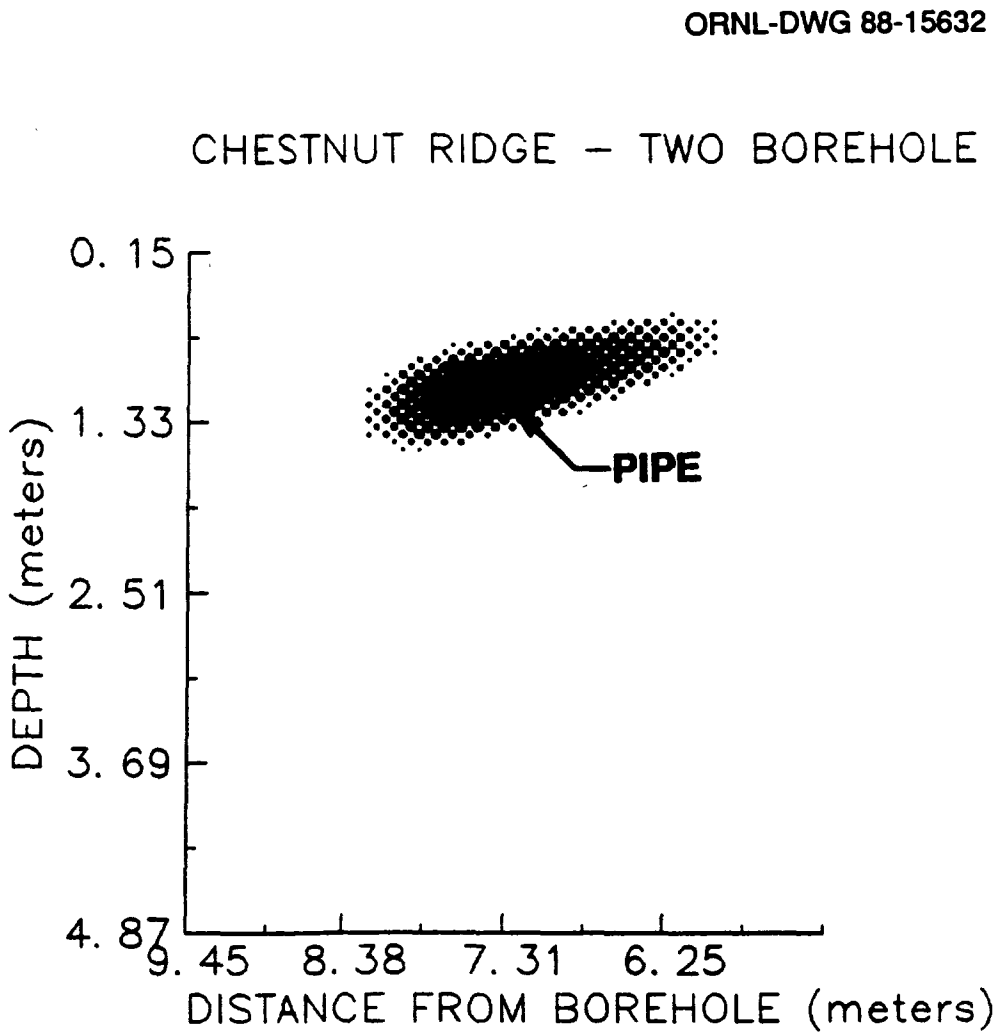

Figure 34: Gray-scale image of the buried pipe cross-section at the Chestnut Ridge site using data from two boreholes.

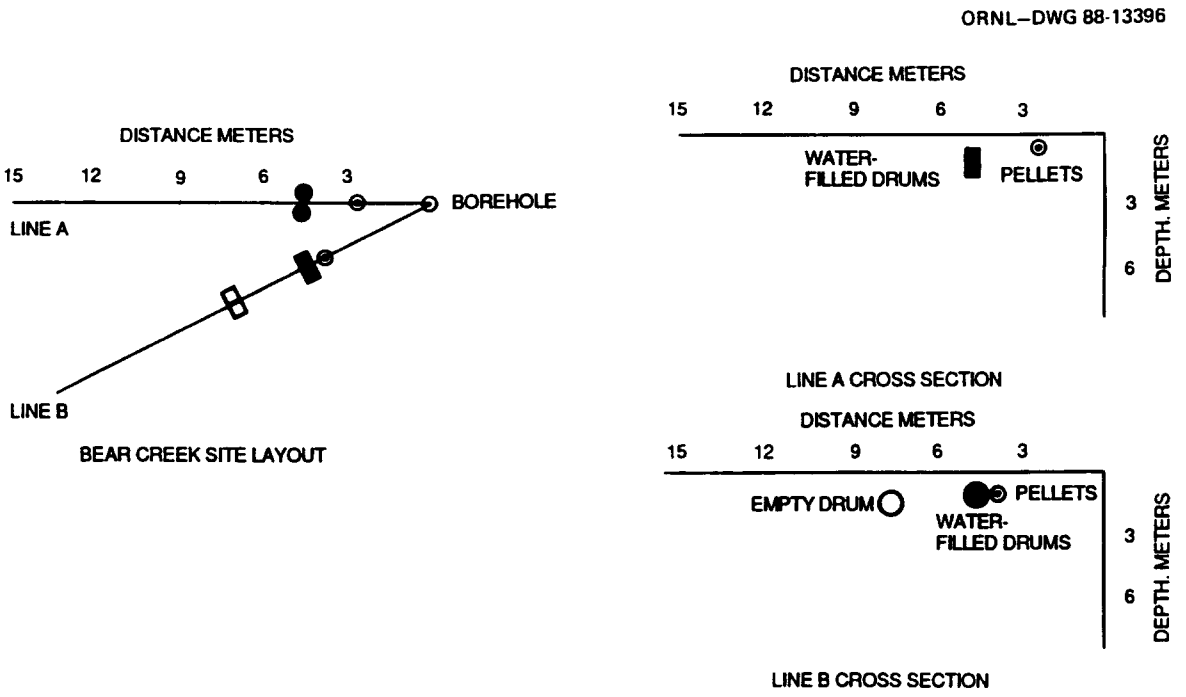

Figure 35: Buried target configuration at the two cross-sections developed at the Bear Creek site.

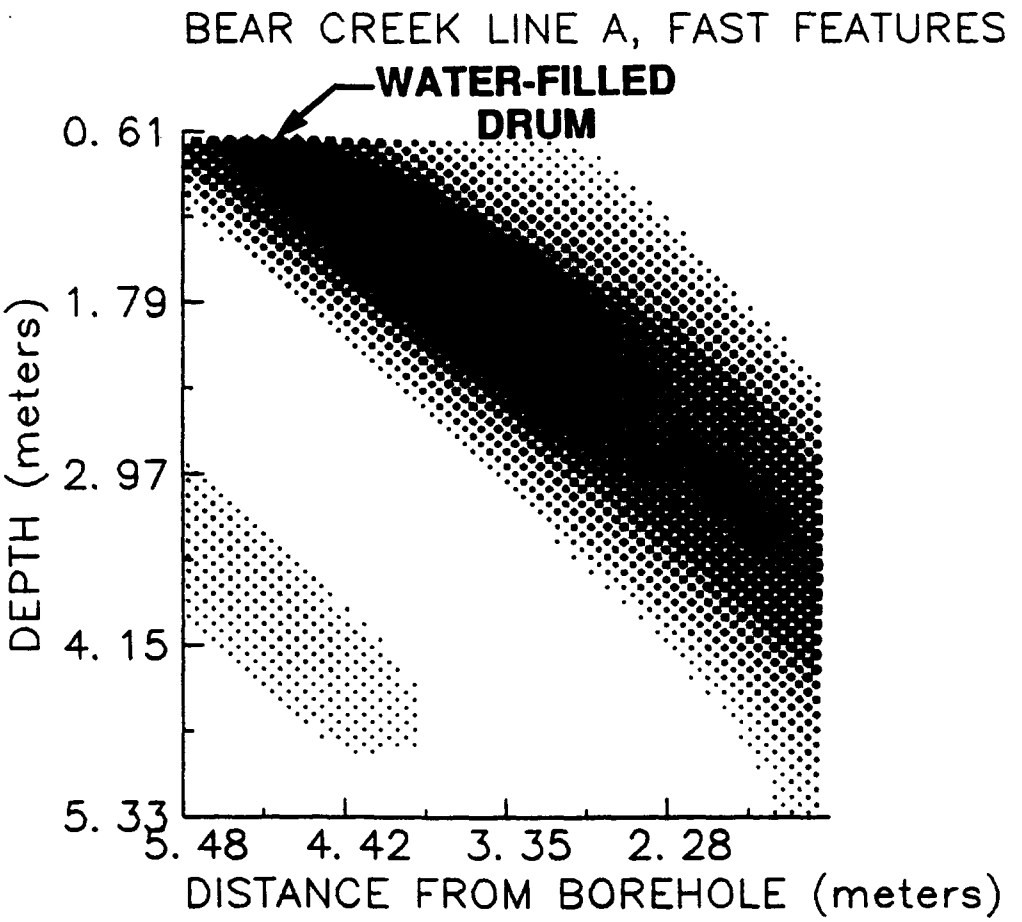

Figure 36: Gray-scale image of fast (high sound speeds) features below Line A at the Bear Creek site.

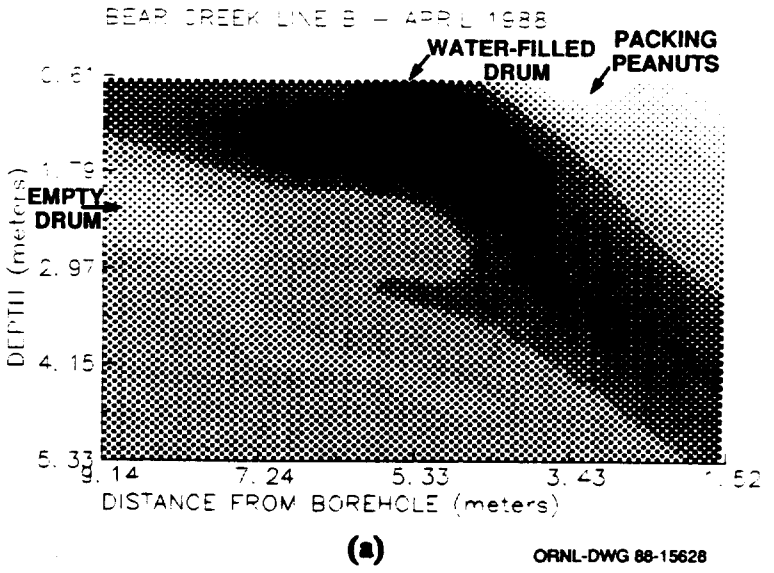

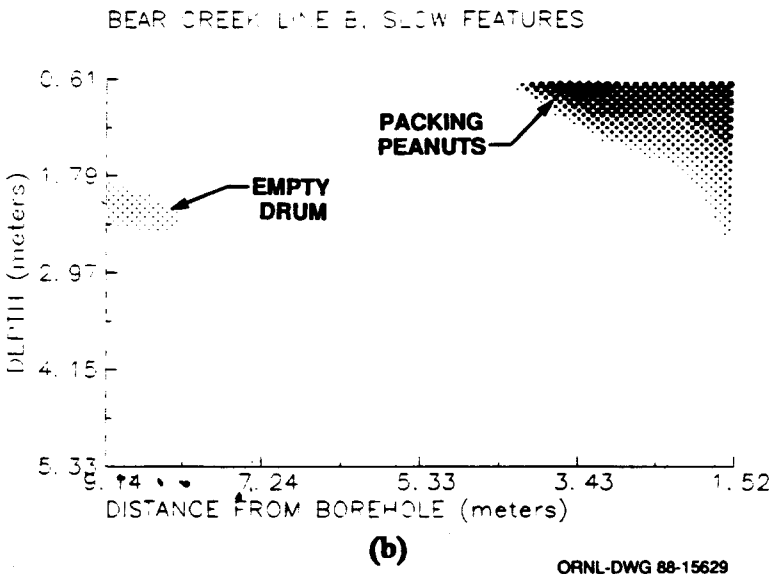

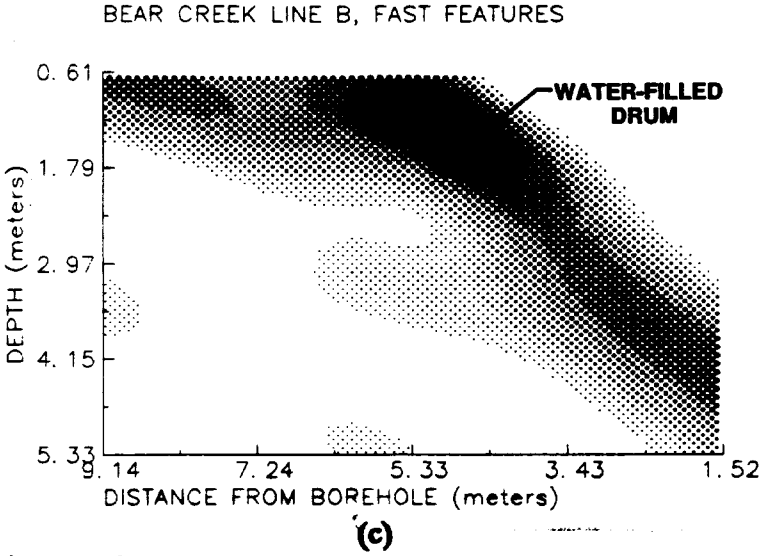

Figure 37: Gray-scale image of cross-section below Line B at the Bear Creek site for (a) full-range plotting contrast, (b) enhanced and inverted contrast to emphasize the slow (low sound speed) features, and (c) enhanced contrast to emphasize the fast (high sound speed) features.

displayed in this figure as black at about 1 m deep and 4.6 m from the well is the image of the two water-filled drums which exhibits a sound speed greater than both the surrounding soil and the wedge of weathered shale.

Images of cross-section B are given in Fig. 37. Because this image displays a number of features, all of which cannot be clearly shown using a single plotting contrast, results are presented for three plotting contrasts. The first [Fig. 37(a)] is a full range plotting contrast. All buried targets appear in this image at the proper location, but the empty drum, as expected, does not exhibit a strong contrast to the surrounding soil. The low sound speed features are displayed in Fig. 37(b). These are the empty drum appearing as the gray area 2 m deep and 9 m from the well and the bag of styrofoam packing peanuts appearing as the white area 1 m deep and 4 m from the well. The sound speed of the empty drum is slightly greater than that of the host soil while the sound speed of the styrofoam peanuts is slightly less than that of the soil. The image of the water-filled drum is less blurred when the plotting contrast is adjusted to highlight the high sound speed features [Fig. 37(c)].

5.4 Dinosaur Site Survey

A field study was performed in March 1988 at a remote site in the high desert of New Mexico. The objective of this study was to image the buried skeletal remains of a large sauropod dinosaur. The reasons that this particular project was undertaken were (1) to demonstrate that the system could operate under rugged field conditions and (2) to test the imaging method in a different geologic setting, sandstone rather than the clay and weathered shale typical of the ORNL reservation. While all other field tests described here were sponsored by USATHMA, this task was completed with ORNL discretionary funds.

No boreholes were developed at this site, instead existing coreholes were used. Capped PVC pipes were placed in these holes, filled with water, and annular regions between the hole walls and the casings were backfilled with sand from the site. The BETSY seismic gun was the primary energy source employed at the site, but a simple hammer and steel plate was also successfully tested here. Figure 38 is a photograph of this site.

The image shown in Fig. 39 is of a cross-section of the skeletal remains of the sauropod dinosaur buried in the host sandstone formation. The black area in this figure is a bone from the pelvic region of the dinosaur. This image, which was developed using the backpropagation algorithm in an offset VSP configuration, is included to demonstrate an important feature of remote sensing with this geometry. Here, the subsurface region containing the bone mass is buried beneath an area of numerous surface obstructions (vegetation, boulders, and irregular terrain). At this location it was not possible to deploy sources immediately above the desired study region. Consequently, source locations were established along a line radially outward from the borehole containing the receiver array beginning at a distance well beyond the bone location. The measurement geometry is illustrated in Fig. 40. The surface features at this site would make detection of the target of interest quite difficult with any remote sensing method based on a reflection measurement geometry; however, imaging was easily accomplished by the application of GDT. This result is significant in many

Figure 38: Photograph of an exposed and plastered bone mass at the dinosaur site.

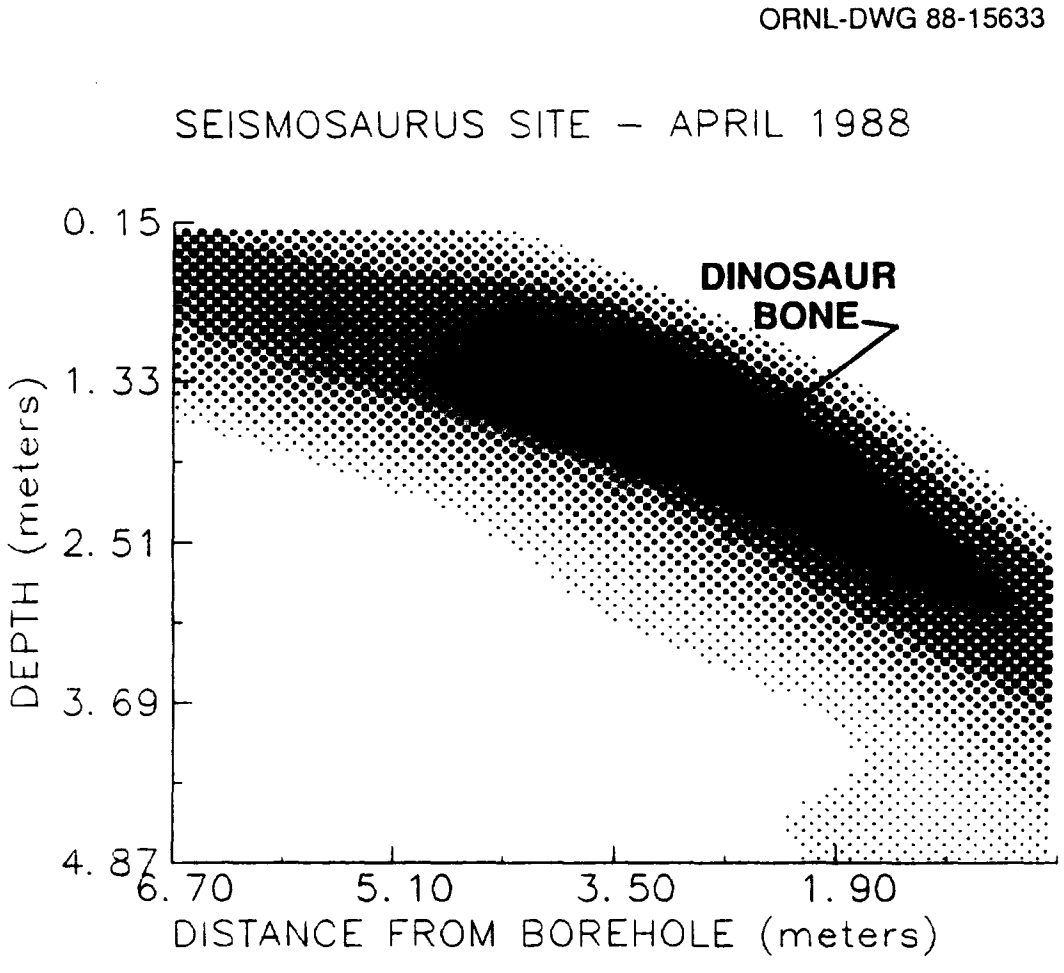

Figure 39: Gray-scale image of a vertical cross-section believed to contain buried dinosaur bone.

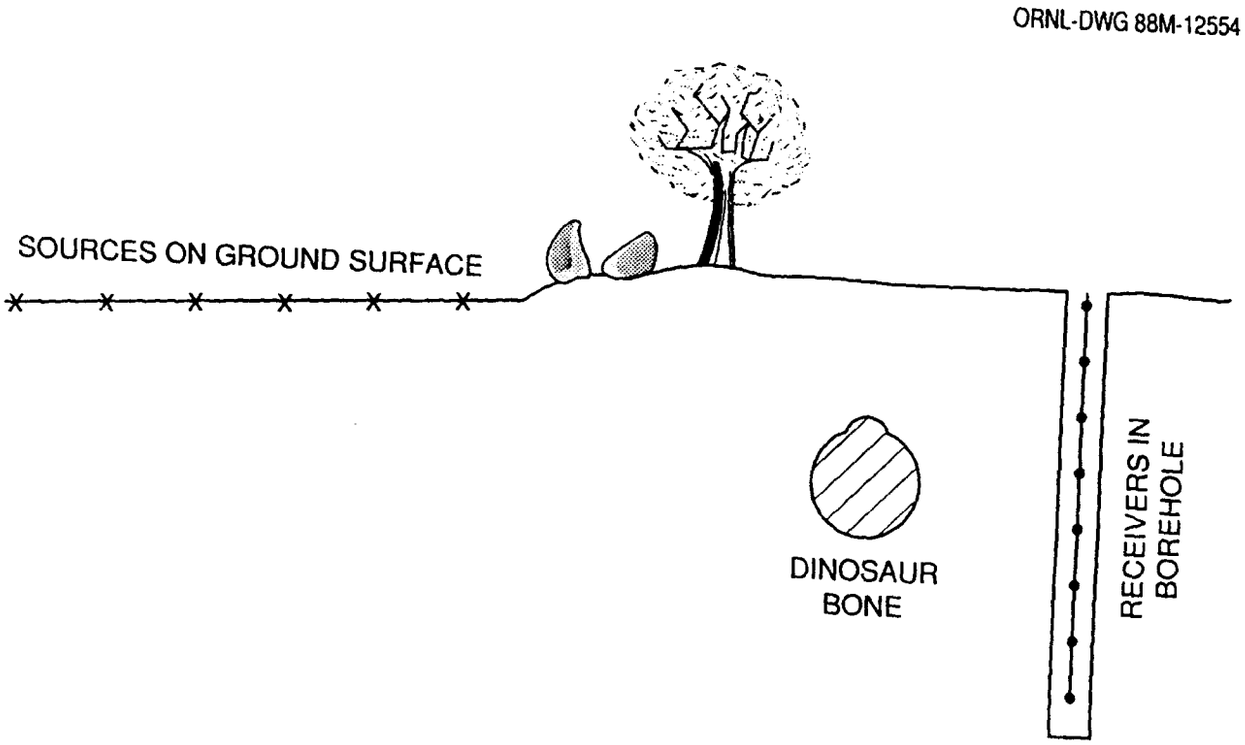

Figure 40: Illustration of measurement geometry required at the dinosaur site.

environmental applications in that it demonstrates the "look-under" capability available in tomography. This capability is important not only for naturally-occurring surface obstructions such as those encountered at the dinosaur site, but for man-made obstructions, such as buildings, above-ground storage tanks, areas of surface or shallow contamination, etc., as well.

5.5 Fort Rucker Survey

The most recent field test of GDT was performed at Ft. Rucker, Alabama during December 1988. The objective of the effort was to demonstrate the system in a "production" mode at a actual waste site. To achieve this goal a significant upgrade of the software was undertaken to produce the operating system described in Chapter 4. In its current form, the system operates in a mode comparable to the anticipated commercial technology.

The imaged region is a portion of a trench which itself is part of a series of trenches comprising a closed landfill at Ft. Rucker. No records exist of the contents and disposal practices employed during its operation, the landfill was closed in the early 1970's and is believed to predominantly contain wood and other construction debris. In order to identify areas containing isolated inclusions or other features of interest in a background setting of largely homogeneous decaying organic materials, a site screening exercise was conducted approximately one month prior to the December field test. At this time, a large portion of the site was surveyed using electromagnetic terrain conductivity mapping. This technique is implemented near the ground surface and detects subsurface regions of elevated electrical conductivity. All of the trench areas surveyed exhibited increased conductivity readings relative to background due to numerous small metallic objects distributed within each trench. One area in particular exhibited an anomolously high metallic content and this location was marked and the area surrounding this position was selected as the primary site for the GDT field test.

Immediately following the EM survey, the site was prepared for the application of GDT. This consisted of minor grading mainly to provide access for the drill rig followed by the drilling and development of cased boreholes. Figure 41 is a photograph of the site after site prep work was completed.

During the December field test at Ft. Rucker, data was collected and images reconstructed for five vertical cross-sections utilizing two boreholes. As shown in Fig. 42, three lines were surveyed along the axis of a trench (Lines 2, 3, and 4), one line was surveyed across the trench, and one survey line was established away from the trench area to image undisturbed background conditions. Pertinent data collection parameters for each of these cross-sections is summarized in Table 1. Figure 43 shows the horizontal and vertical extents of the three axial trench surveys. Images of these five cross-sections are shown in Figs. 44–48. It should be noted that in all these images a full range of view angles (transmission and backscatter) are used while in all previous results only transmission angles are considered.

Figure 44 is an image of Line 1 and displays the background conditions typical of undisturbed areas of the study site. Most evident in this image are numerous clay and sand soil

Figure 41: Photograph of the Ft. Rucker site.

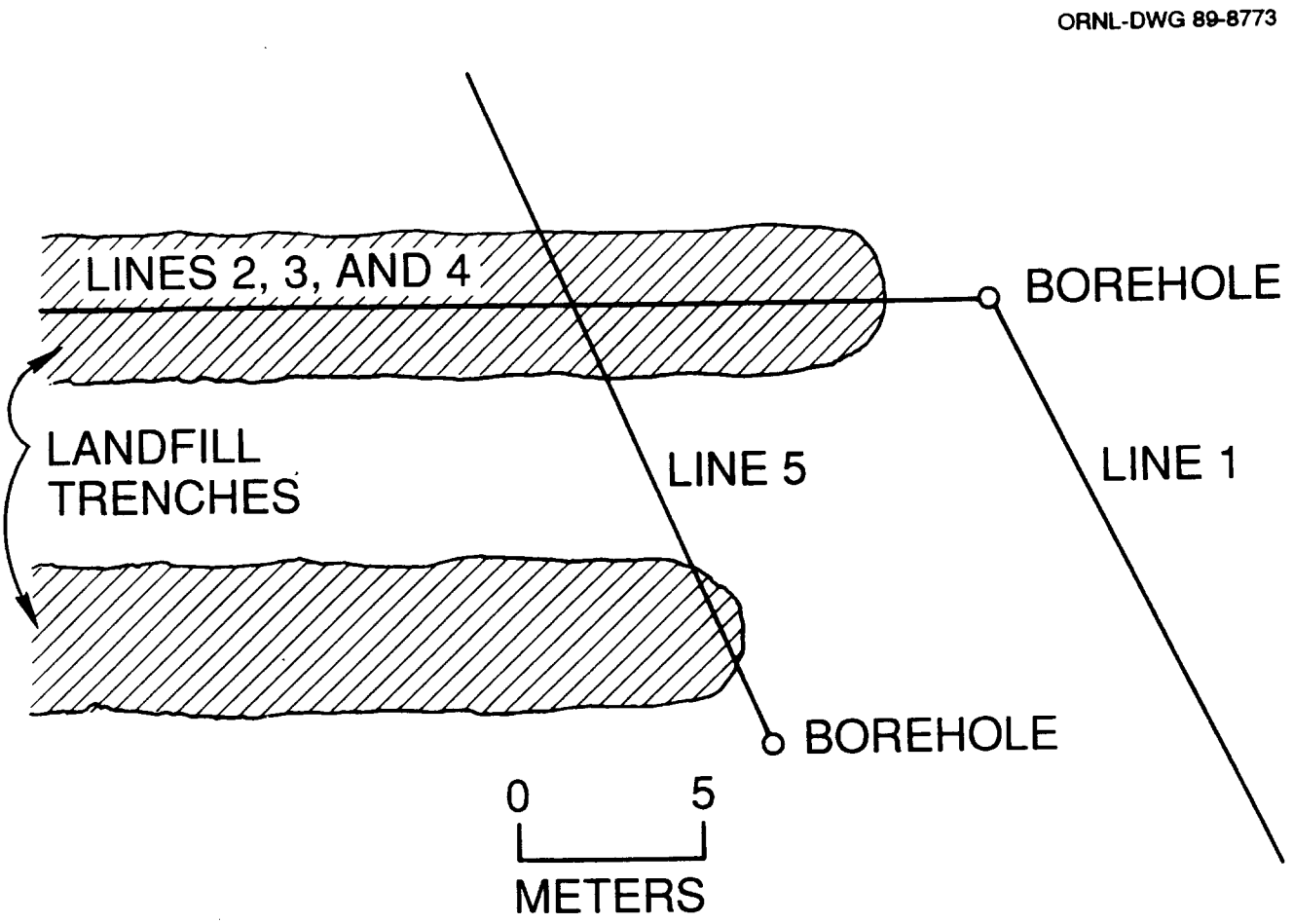

Figure 42: Site plan for the Ft. Rucker site.

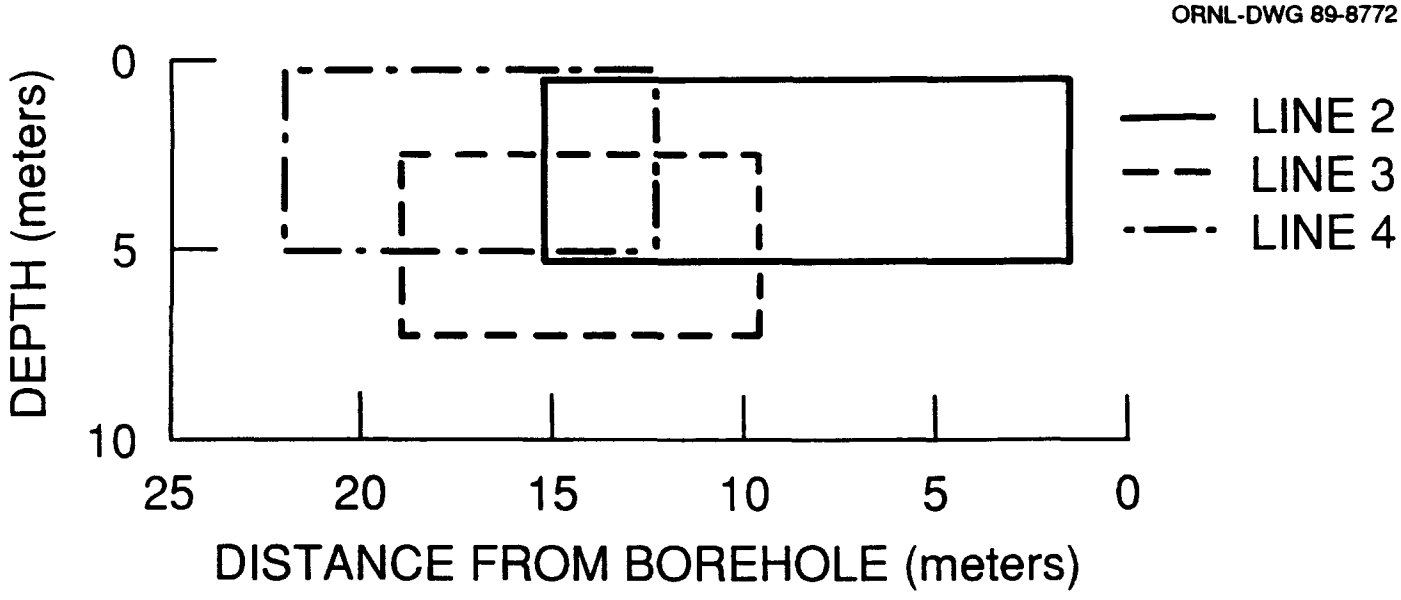

Figure 43: Illustration of the three imaged cross-sections along the axis of a Ft. Rucker landfill trench.

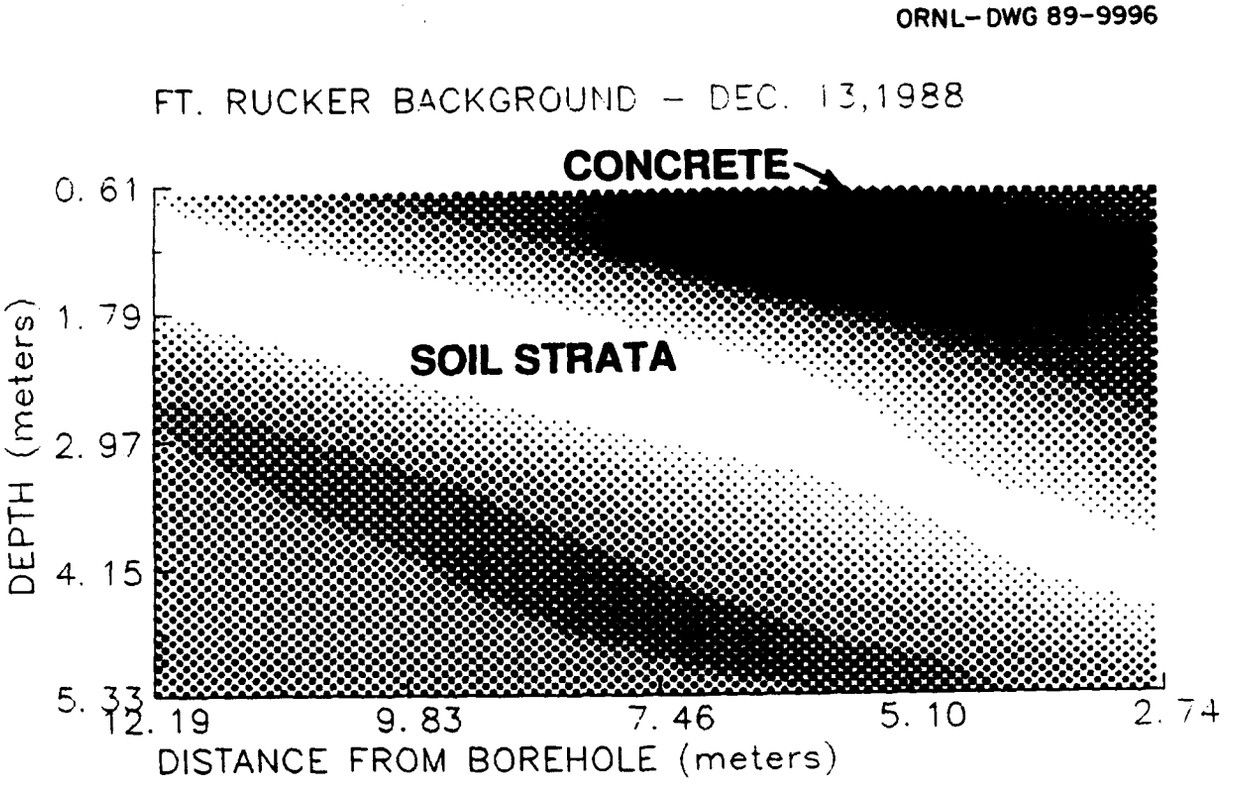

Figure 44: Gray-scale image of the cross-section below Line 1 (background conditions) at the Ft. Rucker site.

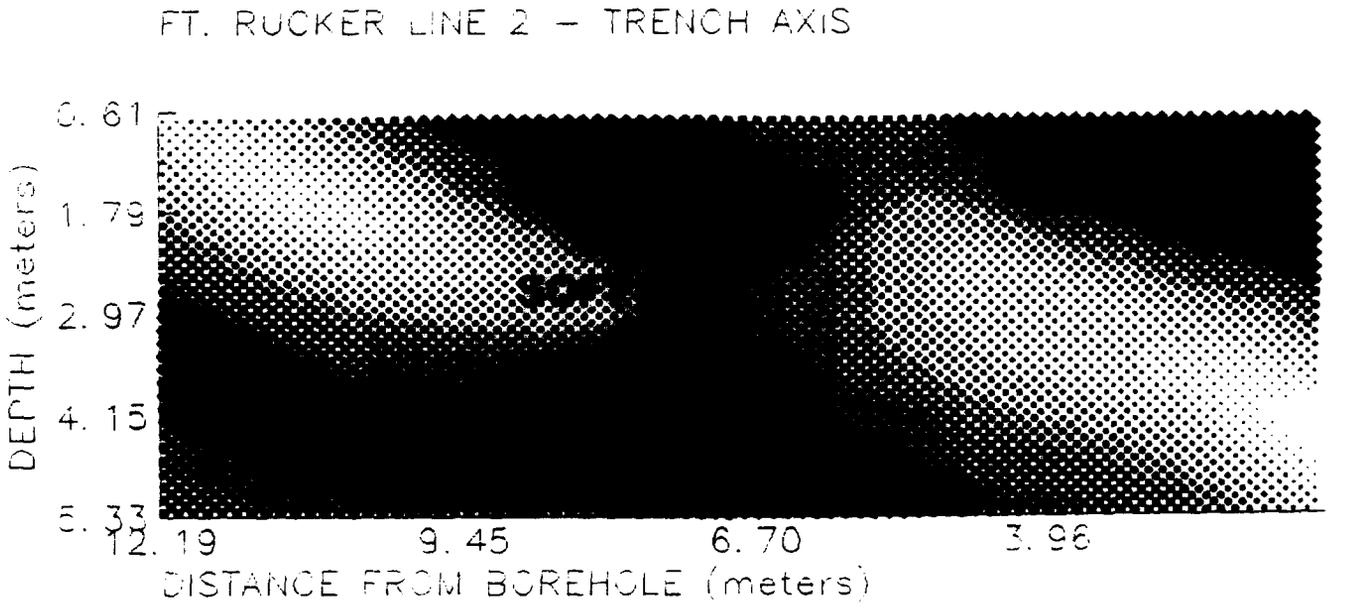

Figure 45: Gray-scale image of a cross-section along the trench axis below Line 2.

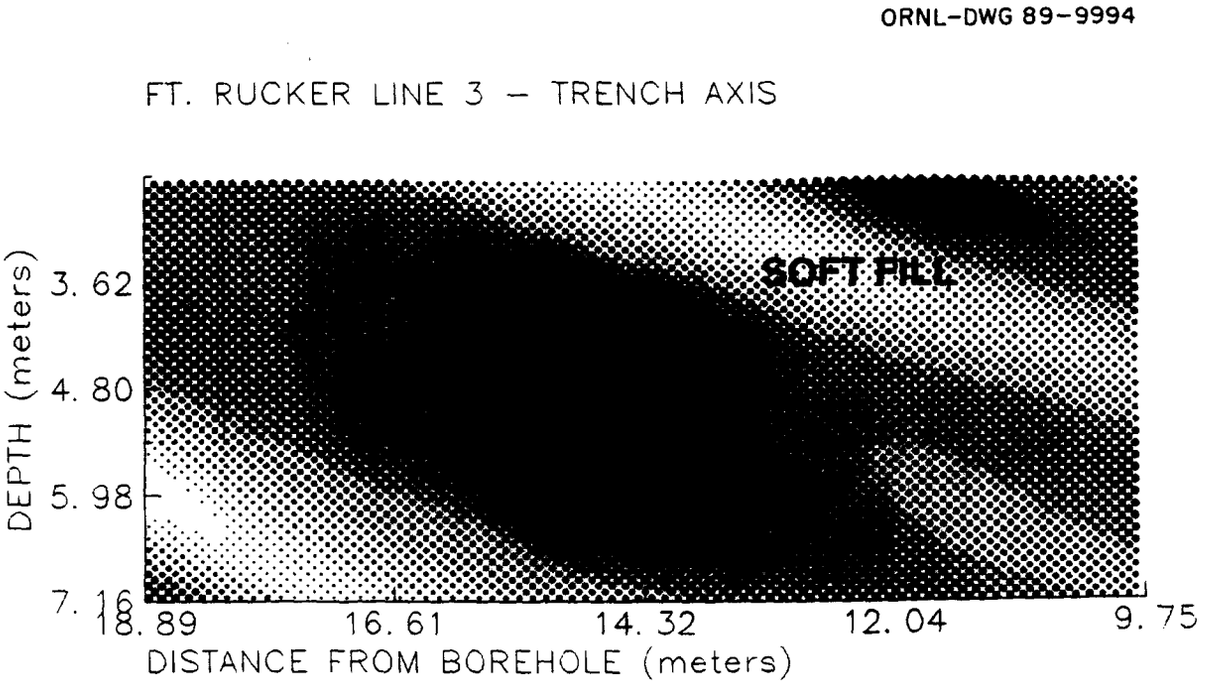

Figure 46: Gray-scale image of a cross-section along the trench axis below Line 3.

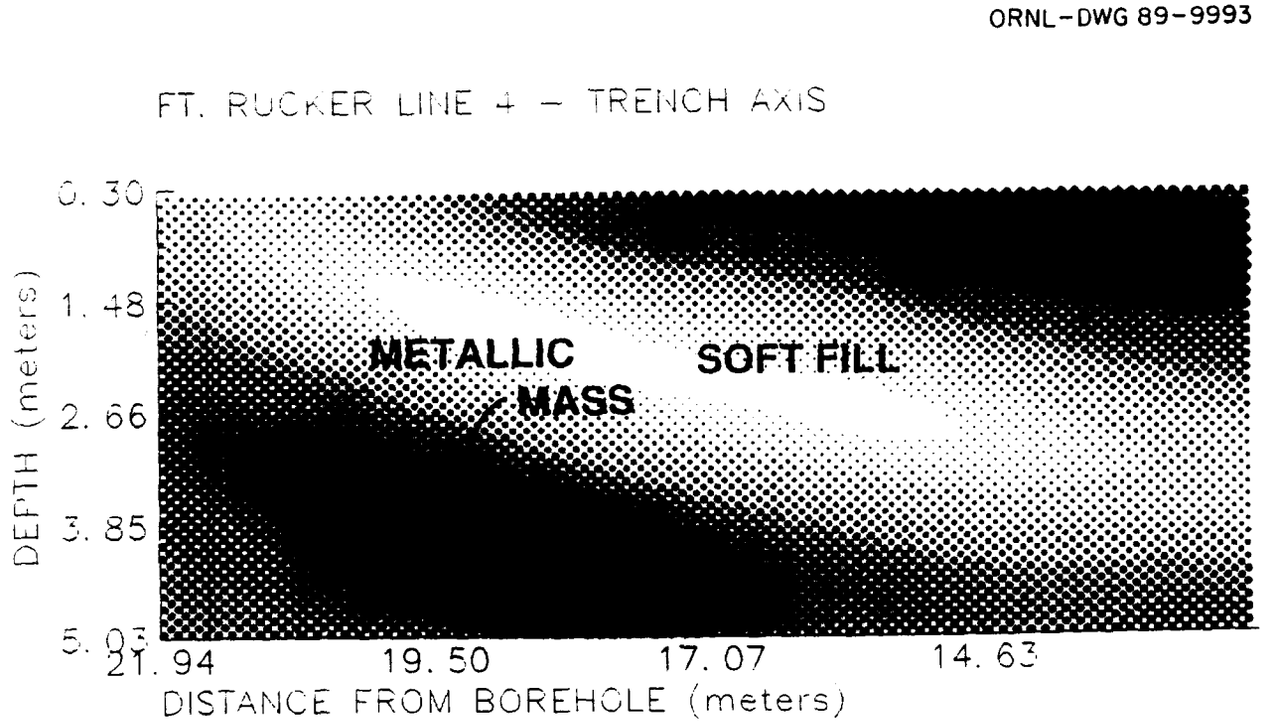

Figure 47: Gray-scale image of a cross-section along the trench axis below Line 4.

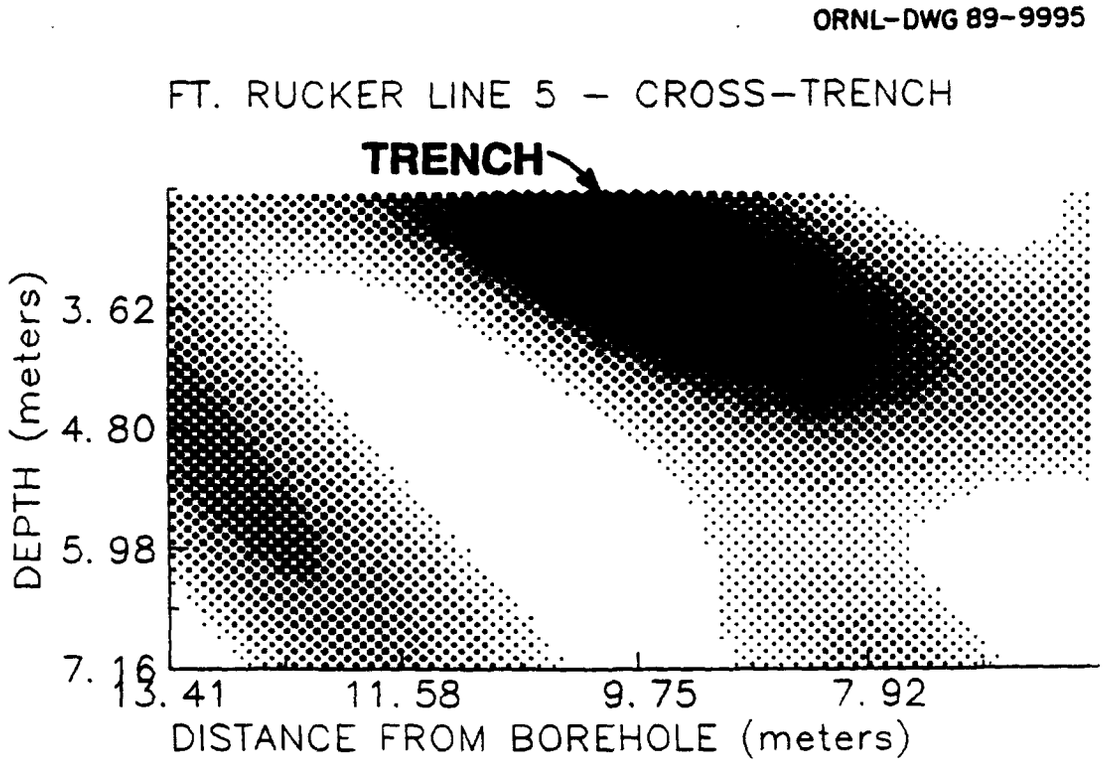

Figure 48: Gray-scale image of a cross-section below Line 5 which extends across the trench. The plotting contrast has been inverted to highlight the slow (low sound speed) features.

Table 1: Data acquisition parameters used in the Ft. Rucker field demonstration.

Line no.	Minimum receiver depth (m)	Minimum source offset (m)	Source spacing (m)	Sampling interval (μs)	Frequency (Hz)
1	0.61	1.21	0.61	100	176
2	0.61	1.21	1.21	100	98
3	2.44	9.75	0.61	200	176
4	0.30	12.19	1.21	300	98
5	2.44	1.21	1.21	100	98

strata found in southeastern Alabama. Note in this image that these layers exhibit a slight dip which, unlike the artifically tilted dry/moist soil contact shown in Fig. 31 resulting from geometric constraints, is believed to be real. The fastest layer occurs at the surface in this image. The presence of this layer, extremely dense hardpan soil, and its dip were confirmed by penetration studies. The only unexpected feature in this image is an isolated fast inclusion which appears as the black area in the upper right of Fig. 44. Excavation at this precise position revealed a small mass of buried concrete.

Images of the three surveyed cross-sections along the trench axis are provided in Figs. 45-47. Figure 43 should be used as a reference when comparing these results. It should be noted that overlap exists among these three cross-sections and that in these overlapping regions most features appear consistently within individual cross-sections. It is also important to realize that each plot displays a full range of gray scales determined by the minimum and maximum sound speed occuring within that particular cross-section. Therefore, gray levels are image-specific and not consistent from one image to the next. For this reason a feature common to more than one cross-section may appear as different gray scales.

Below Lines 2 and 4, Figs. 45 and 47; respectively, the mid-depths of the trench is characterized by very slow sound speeds displayed in these two images as white or light gray. This trench is believed to contain wooden construction debris. In the humid climate of Ft. Rucker, material of this type which has been in the ground for almost 20 years, has, no doubt, decayed to the point where it is quite compressible, having a consistency similar to peat moss. Thus, the very low sound speed is likely to be a result of the high compressibility of buried material in this area. In both of these figures, the highest sound speed areas occur near the top and bottom of the images. These regions represent the vertical boundaries of the trench. The feature appearing as black in the lower left portion of the Line 4 image (Fig. 47) exhibits the greatest sound speed of all the Ft. Rucker trench images. This feature is approximately 4 m long and its position corresponds exactly to the location of the anomolously high reading observed during the earlier EM survey. This would suggest that this object, or objects, is metallic; however, the reconstructed sound speed is not nearly great enough for this to be a solid metal mass. This again is consistent with the EM findings since this method responds to metallic surface area rather than metallic mass. This feature could be a large number of drums spaced so close together that they blur together in the image, one or several larger storage tanks, or other metallic objects with large surface areas

but low metallic mass.

The image below Line 3 (Fig. 46) is similar to the two other trench axis figures, but is too deep to display the upper boundary of the trench. The shallow region of this image displays the low speed typical of the bulk of trench contents along with an isolated fast inclusion in the upper right. Being a relatively deep cross-section, most of the area displayed in the image is below the lower boundary of the trench. The only feature difficult to interpret in the image is the slow area in the lower left corner of this figure. This is too deep to be associated with the landfill operations. It could be a naturally-occurring feature, but is too slow for this to be a reasonable interpretation. It is more likely that this is an image artifact associated with either edge effects of the slant stack or the fact that equipment failure required decommissioning of several of the deep receivers.

The final image from the Ft. Rucker field study is the survey line across the trench (Line 5). This cross-section is shown in Fig. 48. Here, the plotting contrast has been reversed so that fast areas appear as lighter gray levels and slower areas appear as darker gray levels. In this figure, the trench appears as the dark gray and black area in the upper central portion of the image. As in the trench axis figures (Figs. 45-47) the trench exhibits a low sound speed as a result of the highly compressible fill material. This image clearly shows the bottom and lateral trench boundaries; however, the imaged region spans a depth interval too deep for the upper trench boundary to appear in this figure.

6 CONCLUSIONS AND RECOMMENDATIONS

This report presents the mathematical basis for geophysical diffraction tomography (GDT), a description of the specialized field instrumentation and its implementation, as well as the results of all field studies thus far performed. These results suggests that GDT can fulfill its intended purpose, i.e. provide high-resolution, quantitative images of subsurface conditions at existing and potential hazardous waste storage or disposal sites. No special geologic criteria were specified in site selection to improve the results. A known waste configuration represents the only significant fixed variable for only one of these field tests, but is consistent with the overall development program being conducted. The field tests represent an iterative process in the development of the GDT system. In the first effort a single known isolated inclusion was imaged. Following this, experimental conditions have progressed to analyses of known multiple targets of both greater and less than background sound speed in the same imaging plane, and finally to sites with no a priori knowledge of subsurface conditions.

Recognizing the experimental controls applied, the results obtained provide for several very important conclusions for this level of development. Most importantly, all of the buried objects were successfully located and imaged. Reconstructions of cross-sections containing multiple targets characterized by both weak (sound speeds within 20% of background) and strong (sound speeds differing from background by an order of magnitude) inhomogeneities exhibited image quality comparable to that of simple cross-sections containing only a single target. In addition, images of targets having a sound speed less than background were of comparable quality to those having a sound speed greater than background. Geologic interfaces and soil moisture were not a problem in object detection and identification, but represented additional site characterization data obtained concurrently in the imaging process. Finally, field results have demonstrated the capability to detect and image buried objects without sampling needed directly over the target, a serious constraint with existing remote sensing technology.

In the most recent field test (Ft. Rucker, Alabama) it was demonstrated that the system could be operated efficiently in a "production" mode. In this test, operations were conducted in a manner similar to that for applications at actual waste sites. Using rapid data acquisition and the ability to immediately display results, it was possible to design the field program while the test was in progress. The results obtained for one cross-sectional survey were used in establishing subsequent cross-sections to be imaged. In this production mode, data could be acquired and preprocessed at a rate better than one source firing every minute. This is comparable to the time required to reposition the source. Because of the level of automation programmed into the system, this is considerably faster than conventional seismic methods. In addition, GDT offers much higher spatial resolution than such methods along with the capability to display final images in the field rather than well after the data collection has been performed.

Table 2 presents the time required to survey and image a 30 m cross-section as a function of the desired smallest resoluable features. This table was developed on the basis of the proven resolution of one-quarter of a wavelength, a required half wavelength source spacing,

and a demonstrated capability to collect data at a rate of one source firing per minute and to perform final data analysis within two minutes. It can be seen from this table that surveys can be performed very rapidly and that survey time decreases with decreasing resolution. Thus, one effective way to quantify areas of large extent is to first operate at low resolution to establish the locations of disturbed areas, such as trenches, or other features of interest. Then, based on these results, specific sites can be identified for higher resolution applications.

Table 2: Sampling requirement and implementation time as a function of resolution for 30 m survey line.

Resolution (m)	Source spacing (m)	No. of sources (minutes)	Survey time
0.3	0.6	50	52
0.6	1.2	25	27
1	2	15	17
1.5	3	10	12
3	6	5	7
5	10	3	5

While the existing data acquisition system has proven capable of efficient field operations, it is inadequate as a prototype for a commercially viable system. This is because it was designed for establishing the data acquisition parameters necessary for implementation of GDT. As such, it was designed for ease of modification using wire wraps rather than more rugged printed circuits. This, along with the limited computing power of personal computers and microprocessor chips available at the time the system was built, made it unnecessarily large and cumbersome. It is envisioned that the next generation of data acquisition system will serve as a prototype for a commercial product. By using state-of-the-art portable personal computers and microprocessors, the large data acquisition cabinet would be replaced by single data acquisition board installed in the portable supervisory PC. With it, the entire DAS supervisory computer system would be reduced in size to a small portable PC. In addition, the entire system would be battery-powered eliminating the need for local AC power or a portable generator. The awkward streamer containing the array of hydrophones and preamps, would be replaced by individual hydrophone/preamp pairs which could be transported to the field in a container the size of a large briefcase. The receiver array would be assembled in the field by connecting the components together with appropriate lengths of coaxial cable.

The final point to be made deals with demonstrated and anticipated applications of GDT. The method is capable of high resolution imaging not available from any existing remote sensing technology. Demonstrated abilities include:

1. detection of isolated inclusions

2. location of interface boundaries

3. detection of elevated moisture content

4. identification of homogeneous (clean) areas.

From these initial results numerous direct applications can be inferred. The benefits for buried object detection are obvious. Spatial delineation of waste burial areas is a simple extension of imaging isolated inclusions. Stratigraphy and identification of localized water tables are two uses applicable in site characterization studies. The ability to locate isolated soil moisture combined with the look under capability of the technique offers promise in identification of leaking ground-level or underground storage units. While all images presented in the previous section are for vertical cross-sections, Fig. 49 displays a sloping cross-section which represents a detection surface spanning the horizontal extent of the disposal unit. In this manner receivers are installed at a constant depth on one side of the storage tank and sources are fired on the opposite side either on the surface or downhole. The resultant image could detect any significant areas of isolated moist soils in the imaging plane which would infer leakage from the tanks or ponds. In a related example, an imaging plane could be constructed parallel to a subsurface grout curtain or other vertical barrier. This implementation would allow detection of all significant areas of soil moisture on the down gradient side of the barrier thus allowing for 100% evaluation of the barrier as compared to the less certain method of well sampling.

Through the results and potential applications presented here, it is seen that innovative implementation of the proven capabilities of geophysical tomography does suggest numerous opportunities for use in environmental engineering. Further development and applications will serve to further define and improve the capabilities of the technology; however, the system needed is ready for its primary use, characterization of hazardous waste burial sites.

ORNL-DWG 88M-12555

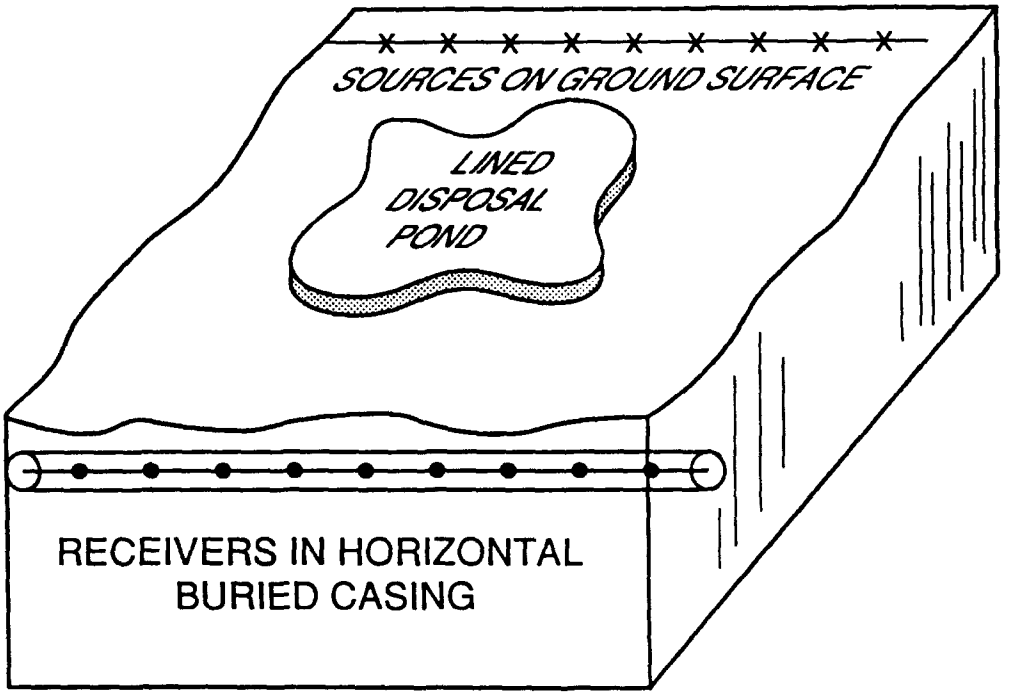

Figure 49: Illustration of a geophysical diffraction tomography measurement configuration which can be used to look under liquid waste storage or disposal units. Such a geometry could be used for the early identification of leakage.

7 REFERENCES

Anderson, D. L., and A. M. Dziewonski, "Seismic tomography," *Scientific American, 251*, 60–68, Oct. 1984.

Benson, R. C., R. A. Glaccum, and M. R. Noel, "Geophysical techniques for sensing buried wastes and waste migration," report prepared for Environmental Monitoring Systems Laboratory, Office of Research and Development, U. S. Environmental Protection Agency, Las Vegas, Nevada, 1982.

Devaney, A. J., "Inverse scattering theory within the Rytov approximation," *Optics Letters, 6*, 376–381, 1981.

Devaney, A. J., "A computer simulation study of diffraction tomography," *IEEE Trans. Biomed Eng. BME-30*, 377–386, 1983.

Devaney, A. J., "Geophysical diffraction tomography," *IEEE Trans Geosci. and Remote Sensing, GE-22*, 3–13, 1984.

Dines, K. A., and R. J. Lytle, "Computerized geophysical tomography," *Proc. IEEE, 67*, 1065–1073, 1979.

Fisk, P. et al., "Strength of materials in and around sinkholes by insitu geophysical testing," *Proc. 2nd Multidisciplinary Conf. on Sinkholes and Environmental Impacts of Karst*, 153–156, 1987.

Kak, A. C., "Computerized tomography with x-ray emissions and ultrasound sources," *Proc. IEEE, 67*, 1245–1272, 1979.

King, W. C. and A. J. Witten, "High resolution subsurface imaging with geophysical diffraction tomography," *Proc. 3rd National Outdoor Action Conference on Acquifer Restoration, Groundwater monitoring and Geophysical Methods*, 1989.

King, W. C., A. J. Witten, and G. D. Reed, "Detection and imaging of buried wastes using seismic wave propagation," *ASCE J. Env. Eng. Div., 115*, 527–540, 1989.

Morse, P. M. and H. Feshbach, *Methods of Theoretical Physics*, McGraw-Hill, New York, 1953.

Olehoeft, G. R., "Interpretation of hole-to-hole radar," *Proc. 3rd. Tech. Symp. on Tunnel Detection*, 616–629, 1989.

Schultz, P. S. and J. F. Clarebout, "Velocity estimation and downward continuation by wavefront synthesis," *Geophysics, 43*, 691–714, 1978.

Witten, A. J. and W. C. King, "A hardware/software system for implementing geophysical diffraction tomography," *SPIE Hybrid Image and Signal Processing, 939*, 64–70, 1988.

Witten, A. J. and W. C. King, "Acoustic imaging of subsurface features," *ASCE J. Env. Eng. Div., 116*, 166–181, 1989.

Witten, A. J. and E. C. Long Jr. "Shallow applications of geophysical diffraction tomography," *IEEE Trans. Geosci. and Remote Sensing, GE-24*, 654–662, 1986.

Witten, A. J. and J. E. Molyneux, "Geophysical imaging with arbitrary source illumination," *IEEE Trans. Geosci. and Remote Sensing, 26*, 409–419, 1988.

Witterholt, E. J., J. L. Kretzsehmar, and K. L. Jay, "The application of cross-hole electromagnetic wave measurements to mapping of a steam flood," *Proc. Petroleum Soc. CIM*, Paper 82-33-81, 1981.

Wolf, E., "Three-dimensional structure determination of semitransparent objects from holographic data," *Opt. Commun., 1*, 153–156, 1969.

A MATHEMATICAL CONSIDERATIONS

A.1 Inversion Procedure

The propagation of acoustic waves is governed by the scalar wave equation

$$\nabla^2 \overline{p} \; - \; \frac{1}{c^2(\underline{x})} \, \frac{\partial^2 \overline{p}}{\partial t^2} \; = \; - \, \overline{f}(\underline{x}, t) \tag{A.1}$$

where $\overline{p}(\underline{x}, t)$ is the pressure as a function of position $\underline{x}$ and time t, $c(\underline{x})$ is the spatially-variable wave speed, and $\overline{f}(\underline{x}, t)$ characterizes the spatial and temporal distribution of the energy source. It is more convenient to consider the frequency dependence than the time dependence, so that eq. (A.1) is Fourier transformed in time to yield

$$\nabla^2 p \; + \; k_0^2 n^2(\underline{x}) p \; = \; f(\underline{x}, \omega) \tag{A.2}$$

where

$$p(\underline{x}, \omega) \; = \; \int \overline{p}(\underline{x}, t) \; e^{i\omega t} dt, \tag{A.3a}$$

$$f(\underline{x}, \omega) \; = \; \int \overline{f}(\underline{x}, t) \; e^{i\omega t} dt, \tag{A.3b}$$

$n(\underline{x}) \; = \; c_0 / c(\underline{x})$ is the spatially-variable refractive index, c_0 is a reference sound speed, ω is the angular frequency (radians/sec), and $k_0 \; = \; \omega / c_0$ is the reference wavenumber at frequency ω.

The imaging problem is now one of extracting information about $n(\underline{x})$ from measured values of p. The most rigorous way to accomplish this is by direct inversion of eq. (A.2). This approach is not practical, so it becomes necessary to linearize this equation by invoking a weak scatter approximation. This is done by first expressing the refractive index as

$$n^2(\underline{x}) \; = \; 1 \; - \; \epsilon O(\underline{x}) \tag{A.4}$$

where $O(\underline{x})$ is referred to as the "object profile" and ϵ is the small parameter to explicitly represent a weak scatter approximation. For homogeneous conditions, $n(\underline{x}) \; = \; 1$ and $O(\underline{x}) \; = \; 0$. Thus, for weak scatter situations, the object profile is small.

The first type of weak scatter approximation to be discussed is the Born approximation. Within this approximation, it is assumed that the pressure p is composed of the sum of the pressure resulting from propagation in homogeneous conditions, this is referred to as the incident pressure p_i, and a perturbed pressure, p_s, associated with nonzero values of $O(\underline{x})$ (inhomogeneities). This is written as

$$p \; = \; p_i \; + \; \epsilon p_s \tag{A.5}$$

where the small parameter ϵ is explicitly included to reflect the fact that only a small perturbation in pressure will result from inhomogeneities of the order $\epsilon O(\underline{x})$. Substitution

of eqs. (A.4) and (A.5) into eq. (A.2), equating terms of equal powers of ϵ and neglecting terms of order ϵ^2, yields the set of linearized equations

$$\nabla^2 p_i + k_0^2 p_i = f \tag{A.6}$$

and

$$\nabla^2 p_s + k_0^2 p_s = k_0^2 O(\underline{x}) p_i, \tag{A.7}$$

where eq. (A.6) governs propagation in homogeneous conditions $[O(\underline{x}) = 0]$, while eq. (A.7) governs the corrective term for the pressure due to inhomogeneities.

Another weak scatter approximation is the Rytov approximation. Here, the total pressure p is represented by

$$p = e^{\psi} = p_i e^{\epsilon\psi'} = e^{\psi_0 + \epsilon\psi'}, \tag{A.8}$$

where ψ is referred to as the complex phase, ψ_0 is the incident or unperturbed phase ($p_i = e^{\psi_0}$) and ψ' is the perturbed phase associated with nonzero values of $O(\underline{x})$. The real part of ψ contains amplitude information while the imaginary part represents variations in wave phase. Substituting eq. (A.8) into eq. (A.2) and collecting terms of equal powers of ϵ yields

$$\begin{aligned}(\nabla^2 p_i) e^{\epsilon\psi'} + 2\epsilon(\nabla p_i) \cdot (\nabla\psi')\, e^{\epsilon\psi'} + \epsilon p_i\, (\nabla^2\psi')\, e^{\epsilon\psi'} \\ + k_0^2 [\, 1 - \epsilon O(\underline{x}) \,]\, p_i\, e^{\epsilon\psi'} = f(\underline{x}, \omega)\,.\end{aligned} \tag{A.9}$$

Utilizing the Rytov transform $D = p_i\psi'$, eq. (A.6) and the relationship $e^{-\epsilon\psi'} = 1 - \epsilon\psi'$ for $\epsilon\psi'$ small, eq. (A.9) simplifies to

$$\nabla^2 D + k_0^2 D = k_0^2 O(\underline{x}) p_i\,. \tag{A.10}$$

The two weak scatter approximations can be unified by defining D to be the reduced data, where

$$D(\underline{x}, \omega) = \begin{cases} p_i\psi'\,,\ p = p_i e^{\epsilon\psi'}\ ;\ \textit{Rytov approximation} \\ p_s\,,\ p = p_i + p_s\ ;\ \textit{Born approximation} \end{cases} \tag{A.11}$$

and both satisfy the linear equations

$$\nabla^2 D + k_0^2 D = k_0^2\, O(\underline{x}) p_i\,, \tag{A.12}$$

$$\nabla^2 p_i + k_0^2 p_i = f(\underline{x}, \omega)\,. \tag{A.13}$$

Following is the derivation of an analytic inversion procedure for the above system of equations. This is the mathematical basis for diffraction tomography. The measurement geometry considered here is the relatively general one shown in Fig. A-1. Both sources and receivers are deployed along lines having arbitrary orientation both to each other and the horizontal. The sources are located at positions ℓ_o on the line defined by unit vectors $\underline{n}$ and $\underline{n}_2$ while receivers are positioned at ℓ' along a line with unit vectors $\underline{m}$ and $\underline{m}_2$. The absolute position relative to the reference coordinates x, y of a source and receiver are

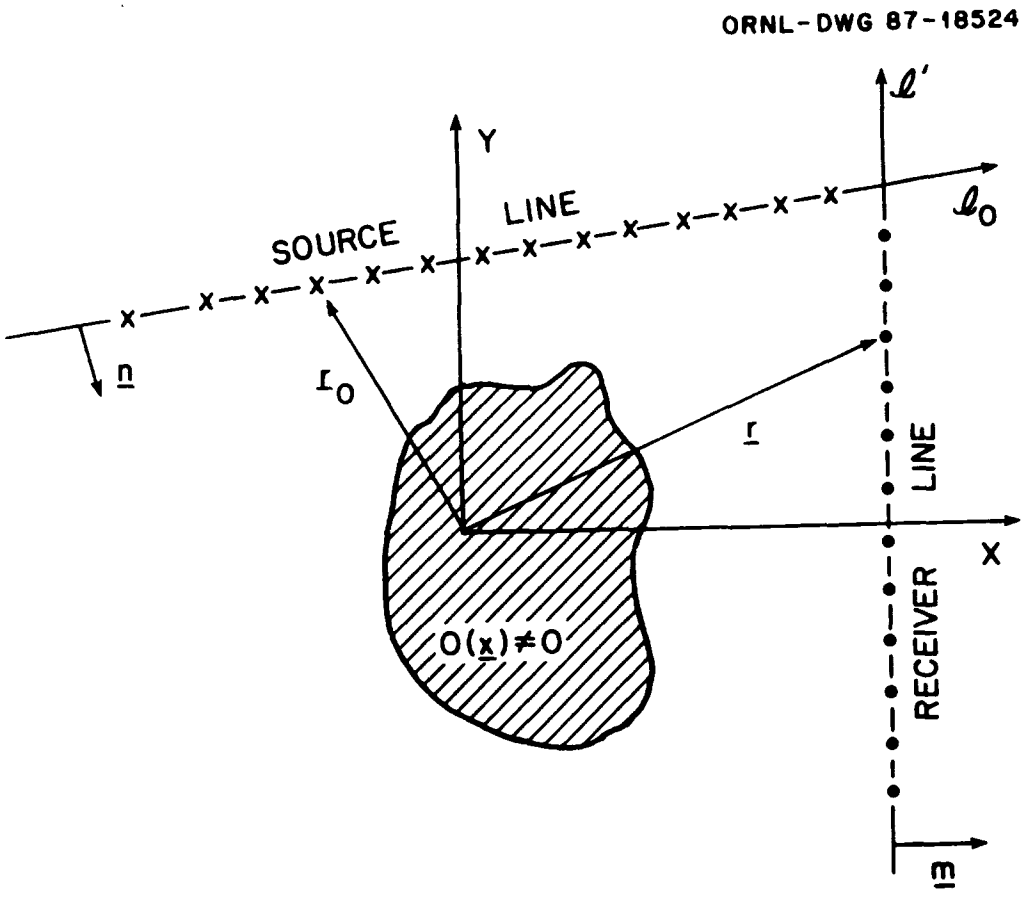

Figure A-1: Geometry and notation used in the derivation of the inversion algorithm.

defined by the vectors $\underline{r}_o$ and $\underline{r}'$, respectively. The solution to eq. (A.12) for measured values of reduced data D at position $\underline{r}'$ is given by (Morse and Feshbach 1953)

$$D(\underline{r}') \;=\; -\,\frac{ik_0^2}{4}\int d\underline{\xi}\; p(\underline{\xi})\; O(\underline{\xi})\; H_0\;(k|\underline{r}' \;-\; \underline{\xi}|) \tag{A.14}$$

where H_0 is the zeroth order Hankel function of the first kind. This function can be expressed in terms of its angular spectrum by

$$H_0(k_0\;|\underline{x}|) \;=\; \frac{1}{\pi}\int \frac{d\alpha}{\sqrt{k_0^2 \;-\; \alpha^2}}\; e^{i(\alpha m_2 \;+\; \sqrt{k_0^2 \;-\; \alpha^2}\;\underline{m})\;\cdot\;\underline{x}} \;. \tag{A.15}$$

Substituting eq. (A.15) into eq. (A.14) yields

$$\begin{aligned} D(\underline{r}') \;=\; -\,\frac{ik_0^2}{4\pi}\int \frac{d\alpha}{\sqrt{k_0^2 \;-\; \alpha^2}}\; & e^{i(\alpha m_2 \;+\; \sqrt{k_0^2 \;-\; \alpha^2}\;\underline{m})\;\cdot\;\underline{r}'} \\ \cdot \int d\underline{\xi}\; p(\underline{\xi})\; O(\underline{\xi}) & e^{-i(\alpha m_2 \;+\; \sqrt{k_0^2 \;-\; \alpha^2}\;\underline{m})\;\cdot\;\underline{\xi}} \;. \end{aligned} \tag{A.16}$$

The problem of imaging is now one of inverting eq. (A.16) to express the desired quantity, $O(\underline{x})$, in terms of the known values of D. This is most easily accomplished for plane wave illumination and, although plane waves cannot be generated in the field; for illustration purposes, this procedure is outlined below.

For a plane wave having a propagation direction defined by the unit vector $\underline{s}_0$, the incident field is simply

$$p_i(\underline{x}) \;=\; e^{ik_0\underline{s}_0\cdot\underline{x}} \;, \tag{A.17}$$

so that D for plane wave illumination, denoted as D_{pw}, can be written as

$$\begin{aligned} D_{pw}(\underline{r}') \;=\; -\,\frac{ik_0^2}{4\pi}\int \frac{d\alpha}{\sqrt{k_0^2 \;-\; \alpha^2}}\; & e^{i(\alpha m_2 \;+\; \sqrt{k_0^2 \;-\; \alpha^2}\;\underline{m})\;\cdot\;\underline{r}'} \\ \cdot \int d\underline{\xi}\; O(\underline{\xi}) & e^{-i(\alpha m_2 + \sqrt{k_0^2 \;-\; \alpha^2}\;\underline{m} \;-\; k_0\underline{s}_0)\;\cdot\;\underline{\xi}} \;. \end{aligned} \tag{A.18}$$

By defining the spatial Fourier transform operator

$$\hat{D}pw \;=\; \int d\ell'\; e^{-i\kappa\underline{m}_2\;\cdot\;\underline{r}'}\; D_{pw}(\underline{r}') \tag{A.19}$$

and applying this operator to both sides of eq. (A.19) yields

$$\hat{D}_p w\;(\underline{r}'\;\cdot\;\underline{m}, \kappa) \;=\; -\,\frac{ik^2}{2}\;\frac{e^{i\sqrt{k_0^2 \;-\; \kappa^2}\;\underline{m}\;\cdot\;\underline{r}'}}{\sqrt{k_0^2 \;-\; \kappa^2}}\hat{O}[\;k_0(\underline{s} \;-\; \underline{s}_0)\;] \;, \tag{A.20}$$

where $\underline{s} = \frac{1}{k_0}\left[\sqrt{k^2 - \kappa^2}\,\underline{m} + \kappa \underline{m}_2\right]$.

Equation (A.20) is the holographic lens equation and relates the one-dimensional spatial Fourier of the data along the receiver line to the two-dimensional spatial Fourier transform

$$\hat{O}\left[k_0(\underline{s} - \underline{s}_0)\right] = \int d\underline{\xi}\, O(\underline{\xi})\, e^{-ik_0(\underline{s} - \underline{s}_0)\cdot\underline{\xi}} \tag{A.21}$$

of the object profile.

In real applications, acoustic sources are typically impulsive point sources. The incident field, p_i, at a position $\underline{x}$ for a point source located at point $\underline{r}_o$ in two-dimensions is governed by

$$\nabla^2 p_i + k_0 p_i = -4\pi\,\delta(\underline{x} - \underline{r}_o) \tag{A.22}$$

and the solution to this equation is

$$p_i(\underline{x}) = i\pi\, H_0\left(k_0 \mid \underline{x} - \underline{r}_o \mid\right) = i\int \frac{dq}{\sqrt{k_0^2 - q^2}} e^{i(qn_2 + \sqrt{k_0^2 - q^2}\,\underline{n})\cdot(x - r_o)}. \tag{A.23}$$

Substituting this expression for the incident field into eq. (A.16) yields the expression for the measured data D for an impulsive point source

$$D(\underline{r}') = \frac{k_0^2}{4\pi}\int\int \frac{d\alpha dq}{\sqrt{k_0^2 - \alpha^2}\sqrt{k_0^2 - q^2}} \cdot e^{i(\alpha m_2 + \sqrt{k_0^2 - \alpha^2}\underline{m})\cdot r' - i(qn_2 + \sqrt{k_0^2 - q^2}\underline{n})\cdot\underline{r}_o} \cdot \int d\underline{\xi}\, O(\underline{\xi})\, e^{i(\alpha m_2 + \sqrt{k_0^2 - \alpha^2}\underline{m} - q\underline{n}_2 - \sqrt{k_0^2 - q^2}\,\underline{n})\cdot\underline{\xi}}. \tag{A.24}$$

This expression can be simplified by defining the operator

$$\hat{D}(\underline{r}', \nu) = \int d\ell_o\, e^{i\nu\underline{n}_2\cdot\underline{r}_o}\, D(\underline{r}'). \tag{A.25}$$

Applying this operator to both sides of eq. (A.25) and using the relationship

$$\int d\ell_o\, e^{i(\nu n_2 - qn_2 - \sqrt{k_0^2 - q^2}\,\underline{n})\cdot r_o} = 2\pi\,\delta(\nu - q) e^{-i\sqrt{k_0^2 - \nu^2}\,\underline{n}\cdot\underline{r}_o} \tag{A.26}$$

yields

$$\hat{D}(\underline{r}', \nu) = \frac{k_0^2}{2}\frac{e^{-i\sqrt{k_0^2 - \nu^2}\,\underline{n}\cdot\underline{r}_o}}{\sqrt{k_0^2 - \nu^2}} \cdot \int \frac{d\alpha}{\sqrt{k_0^2 - \alpha^2}} e^{i(\alpha m_2 + \sqrt{k_0^2 - \alpha^2}\,\underline{m})\cdot\underline{r}'} \cdot \int d\underline{\xi}\, O(\underline{\xi})\, e^{-i(\alpha m_2 + \sqrt{k_0^2 - \alpha^2}\,\underline{m} - \nu\underline{n}_2 - \sqrt{k_0^2 - \nu^2}\,\underline{n})\cdot\underline{\xi}}. \tag{A.27}$$

By defining $k_0 \cdot \underline{s}_0 = \nu \underline{n}_2 + \sqrt{k_0^2 - \nu^2}\, \underline{n}$,

$$D_{pw}(\underline{r}', \nu) = -\frac{i}{2\pi}\sqrt{k_0^2 - \nu^2}\, e^{-i\sqrt{k_0^2 - \nu^2}\, \underline{n} \cdot \underline{r}_o} \tag{A.28}$$

$$\cdot \int d\ell_o e^{i\nu \underline{n}_2 \cdot \underline{r}_o} D \ , \tag{A.29}$$

and applying the operator defined by eq. (A.19), eq. (A.27) becomes

$$\hat{D}_{pw}\ (\underline{r}' \cdot \underline{m}, \kappa) = -\frac{ik_0}{2} \frac{e^{-i\sqrt{k_0^2 - \kappa^2}\, \underline{m} \cdot \underline{r}'}}{\sqrt{k_0^2 - \kappa^2}} \cdot \hat{O}[\ k_0\ (\underline{s} - \underline{s}_0)\ ] \ . \tag{A.30}$$

This is the equation of a holographic lens identical to that for plane wave illumination [eq. (A.20)]. Thus, the operator defined by eq. (A.20) is a synthetic aperture lens which produces the response for plane wave illumination at an insonifying angle $\underline{s}_0$ given by eq. (A.28).

The final step of the inversion procedure is to recover $O(\underline{x})$ from eq. (A.30). This is

$$O(\underline{x}) = \frac{2i}{(2\pi)^2 k_0} \int d\underline{K} \sqrt{k_0^2 - \kappa^2}\, e^{-i\sqrt{k_0^2 - \kappa^2}\, \underline{m} \cdot \underline{r}'} \cdot \hat{D}_{pw}\, e^{i\underline{K} \cdot \underline{x}} \tag{A.31}$$

where

$$\underline{K} = k_0(\underline{s} - \underline{s}_0) \ . \tag{A.32}$$

For an offset VSP configuration, $\underline{n} = (0, -1)$, $\underline{n}_2 = (1, 0)$, $\underline{m} = (1, 0)$, $\underline{m}_2 = (0, 1)$ and by defining $\underline{s}_0 = (\cos\theta,\ \sin\theta)$, the wavevector $\underline{K}$ can be expressed in terms of κ and θ by

$$\underline{K} = (K_x,\ K_y) = \left[\sqrt{k_0^2 - \kappa^2} - k_0 \cos\theta,\ \kappa - k_0 \sin\theta\right] \ . \tag{A.33}$$

Computationally, it is more practical to integrate over θ and κ than over K_x and K_y. To accomplish this, the change of variables

$$dK_x dK_y = \begin{vmatrix} \frac{\partial K_x}{\partial \kappa} & \frac{\partial K_x}{\partial \theta} \\ \frac{\partial K_y}{\partial \kappa} & \frac{\partial K_y}{\partial \theta} \end{vmatrix} d\kappa d\theta = \begin{vmatrix} -\kappa/\sqrt{k_0^2 - \kappa^2} & -k_0 \sin\theta \\ 1 & k_0 \cos\theta \end{vmatrix} d\kappa d\theta$$

$$= \frac{k_0}{\sqrt{k_0^2 - \kappa^2}} \left|\sqrt{k_0^2 - \kappa^2}\, \sin\theta - \kappa \cos\theta\right| d\kappa d\theta \tag{A.34}$$

is introduced. For the offset VSP configuration, realizable viewing angles are $0 \le \theta \le -\pi$. For this range of viewing angles, the mapping defined by eq. (A.34) is not injective when (1) $-\pi/2 \le \theta \le 0$ and $\kappa = k_0 \sin\theta$, and (2) $-\pi \le \theta < -\pi/2$ and $\kappa = -k_0 \sin\theta$. In

addition, it is necessary to remove double coverage which occurs when K_x, $K_y < 0$ as well as evanescent modes $|\kappa| \geq k_0$. This is accomplished by defining the filter function

$$F(\kappa,\theta) = \begin{cases} 0, & for\ |\kappa| \geq k_0; \\ 0, & for\ -k_0 \leq \kappa \leq k_0 \sin\theta\ and\ -\frac{\pi}{2} \leq \theta \leq 0; \\ 0, & for\ -k \sin\theta \leq \kappa \leq k_0\ and\ -\pi \leq \theta < -\frac{\pi}{2}; \\ 2 & |\sqrt{k_0^2 - \kappa^2}\sin\theta - \kappa\cos\theta| \,/\sqrt{k_0^2 - \kappa^2}\ , \ otherwise. \end{cases} \tag{A.35}$$

with this the final form of the expression for $O(\underline{x})$ becomes

$$O(\underline{x}) = \frac{i}{2\pi^2 k_0}\int d\theta e^{-ik_0(x\cos\theta + y\sin\theta)}$$
$$\cdot \int d\kappa\ F\ \hat{D}_{pw}\sqrt{k_0^2 - \kappa^2}\ e^{i\sqrt{k_0^2 - \kappa^2}\ (x - \underline{m}\cdot\underline{r}') + i\kappa y}. \tag{A.36}$$

A.2 Phase Unwrapping

Implementation of geohysical diffraction tomography within the Rytov approximation requires a quantification of the perturbed phase, ψ' [eq. (A.11)], the imaginary part of which is essentially the difference in distance, measured in radians or wave cycles, between the full wave field and the wave field which would propagate in homogeneous conditions. For an impulsive source, the Fourier transformed pressure will be complex

$$p = P_R + iP_I \tag{A.37}$$

having real and imaginary parts P_R and P_I, respectively. Phase perturbations must be deduced from this relation and eq. (A.8) where

$$P_R + iP_I = e^{\psi} = e^{\psi_0 + \epsilon\psi'}. \tag{A.38}$$

The real part of ψ, ψ_R, where $\psi = \psi_R + i\psi_I$ is simply

$$\psi_R = \ell n\left(\sqrt{P_R^2 + P_I^2}\right), \tag{A.39}$$

while the principal value of the imaginary part of ψ, $\psi_I^{(p)}$, is given by

$$\psi_I^{(p)} = \arctan\left(P_I/P_R\right). \tag{A.40}$$

The arctan only returns values between $-\pi$ and π, the principal value, which represents only the fraction portion of the total number of wave cycles. Thus, ψ_I is related to $\psi_I^{(p)}$ by

$$\psi_I = \psi_I^{(p)} + 2\pi n \tag{A.41}$$

where $n = 0, \pm 1, \pm 2, ...$

The phase unwrapping procedure is a logical method for deducing n based on available information. To accomplish this, two assumptions are made. First, it is assumed that n

is known, based on field information for the shallowest receiver and second that changes in phase are smooth with receiver depth so that any large change in $\psi_I^{(p)}$ which occurs suggests a point of phase unwrap. By testing the difference between successive values in depth of $\psi_I^{(p)}$ points of large change in the difference, say $\pm \pi/2$, can be identified. At all such points a value of $\pm 2\pi$ is added to $\psi_I^{(p)}$ along with a value of $\pm 2\pi n$ associated with the ψ_I from the previous receiver position.

Having accomplished the phase unwrap by this procedure, the phase perturbation is easily computed by subtracting the complex quantity ψ_o, where

$$e^{\psi_0} = p_i = i\pi H_0 (k_0 R) , \tag{A.42}$$

from the full complex phase ψ.

A.3 Relationship of Sound Speed to Mechanical Properties

For an inviscid fluid, the equation governing the perturbed pressure D [eq. (A.11)] is

$$\nabla^2 D + k_0^2 D = - k_0^2 [\gamma_\beta(\underline{x}) + \gamma_\rho(\underline{x})] p_i - \frac{1}{2} \nabla^2 (\gamma_\rho) p_i , \tag{A.43}$$

where

$$\gamma_\beta(\underline{x}) = [\beta(\underline{x}) - \beta_0]/\beta_0 \tag{A.44}$$

is the normalized compressibility perturbations and

$$\gamma_\rho(\underline{x}) = [\rho(\underline{x}) - \rho_0]/\rho(\underline{x}) \tag{A.45}$$

is the normalized density perturbations. Comparing eq. (A.43) to eq. (A.10) it is easily seen that

$$O(\underline{x}) = 1 - c_0^2/c^2(\underline{x}) = - [\gamma_\beta(\underline{x}) + \gamma_\rho(\underline{x})] - \frac{1}{2k_0^2} \nabla^2 \gamma_\rho(\underline{x}) . \tag{A.46}$$

This clearly shows that wave speed variations are a result of perturbations in the more fundamental mechanical properties, density and compressibility. A similar relationship can be obtained from the acoustic approximation of the elastic wave equation. Here sound speed is a composite function of density and bulk modulus.